Influence of C_{60} fullerene on fretting wear of metals

B. M. Ginzburg, V. A. Krasnyĭ, Yu. P. Kozyrev, and V. P. Bulatov

Institute of Problems in Mechanical Engineering, Russian Academy of Sciences, St. Petersburg
(Submitted March 19, 1997)
Pis'ma Zh. Tekh. Fiz. **23**, 1–6 (August 12, 1997)

The potential usefulness of C_{60} as additives in lubricating oils and as coatings under fretting conditions is demonstrated by tribological techniques. © *1997 American Institute of Physics.* [S1063-7850(97)00108-0]

The discovery of fullerenes[1] has stimulated research into various aspects of these materials. However, information on the tribological properties is very scarce and applies mainly to the C_{60} fullerene. Several published studies have investigated C_{60} fullerene as a solid lubricant film[2,3] and also as additives to liquid lubricants.[4]

The use of various modified fullerenes as antifriction coatings, solid lubricants, and additives to lubricating oils has been reported in several patents.[5–11]

A particular form of damage to solids accompanying sliding friction is fretting wear.[12] Fretting is typically observed for nominally fixed structural members (for example, at points where components are attached), and generally occurs as a result of vibrations which lead to different vibrational relative displacements of the contacting bodies. Fretting is frequently accompanied by chemical processes at the friction surfaces (fretting corrosion).[13,14] A characteristic feature of fretting, unlike other forms of sliding friction, is the small amplitude of the relative displacements of the contacting bodies, comparable with the spacing between the tips of the microroughness points on the friction surface, which makes it difficult to remove the wear products from the contact zone. The wear products then begin to act as an abrasive, causing further wear. In many cases, the cyclic nature of the fretting reduces the fatigue strength of the contacting bodies, resulting in fatigue damage. Thus, the mechanisms responsible for fretting wear are very diverse and the various combinations of these under real conditions make it difficult to study and select ''antifretting'' protection measures.

Here we present the first results of phenomenological investigations of C_{60} fullerene as a material to prevent fretting wear under sliding friction.

The C_{60} fullerene (96–98% pure) was prepared in the laboratory of Professor V. P. Budtov (''Khromotron'' project of the Russian scientific-technical program ''Fullerenes and Atomic Clusters'').

The specimens were tested for fretting wear by the procedure laid down in GOST 23.211-80 (Ref. 14) using a special ''FK'' system attached to a standard SMTs-2 friction machine. The fixed surface — specimen — was a disk, 35 mm in diameter and 7.5 mm thick. The moving surface was a hollow cylinder with outer and inner diameters of 25 and 20 mm, respectively, whose end (annular) surface was in contact with the flat surface of the specimen. The cylinder undergoes cyclic rotational vibrations about its own axis. Different loads are applied to the cylinder along the axis to create a normal pressure at the contact. The test conditions were as follows: amplitude 150 μm, frequency 500 min^{-1}, normal pressure in tests with lubricants 4.2 MPa and without lubricants 3.2 MPa, and each specimen was tested over 250 000 cycles. At least three specimens of the same type were tested under the same conditions.

A series of tests were carried out on St20 steel and LaZh-60 brass specimens with St20 cylinders, using lubricating oil and grease with added fullerene C_{60} and preliminary tests on C_{60} coatings were also carried out.[1)] The wear of the specimens and cylinders was determined by weighing to within 0.1 mg before and after the tests.

The lubricants used were industrial I-40A oil and Litol-24 grease, to which C_{60} was added in powder form by mechanical mixing. The nonuniform distribution of the fullerene particles in the lubricant is clearly one reason for

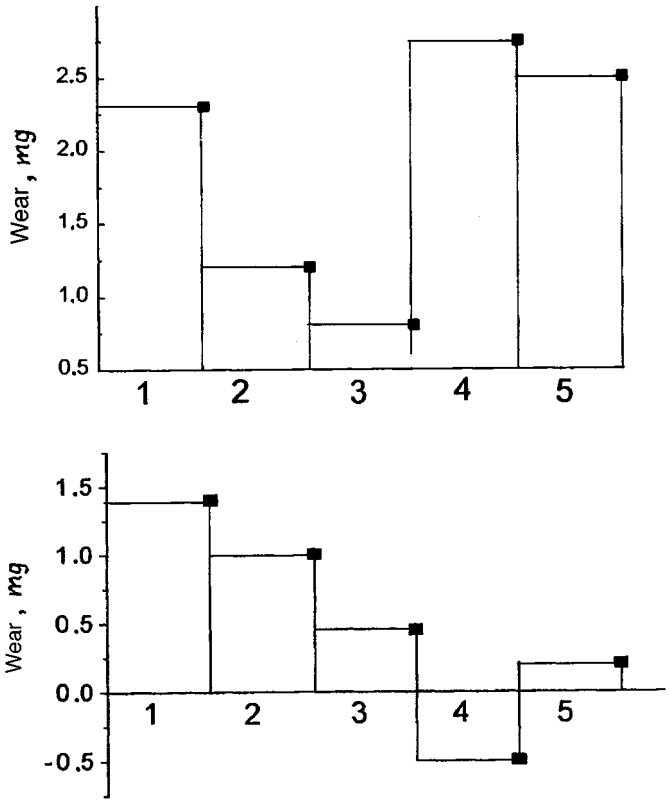

FIG. 1. Wear of steel specimens (upper diagram) and steel cylinders (lower diagram): *1* — without lubricant, *2* — I-40A lubricant, *3* — I-40A with 2.5% C_{60}, *4* — Litol-24, and *5* — Litol-24 with 2.5% C_{60}. A negative wear value indicates that some of the debris particles are transferred to the cylinder.

 1063-7850/97/080575-02$10.00

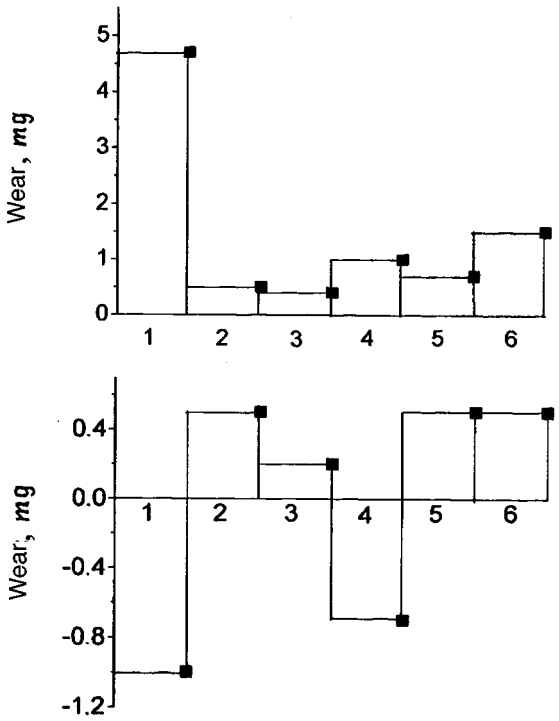

FIG. 2. Wear of brass specimens (upper diagram) and steel cylinders (lower diagram): *1* — without lubricant, *2* — I-40A lubricant, *3* — I-40A with 2.5% C_{60}, *4* — Litol-24, and *5* — Litol-24 with 2.5% C_{60}; *6* — C_{60} coating on brass specimen under dry friction.

the large spread of the experimental data (up to 20%).

The test results (as averages of the wear values for each series of specimens), plotted as histograms in Figs. 1 and 2, show that using I-40A lubricating oil appreciably reduced the fretting wear compared with unlubricated specimens, particularly for the brass specimens. When this lubricating oil was used on the friction track, there were no traces of binding and transfer of copper to the cylinder, which were observed for dry friction. By using this lubricating oil with added C_{60}, the wear of the specimens was reduced by a further 20–30% and that of the cylinders was reduced by 50% compared with the lubricating oil with no fullerenes added.

Unexpected results were obtained for the Litol-24 grease. For steel samples the wear with this lubricant was even higher than that under dry friction, and some of the wear debris was transferred to the cylinder. For brass specimens, Litol-24 was less effective than the lubricating oil, which may be attributed to its high viscosity and inadequate mechanical stability under shear deformation conditions. However, the addition of C_{60} to this lubricant reduced the wear compared with that with no additive.

Tests carried out on brass specimens with a C_{60} coating applied, showed that at a normal pressure of 4.2 MPa the specimens without any lubricant or coating exhibited binding and the rotation of the cylinder was visibly slowed. It was therefore necessary to reduce the normal pressure for the tests under dry friction conditions to 3.2 MPa. For a coated LAZh60 specimen, no slowing of the cylinder was observed, which indicated that no binding occurred in the initial period of fretting. The wear of the coated brass sample was approximately a third that of the uncoated sample under dry friction, no copper was transferred to the cylinder, and no traces of binding were observed on the friction track. This suggests that these coatings are effective as solid lubricants, particularly when it is structurally difficult to supply liquid lubricant to the friction site.

To conclude, these investigations have shown that it is effective to use C_{60} as additives to lubricating oils and also as coatings under fretting conditions.

This work was carried out as part of the Russian Scientific-Technical Program ''Fullerenes and Atomic Clusters'' (''Tribol'' project).

[1)]The coatings were applied in the laboratory of Professor A. Ya. Vul'.

[1] A. V. Eletskiĭ and B. M. Smirnov, Usp. Fiz. Nauk **163**(2), 33 (1993) [Phys. Usp. **36**, 202 (1993)].
[2] B. Bhushan, D. K. Gupta, G. W. Van Cleef *et al.*, Tribol Trans. **36**, 573 (1993).
[3] B. Bhushan, D. K. Gupta, G. W. Van Cleef *et al.*, Appl. Phys. Lett. **62**, 3253 (1993).
[4] B. K. Gupta and B. Bhushan, Lubr. Engin. **50**, 524 (1994).
[5] K. Shigematsu and K. Abe, *Preparation of Hydrogenated Fullerene*, Japanese Patent No. 05-229966, 02-25-92.
[6] H. Higashihara and K. Shigematsu, *Manufacture of Fluorinated Fullerenes*, Japanese Patent No. 06-24720, 07-06-92.
[7] K. Shigematsu and K. Abe, *Hydrogenated Closed-Structure Fullerene and its Preparation*, Japanese Patent No. 05-117174, 09-05-91.
[8] M. Taniguchi, Y. Tomioka, N. Kumegava, and M. Isibashi, *Lubricants*, Japanese Patent No. 05-179269, 12-27-91.
[9] A. O. Patil, G. W. Schriver, and R. D. Lundberg, *Lube Oil Compositions Containing Fullerene-Grafted Polymers*, US Patent No. 5,292,444, 10-02-92.
[10] A. O. Patil, G. W. Schriver, and R. D. Lundberg, *Fullerene-Grafted Polymers and Process for Their Preparation*, US Patent No. 5,292,813, 10-02-92.
[11] P. G. Bekiarian, P. J. Fagan, and P. J. Krusic, *Cyclofluoroalkylated Fullerene Compounds*, US Patent No. 5,382,718, 09-16-93.
[12] GOST 23.211-80, *Ensuring the Wear Resistance of Components. Method of Testing Materials for Fretting Wear and Fretting Corrosion*.
[13] N. L. Golego, A. Ya. Alyab'ev, and V. V. Shevelya, *Fretting Corrosion of Metals* [in Russian] (Tekhnika, Kiev, 1974).
[14] R. B. Waterhouse, *Fretting Corrosion* (Pergamon Press, Oxford, 1972; Mashinostroenie, Leningrad, 1976).

Translated by R. M. Durham

Thin-film electroluminescent emitters on rough substrates

N. T. Gurin, O. Yu. Sabitov, and I. Yu. Brigadnov

Moscow State University, Ul'yanovsk
(Submitted May 5, 1996; resubmitted March 3, 1997)
Pis'ma Zh. Tekh. Fiz. **23**, 7–12 (August 12, 1997)

For thin-film ac electroluminescent emitters prepared on rough glass substrates in combination with the use of a layer of liquid-crystal insulating composite, a twofold increase has been observed in the emission brightness as compared with the usual emitters prepared on smooth substrates. © *1997 American Institute of Physics.* [S1063-7850(97)00208-5]

A topical problem in the development of thin-film electroluminescent emitters and indicators based on them, utilizing the effect of prebreakdown luminescence, is to enhance the brightness, particularly of the blue and red luminescence.[1] Various designs of electroluminescent emitters have been proposed to enhance the luminescence brightness by increasing the radiation yield from the electroluminescent structure, including those with a rough substrate surface on which layers of electroluminescent emitter are deposited[2] and those with microroughness points on the surface of the transparent electrode.[3] In these structures the increase in the radiation yield may be influenced not only by purely optical effects but also by the nonuniform distribution of the electric field in the electroluminescent layer. Studies have shown that a nonuniform electric field distribution in the electroluminescent layer also exists in thin-film electroluminescent emitters with a composite liquid insulator, where this field is concentrated in local regions of contact between the filler grains of the composite liquid insulator and the electroluminescent layer.[4,5] This reduces the required average threshold strength of the electric field in the electroluminescent layer at which luminescence is initiated as compared with ordinary thin-film electroluminescent structures. If the structures of an electroluminescent emitter with a rough substrate and a layer of composite liquid insulator are matched, an increased degree of nonuniformity of the electric field in the electroluminescent layer should be expected, which may further enhance the radiation yield. In order

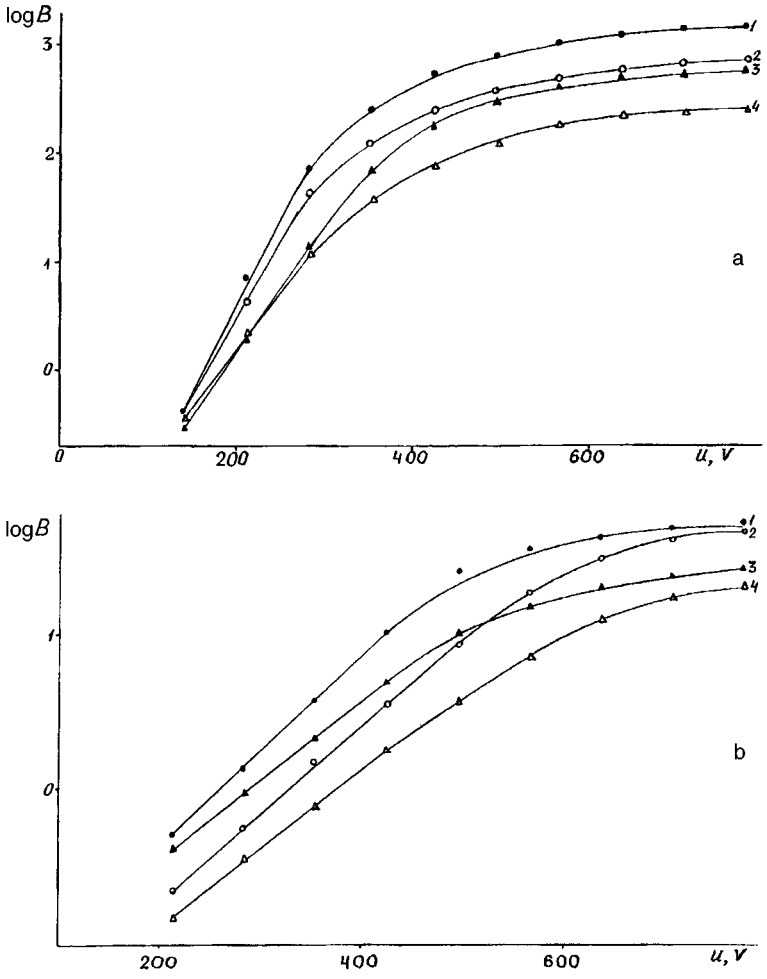

FIG. 1. Brightness–voltage characteristics of electroluminescent emitters: a — $d_c=40$ μm, b — $d_c=100$ μm, *1*, *3* — on rough substrate and *2*, *4* — on smooth substrate; *1*, *2* — $f=5$ kHz and *3*, *4* — $f=1$ kHz.

 1063-7850/97/080577-03$10.00

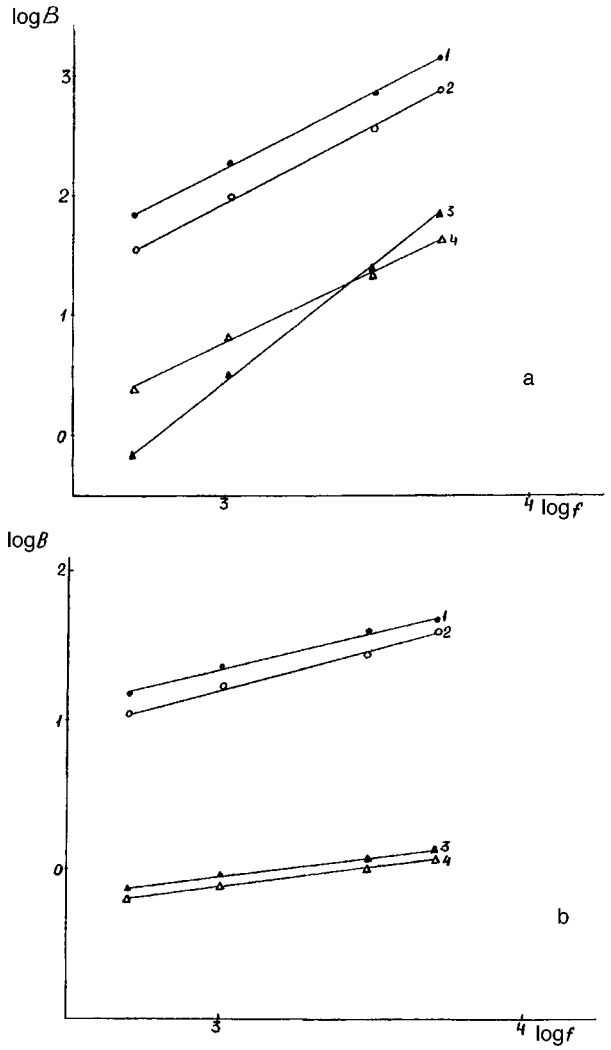

FIG. 2. Brightness of electroluminescent structures versus frequency: a — $d_c = 40$ μm, b — $d_c = 100$ μm, *1, 3* — on rough substrate, *2, 4* — on smooth substrate, *1, 2* — in saturation section of brightness–voltage characteristic, and *3, 4* — on increasing section of characteristic.

to check out this supposition, investigations were made of metal—semiconductor—composite-liquid-insulator—metal (MSCM) electroluminescent structures deposited on ordinary smooth and rough glass substrates. Here M is the first transparent SnO_2 electrode 0.2–0.3 μm thick and a second clamped metal electrode with micrometer-regulated movement accurate to within ± 5 μm, S is a ZnS:Mn (0.5% by weight) electroluminescent layer 1.2–1.5 μm thick, and C is a layer of composite liquid insulator consisting of a mixture of PFMS-4 silicon-organic liquid and a barium titanate $BaTiO_3$ powder filler with a grain size of 1.5–3.0 μm. The filler concentration in the composite liquid insulator is approximately 40% by volume. The SnO_2 transparent electrode was fabricated by the hydrolysis of stannic chloride. The phosphor layer was deposited by vacuum thermal evaporation in a quasiclosed volume and the composite liquid insulator was applied in paste form. Rough substrates were obtained by chemical etching of a smooth substrate in hydrofluoric acid. The results of measurements using an MII-4 microscope indicated that the rough substrates exhibited microroughness of height and linear dimensions of the order of 1 μm, uniformly distributed over the surface. The surface resistivity of the transmitting electrode on the smooth substrates was 100 $\Omega/\square$ and that on the rough substrates was 1000 $\Omega/\square$.

Brightness–voltage characteristics of the MSCM structure on rough and smooth substrates were obtained by exciting the structures with a sinusoidal voltage at frequencies of 1 kHz and 5 kHz. The sinusoidal voltage source was a G3-56/1 generator with a step-up transformer. The brightness of the electroluminescent structures was measured with a YaRM-3 light meter.

A comparison between the brightness–voltage characteristics of the electroluminescent structures (Fig. 1a) indicates that for similar threshold voltages (at brightness $B = 1$ cd/m^2) the maximum brightness of the luminescence in the saturation range of the brightness–voltage characteristic is twice as high for the electroluminescent structure on the rough substrate compared with the smooth at a frequency of 5 kHz, the respective maxima being 1445 cd/m^2 and 720 cd/m^2. At a frequency of 1 kHz, these maxima are more than twice as high, 560 cd/m^2 and 246 cd/m^2, respectively. The brightness-voltage characteristic of the electroluminescent structure on the rough substrate also exhibits a steeper slope compared with that for the smooth substrate. As the thickness of the composite liquid insulator layer is increased (Fig. 1b), the difference between the threshold voltages for the electroluminescent structures on the rough and smooth substrates becomes larger and is of the order of 60–70 V at 5 kHz and 90–100 V at 1 kHz. The brightness–voltage characteristics of the electroluminescent structure on both the smooth and the rough substrate do not have a clearly defined transition from abruptly increasing to saturation, which is typical of thin-film MISIM electroluminescent structures.

Curves of the brightness B as a function of the frequency f (Figs. 2a and 2b) for electroluminescent structures with an insulator thickness $d_c = 40$ μm indicate that the section of abruptly increasing characteristic for the electroluminescent structure on a rough substrate typically shows linear behavior of $B(f)$ (exponent $\alpha_f = 1$) whereas for the structure on the smooth substrate, this curve is sublinear with $\alpha_f \approx 0.6$. In the saturation section of the characteristic the slope of the curves plotted in logarithmic coordinates, log B versus log f, is almost the same for both electroluminescent structures and corresponds to an exponent $\alpha_f \approx 2/3$, which agrees with the results of studies of electroluminescent structures with a composite liquid insulator reported in Ref. 5. It can be seen from Fig. 2b that as the thickness of the insulator layer is increased to $d_c = 100$ μm, the exponent α_f for the electroluminescent structures on rough and smooth substrates becomes almost the same and is ~ 0.25 for the section of abruptly increasing characteristic and ~ 0.55 for the saturation section, respectively.

The increase in the maximum brightness of the electroluminescent structure on the rough substrate compared with the smooth may be attributed to a local rise in the electric field strength in the electroluminescent layer. Other factors may be a microlens pattern formed on the substrate and a microrelief which reduces the waveguiding effect, so that the

radiation yield from the electroluminescent structure is increased.

It should be noted that the luminescence of the electroluminescent structure on the rough substrate has a clearly defined granular property compared with the smooth substrate,[5] and this may be attributed to the microlens effect.

It has thus been demonstrated that by using rough substrates combined with a layer of composite liquid insulator in an electroluminescent emitter, the radiation yield from the structure and the brightness of the luminescence can be enhanced substantially. This may be utilized to develop electroluminescent emitters based on phosphors whose brightness is inadequate in ordinary MISIM structures.

[1] N. A. Vlasenko, *Electroluminescent Display Devices* [in Russian] (Znanie, Kiev, 1991)
[2] U. S. Patent No. 4,474,435 (1988).
[3] U. S. Patent No. 4,728,581 (1988).
[4] I. Yu. Brigadnov and N. T. Gurin, Pis'ma Zh. Tekh. Fiz. **16**(23), 71 (1990) [Sov. Tech. Phys. Lett. **16**, 914 (1990)].
[5] I. Yu. Brigadnov and N. T. Gurin, Zh. Prikl. Spektrosk. **59**, 175 (1993).

Translated by R. M. Durham

Electronic and adsorption properties of the real surface of cadmium selenide films containing indium whiskers

Yu. A. Vashpanov

I. I. Mechnikov State University, Odessa
(Submitted March 12, 1997)
Pis'ma Zh. Tekh. Fiz. **23**, 13–17 (August 12, 1997)

An investigation is made to determine how surface doping of thin semiconducting cadmium selenide films with heavy metal atoms influences their binding energy and their absorption sensitivity to oxygen. Under certain doping conditions, indium atom whiskers are formed on the surface of the films. These samples show an appreciable reduction in the oxygen binding energy with the surface and a reversible response in the interaction with oxygen at 353 K.
 [S1063-7850(97)00308-X]

It is known that surface doping with metal atoms is an effective method of controlling the surface parameters of semiconductor materials.[1] In particular, changes in the oxygen binding energy have been observed by surface doping of cadmium selenide films with indium and selenium atoms.[2] Fundamental changes in the electronic properties of the semiconductor are mainly observed up to thicknesses of a monolayer, so that investigations are limited to this region of doping levels. The physical nature of the changes in the binding energy between oxygen and the surface of the material has been attributed to dipole interaction of donor impurity—adsorbed oxygen molecule complexes, whose surface concentration increased with increasing ligand concentration. The formation of clusters on the surface of the material strongly influences the electronic and adsorption properties of the solid. However, the adsorption properties of semiconductor materials containing various metal cluster structures at their surfaces have not been studied in sufficient detail. Information on the mechanism of interaction between gas particles and these surfaces is required from the theoretical and practical points of view.

Samples of semiconducting cadmium selenide films were prepared by thermal deposition of powder onto cold substrates in a high vacuum of 10^{-7} Torr. Deposition of the cadmium selenide layer at room temperature was immediately followed by the deposition of vapor-phase metallic indium atoms on the semiconductor surface

Studies of the electronic properties of these samples revealed that many samples whose surfaces were doped with indium atom concentrations of more than one monolayer retained their semiconducting properties, whereas other samples had a temperature coefficient of resistance typical of metallic conductivity. A study of the adsorption of oxygen on the surface of these structures showed that at 353 K the conductivity of the film exhibits reversible changes whereas at these temperatures all known semiconductor materials are known to exhibit irreversible changes in conductivity.

Curve *1* in Fig. 1 gives results of studying the binding energy of adsorbed oxygen particles by a method described in Ref. 3 as a function of the degree of doping of the surface with indium atoms. It can be seen that the binding of oxygen with the semiconductor surface decreases substantially to 0.4 eV. The electron mobility in the samples in vacuum is activated after the desorption of oxygen, with an activation energy of 0.3 eV. As the oxygen concentration was increased to 45 Vol.% in a mixture with high-purity nitrogen, this activation energy was observed to decrease to 0.15 eV. Above one monolayer the effective electron concentration was almost independent of the degree of doping.

It is known that surface doping is accompanied by the formation of cluster structures whose size increases with increasing surface concentration.[4] At specific concentrations, a continuous metal film forms on the surface[5] as a result of the coagulation of clusters, and its thickness increases with further condensation of the metal. The physical properties of the material are then determined by the metal film.

In our case, no continuous film is formed for indium atom concentrations much greater than one monolayer (10^{17}–10^{19} cm^{-2}). It is known that under certain conditions of condensation from the vapor phase, some metal atoms form cluster filaments perpendicular to the surface, known as whiskers.[6] In this case, no continuous metal film forms and the metal clusters grow perpendicular to the surface. The formation of whiskers of various atoms, including indium atoms, has now been observed.[7] The physical factors responsible for the formation of whiskers are associated with screw dislocations at the surface of a solid with an extremely stressed surface state. These dislocations lead to the growth of a metal cluster (whisker) perpendicular to the surface. The electronic and adsorption properties of the material contained in these clusters has been little studied. The fact that the effective electron concentration and mobility do not depend on the concentration N_s for values greater than a monolayer indicates that indium whiskers are formed on the surface of the semiconducting cadmium selenide film.

The experimentally observed decrease in the oxygen binding energy is caused by these cluster structures on the surface of the semiconductor. It is known that in metal filaments free electrons are distributed over the surface as a result of the skin effect.[8] From electrostatics, the maximum concentration of free charge should be concentrated at the tip of the whisker. Thus, strong electrostatic fields reaching 10^7 V/cm may be created near the tip.[9] In particular, metal tips are used in electron and ion field emission. The tip of the whisker containing the largest number of free electrons acts as a site for the effective adsorption of oxygen particles since

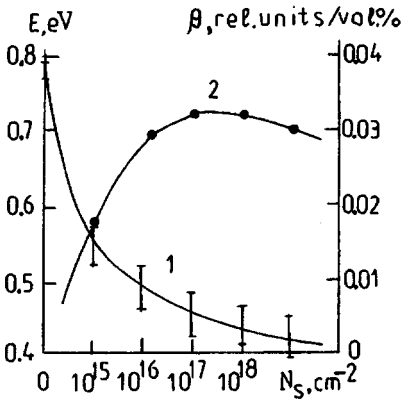

FIG. 1. Binding energy of oxygen on the sample surfaces (curve *1*) and adsorption sensitivity at 353 K (curve *3*) as functions of the degree of doping of the surface of cadmium selenide films with indium atoms.

free electrons serve as oxygen adsorption centers.[10]

The changes in the binding energy observed in the experiments cannot be attributed merely to dipole repulsion of complexes since, according to Ref. 11, the energy of this interaction does not exceed 0.2 eV. The dipole–dipole interaction is observed at distances greater than the lattice constant. At distances of the order of the lattice constant, as is found at the whisker tip, the adsorbed atoms may undergo Coulomb repulsion: $E_{\text{el.stat}}(R)=2q^2/R(\varepsilon_0+1)$ (Ref. 11). Only the electrostatic interaction in the adsorbed complex may lead to the observed decrease in the binding energy between the oxygen and the surface as a result of strong electrostatic fields at the tip of the metal whisker.

The highest rate of exchange between the solid and the gas phase should then be observed at the whisker tips, since this is where the binding energy is lowest and the electron (adsorption center) concentration is the highest. As a result of their concentration gradient, the adsorbed particles diffuse along the surface of the whisker toward the base, where the oxygen ions directly influence the electron parameters of the semiconductor film.

The formation of finely dispersed clusters on the surface gives rise to a nonuniform electronic structure in the semiconductor film, which causes strong fluctuation of the band potential along the surface. The experimentally observed mobility activation energy is directly related to the formation of a current-transport barrier structure. A region enriched in n-type electrons is formed at the base of the whiskers, and a barrier 0.3 eV high is formed between them. Adsorption of oxygen changes the value of this barrier. A change in the transparency of the barrier as a result of adsorption was observed in Ref. 12.

It is interesting to note that these structures possess long-term stability in contact with oxygen at concentrations between 0 and 45 vol.%. At measurement temperatures of around 343 K, the adsorption and desorption times are no greater than 2–3 min. In this temperature range, films of almost all known semiconductor materials showed an irreversible change in conductivity caused by the adsorption of oxygen. One of the surprising properties of filamentary crystals metal (whiskers) is their high chemical stability to oxidation. For instance, an iron whisker oxidizes 50 times more slowly at 773 K compared with polycrystalline iron.[13] Quantum filaments of silicon in porous silicon exhibit similar chemical stability.[14] Thus the long-term stability of these samples to the adsorption and desorption of oxygen may be explained by the chemical stability of the metallic indium whiskers at temperatures of 353 K.

Measurements were made of the adsorption-desorption sensitivity β using a procedure described in Ref. 15. The results of the measurements are given by curve *2* in Fig. 1. For these samples the change in conductivity was mainly caused by the change in the effective electron mobility. Thus the physical mechanism responsible for the adsorption sensitivity is mainly attributable to the change in the transparency of the barrier between the cluster structures on the semiconductor surface caused by the adsorption of oxygen.

[1] V. E. Primachenko and O. V. Snitko, *Physics of a Metal-Doped Semiconductor Surface* [in Russian] (Naukova Dumka, Kiev, 1996).
[2] Yu. A. Vashpanov, V. A. Smyntyna, and V. V. Serdyuk, Poverkhnost' Fiz. Khim. Mekh. No. 1, 93 (1984).
[3] Yu. A. Waschpanow, Phys. Halbleit. (Berlin) **20**, 69 (1989).
[4] Yu. I. Petrov, *Clusters and Small Particles* [in Russian] Nauka, Moscow, 1988).
[5] Yu. F. Komnik, *Physics of Metal Films: Size and Structural Effects* [in Russian] (Atomizdat, Moscow, 1979).
[6] V. G. Syrkin, *Future Materials. Metal Fiber Crystals* [in Russian] (Nauka, Moscow, 1990).
[7] P. V. Zevy and O. F. Kammerer, J. Appl. Phys. **26**, 1182 (1955).
[8] V. S. Ivanova, *Synergetics and Fractals in Materials Science* [in Russian] (Nauka, Moscow, 1994).
[9] *Physics Encyclopedia*, edited by A. M. Prokhorov [in Russian] (Sovetskaya Entsiklopedia, Moscow, 1988), p. 585.
[10] V. F. Kiselev and O. V. Krylov, *Electronic Effects in Adsorption and Catalysis on Semiconductors and Insulators* [in Russian] (Nauka, Moscow, 1979).
[11] O. M. Braun and V. K. Medvedev, Usp. Fiz. Nauk **157**, 631 (1989) [Sov. Phys. Usp. **32**, 358 (1989)].
[12] P. G. Borzyak and Yu. A. Kulyupin, *Electronic Processes in Island-like Metal Films* [in Russian] (Naukova Dumka, Kiev, 1980).
[13] G. V. Berezhkova, *Filamentary Crystals* [in Russian], Nauka, Moscow (1969), p. 106.
[14] M. E. Kompan and I. Yu. Shabanov, Fiz. Tekh. Poluprovodn. **29**, 1859 (1995) [Semiconductors **29**, 971 (1995)].
[15] Yu. A. Waschpanow, *Festkörperchemie Komplexer Oxidischer Systeme* (BRD, Greifswald, 1990), pp. 170–180.

Translated by R. M. Durham

Three-dimensional lattice of parallel-oriented tellurium nanoclusters in an opal matrix

V. N. Bogomolov and L. M. Sorokin

A. F. Ioffe Physicotechnical Institute, Russian Academy of Sciences, St. Petersburg
(Submitted March 18, 1997)
Pis'ma Zh. Tekh. Fiz. **23**, 19–24 (August 12, 1997)

Transmission electron microscopy has been used to study the structural state of tellurium introduced into the voids of an opal matrix from a melt under pressure. It is shown that when the opal is a single crystal (the SiO_2 spheres form a close-packed cubic structure), tellurium filling the voids produces an ordered cluster lattice. The tellurium in the clusters has a single-crystal structure whose orientation is conserved in neighboring clusters within an appreciable area. It is thus shown that a lattice of parallel-oriented nanoclusters can be obtained in principle. © *1997 American Institute of Physics.* [S1063-7850(97)00408-4]

With the advances in technology developed in Refs. 1–3, it has now become possible to produce three-dimensional superlattices formed by submicron clusters in synthetic opal. These superlattices have been studied intensively as materials for the next generation of electronics. Synthetic opals, like natural ones, consist of amorphous SiO_2 spheres of fairly uniform size, 200–250 nm in diameter. In order to obtain a three-dimensional lattice of clusters, i.e., a periodic structure in which a unit cell with a ''quasiatom'' can be isolated as a cluster, the SiO_2 spheres in the opal must have an ordered cubic or hexagonal close-packed structure. Then the voids between the spheres will have a regular periodic distribution; i.e., a three-dimensional sublattice of voids is found in the opal ''crystal.'' Since the size of the SiO_2 spheres is a fraction of a micron, geometric analyses[2] indicate that the octahedral and tetrahedral voids will have dimensions of 45–55 and ~85–105 nm, respectively, for the sphere sizes indicated above. These dimensions will also determine the maximum size of a quasiatom in the cluster lattice when various materials are introduced into the opal matrix by various methods. For ideal SiO_2 spheres, the voids in the opal are connected by channels having a triangular cross section with concave sides. The diameter of the inscribed cylinder is ~30–40 nm. These capillaries ensure that all the pores are filled with the material when the initial opal is placed in a suitable medium. The matrix must be an ideal single crystal to achieve 100% filling of all pores, which account for up to 22–26% of the total volume of the matrix, since the presence of blocks, small- and large-angled boundaries, and other defects will block some of the voids.

It is therefore of interest to use transmission electron microscopy to study the structural state of the material in the cluster, the possibility of crystallization of the material in the microvolume, and the influence of the channels (microcapillaries) between the voids on the crystallographic orientation of a particular cluster relative to its neighbors during its crystallization process.

The experimental matrix was synthetic opal grown at the Physicotechnical Institute by a method similar to that described in Ref. 4. We used the property of opal to diffract visible light to select a sample close to single-crystal, into which tellurium (Te) (melting point ~450 °C) was introduced under pressure from a melt. Since we are interested in the state of the tellurium in the voids, the surface layer of the sample, consisting mainly of polycrystalline Te, was removed with polishing paper with an abrasive grain size of ~5 μm. The sample was then washed in distilled water and dried with filter paper. Pieces were cleaved from the sample and ground mechanically, and the finest fraction of the powder was deposited on a copper grid (100 mesh/mm).

An EM 4000 EX electron microscope with an accelerating voltage of 400 kV was used because of the strong electron absorption by tellurium ($z=52$).

Figure 1 shows a model of the void sublattice (cluster lattice) for cubic-packed spheres in the (100) projection. To develop this model, the tetrahedral voids were approximated by tetrahedra and the octahedral ones by cubes, where, following the geometry, the cross section of the tetrahedra was approximately twice that of the cubes. In this approximation, for the (100) projection both types of voids, and therefore clusters, will be seen as squares of different size, oriented with their sides parallel. If the proposed model is implemented in a real volume with a filler, electron microscopic images for the (100) projection of the opal matrix should show the Te clusters as ordered squares whose sizes differ by about a factor of 2.

Since the method of preparing the sample for examination did not allow the orientation of the powder to be fixed, the observed images corresponded to different projections of the opal matrix. Thus, the observation of cluster images with the required orientation depended to some extent on the position. Using a goniometer did not help because this could only measure the orientation of the powder to within 20°.

As a result of the large difference in the absorption of electrons by the elements contained in the sample, the Te clusters will be imaged as dark squares against a background of lighter SiO_2 spheres. Figure 2 shows an electron microscopic image of opal powder with a Te filler. The configuration of dark cluster squares corresponds to the (100) projection of the cluster lattice model in the opal matrix (Fig. 1). The real shape of the clusters on the image, having concave-sided squares, differs from the model since it is caused by the curvature of the SiO_2 sphere, and this indicates complete filling of the voids by Te. The figure also shows that the clusters are connected by ''bridges'' of the same dark contrast. These images confirm that under the influence of pres-

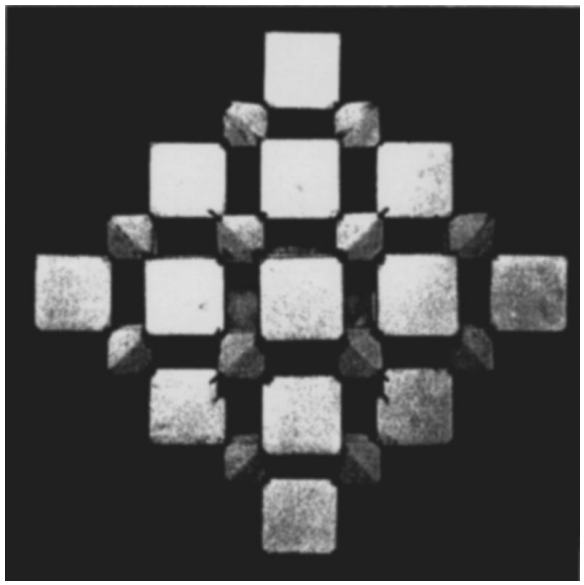

FIG. 1. Model of cluster lattice consisting of octahedral (O) and tetrahedral (T) voids in an opal matrix comprising cubic close-packed SiO_2 spheres. (100) projection.

sure, the Te from the melt fills all voids and the pores are interconnected via a labyrinth of channels. Although the channels have very small cross sections, providing a high flow resistance, the tellurium ''seeps'' through the capillary channels to fill the neighboring voids.

A microdiffraction analysis was made of the observed set of clusters in an opal matrix. This yielded point electron diffraction patterns, which are interpreted as tellurium with the standard lattice parameters ($a=0.4457$ nm, $b=0.5929$ nm) (Ref. 5). Point electron diffraction patterns were obtained for various sections of the cluster lattice within an area of a few square microns. An example of one of these diffraction patterns is shown in the inset to Fig. 2. The patterns were characterized by the same crystallographic zone and the same azimuthal orientation in the plane of this zone. This indicates that the clusters crystallize with a single-crystal structure, not only within a single cluster but over a fairly large area, and neighboring clusters have the same crystallographic orientation. This behavior suggests that as the system cools down after tellurium has been introduced, it undergoes directional crystallization in the voids and systematically envelops one cluster after another via the narrow channels. Clear confirmation of this mechanism for solidifying of Te in opal voids is provided by high-resolution electron microscopic images of the sample. These images clearly show that the (0001) atomic planes of Te with $d=0.5929$ nm in neighboring clusters are parallel to these planes in the bridges, i.e., a common single-crystal structure is maintained in the clusters and in the intervening compounds.

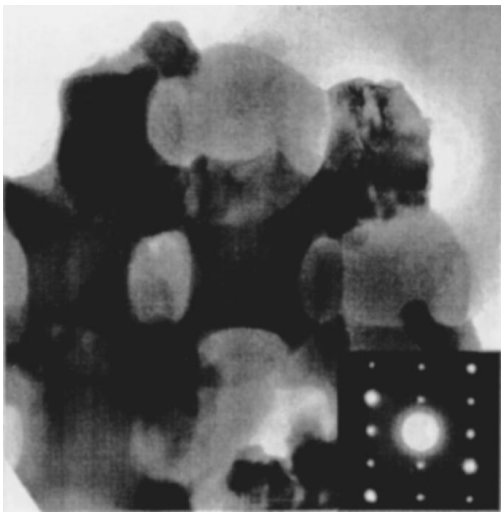

FIG. 2. Electron-microscopic image of tellurium clusters (O and T) forming an ordered three-dimensional lattice in an opal matrix (A-spheres of SiO_2). The inset shows a microdiffraction pattern with the $(1\bar{2}10)$ orientation, obtained with parallel-oriented tellurium clusters.

The system formed by clusters in an opal matrix may be treated as a set of Schottky diodes. These results then demonstrate that, in principle, it is possible to obtain a new type of medium consisting of a system of parallel-oriented Schottky diodes.

To sum up, we can conclude that:

1. The incorporation of tellurium into the pores in opal forms a three-dimensional cluster lattice. The spatial configuration of these clusters is a copy of the regularly distributed voids in the opal matrix.

2. The tellurium fills the entire volume of the void so that the cluster acquires the shape of the void.

3. Tellurium clusters have a single-crystal structure where neighboring clusters maintain the same crystallographic orientation, which is achieved by directional crystallization via the channels between amorphous SiO_2 spheres.

4. It has been demonstrated for the first time that in principle it is possible to obtain a three-dimensional superlattice in an opal matrix consisting of parallel-oriented single-crystal Te clusters.

This work was partially supported by the Russian Fund for Fundamental Research, Grant N 96-02 16948-a.

[1] V. G. Balakirev, V. N. Bogomolov, V. V. Zhuravlev *et al.*, Kristallografiya **36**, 111 (1993) [Crystallogr. Rep. (1993)]
[2] V. N. Bogomolov and T. M. Pavlova, Fiz. Tekh. Poluprovodn. **29**, 826 (1995) [Semiconductors **29**, 428 (1995)].
[3] V. N. Bogomolov, S. A. Ktitorov, D. A. Kurdyukov *et al.*, Pis'ma Zh. Éksp. Teor. Fiz. **61**, 738 (1995) [JETP Lett. **61**, 753 (1995)].
[4] W. Stober, A. Fink, and E. Bohn, J. Colloid Interface. Sci. **26**, 62 (1968).
[5] A. Guinier, *Théorie et Technique de la Radiocristallographie* (Dunod, Paris, 1956) [Russ. transl, Fizmatgiz, Moscow, 1961)].

Translated by R. M. Durham

Excitation of ray oscillations in quasioptical dielectric cavities with whispering gallery modes

S. N. Khar'kovskiĭ, A. E. Kogut, and V. V. Kutuzov

Institute of Radio Engineering and Electronics, Ukrainian National Academy of Sciences, Kharkov
(Submitted January 6, 1997)
Pis'ma Zh. Tekh. Fiz. **23**, 25–29 (August 12, 1997)

It is observed that ray oscillations may be excited together with whispering gallery modes in quasioptical dielectric cavities. It is shown that as the excitation conditions change, the fields of these oscillations gradually ''split off'' from the fields of the whispering gallery modes whose characteristics deteriorate. The angular spectrum of ray oscillations in dielectric cavities is determined. © *1997 American Institute of Physics.* [S1063-7850(97)00508-9]

The phenomenon of high-Q resonance of whispering gallery modes in dielectric solids of revolution is used over a wide range of frequencies between the microwave and the optical.[1,2] In quasioptical dielectric cavities where the radius R is related to the wavelength λ_d by $R>5\lambda_d$ the field of these modes is concentrated in a narrow band near the boundary of the dielectric between caustics of radii a and a_c (Fig. 1a) and may be described using the wave approach. At the same time, the geometric-optics approach indicates that oscillations may occur in these cavities for which the ray trajectory is a regular N-sided polygon inscribed within the cavity circumference (Fig. 1b). Unlike the whispering gallery modes, which are the result of diffraction and interference of waves from the source at a curvilinear boundary, these oscillations may be described using geometric optics and we shall therefore call them ray oscillations. As a result of an experimental study of quasioptical dielectric cavities in the millimeter wavelength range, we observed that both ray and whispering gallery oscillations can be excited simultaneously. This effect was particularly noticeable for weakly directional radiation sources (such as the open end of a cavity, coupling slit, and so forth). In order to determine the separability and mutual influence of these oscillations, we made specific studies of a quasioptical dielectric cavity where one half was replaced by a mirror with a coupling slit. Note that this problem goes back to studies on wave propagation near a curved solid surface[3,4] and was first formulated by us for whispering gallery modes in quasiopticalal dielectric cavities.

We present results of an investigation of a specular, hemispherical, quasiopticalal dielectric cavity containing plane reflectors *1* and *2* (Fig. 1c). One of these reflectors incorporates an exciting waveguide *3* which tapers smoothly along its narrow wall to an open end, forming a 7.2×1 mm slit on the surface of the reflector. The hemisphere *4* was made of Teflon-4 and its radius was $R=39$ mm. The characteristics of the TM_{nml} ($E_r\neq 0$) whispering gallery modes of this cavity for n, m, $l=1$ variations of the field along the polar, azimuthal, and radial coordinates, respectively were described in Ref. 5. Figure 2a gives the relative resonance amplitude A/A_m and its frequency variation Δf_m as a function of the normalized radial coordinate of the slit r_i/R ($n=37$, resonant frequency $f_n=36.6$ GHz). The coupling between the cavity and the supply waveguide was below critical because of the additional radiation losses caused by the bounded area of the mirrors, but at each point r_i the coupling was tuned to the maximum for the system by changing the position of mirror *2*. It can be seen that the resonance is excited continuously and efficiently over a wide range of r_i, which includes the radius of the internal caustic a of the whispering gallery modes (this is calculated below). As the slit is displaced, the amplitude, shape and width of the resonance vary. To identify the oscillations, we use the displacement of the mirror *2*, whose length along the radial coordinate of the cavity does not exceed the distance between the caustics of the whispering gallery modes. Figure 2b gives the relative resonance amplitude A/A_m as a function of the normalized radial coordinate r_0/R of the center of mirror *2* keeping the slit position fixed. For $r_i=38.5$ mm, the field spot lies on the radius between the whispering gallery caustics. As r_i decreases, the field spot ''spreads'' over the radius into the dielectric. For instance, at $r_i=35.5$ mm the field spot has expanded by 50% and forms the transition region from whispering gallery to ray oscillations. A further decrease in r_i leads to the formation of a resonant field for a specific position of the slit ($r_i=33$ mm) and this field spot splits off appreciably from the spot of the whispering gallery field and moves as a whole into the dielectric. An investigation of the field distribution along the polar coordinate shows that in its pure form, a ray oscillation is excited with N

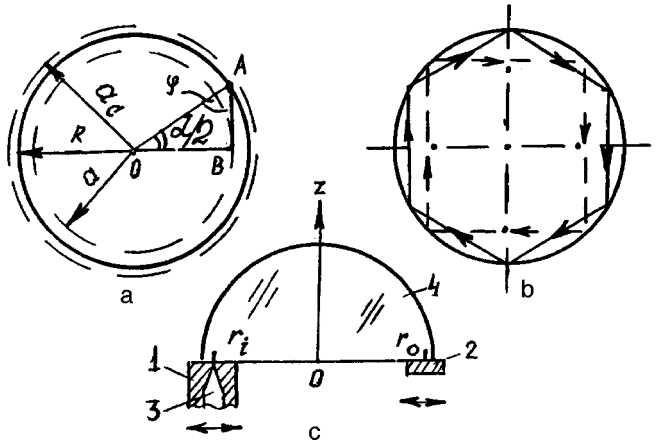

FIG. 1.

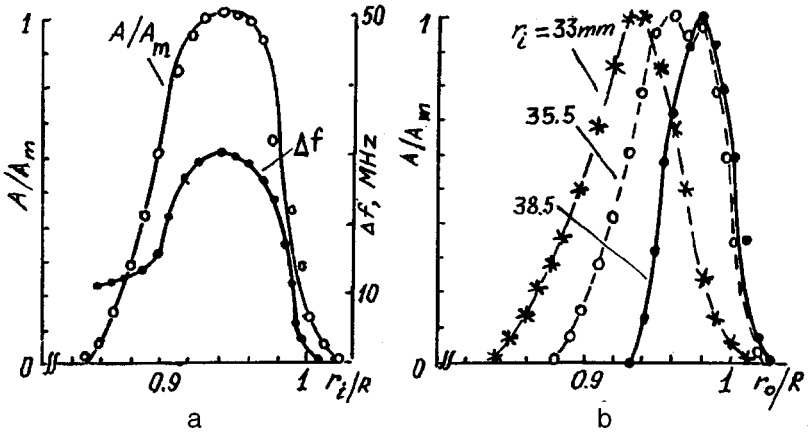

FIG. 2.

reflections from the concave surface of the dielectric. In this case $N=6$ and no ray oscillation is observed for other values of N.

The ray oscillations form an almost periodic sequence of resonances whose frequencies are similar to, and in some parts of the spectrum almost coincide with, the resonant frequencies of the whispering gallery oscillations. Their Q factor is 30% lower than that of the whispering gallery modes. The excitation of transient and/or ray oscillations leads to broadening and distortion of the resonance curve, radial blurring of the field spot of the whispering gallery modes, and causes additional modulation of their polar field distribution.

We determine the angular spectrum and number N of reflections of the ray from the surface of the dielectric for which pure ray oscillations can be excited in quasioptical dielectric cavities with whispering gallery modes. We confine ourselves to the first stage of the two-dimensional model of whispering galleries in a circle. Among the reflected waves contributing to the resonant field of the whispering gallery modes in quasioptical dielectric cavities, we single out the ray with the smallest number j of reflections. Its trajectory will obviously have the form of a rectangular j-sided polygon described around the inner caustic of the whispering gallery mode. The radius a of the inner whispering gallery caustic is given by:[6]

$$a=nc/2\pi f_n\sqrt{\varepsilon}, \tag{1}$$

where ε is the permittivity of the cavity material and c is the velocity of light in vacuum.

From the geometry of the problem (see ΔAOB in Fig. 1a, $\alpha/2=\pi/j$, $\varphi=\pi/2-\alpha/2$) and the condition for total internal reflection of the ray from the boundary of the dielectric, we find that the discrete angular spectrum φ_N of the ray oscillations lies in the range

$$\arcsin(1/\sqrt{\varepsilon})<\varphi_N<\pi/2-\arccos(nc/2\pi f_n\sqrt{\varepsilon}R). \tag{2}$$

The number N of reflections of the ray from the circular boundary of the dielectric corresponding to the ray oscillations, is determined from

$$\pi/[\pi/2-\arcsin(1/\sqrt{\varepsilon})]<N<\pi/\arccos(nc/2\pi f_n\sqrt{\varepsilon}R). \tag{3}$$

Note that in specular quasioptical dielectric cavities, the resonances form rays describing trajectories in the form of half N-sided polygons with even N.

In the experiment we have $R=39$ mm and $\varepsilon=2.04$. For $n=37$ and $f_n=36.6$ GHz, the calculated caustic radius is $a=37$ mm or $a/R=0.94$, which agrees with the experimental estimate of a. Equation (3) gives $4<N<8$, as was observed ($N=6$).

[1] V. B. Braginskiĭ, V. S. Il'chenko, and M. L. Gorodetskiĭ, Usp. Fiz. Nauk **160**, 157 (1990) [Sov. Phys. Usp. **33**, 87 (1990)].
[2] M. E. Il'chenko, V. F. Vzyatyshev, L. G. Gassanov *et al.*, in *Dielectric Cavities* [in Russian], edited by M. E. Il'chenko (Radio i Svyaz', Moscow, 1989).
[3] B. E. Kinber, Radiotekh. Elektron. **6**, 1273 (1961).
[4] V. M. Babich and V. S. Buldyrev, *Asymptotic Methods in Short-wave Diffraction Problems* [in Russian] (Nauka, Moscow, 1972).
[5] S. N. Khar'kovskiĭ, A. E. Kogut, and V. A. Solodovnik, Pis'ma Zh. Tekh. Fiz. **21**(18), 38 (1995) [Tech. Phys. Lett. **21**, 741 (1995)].
[6] S. N. Vlasov, Radiotekh. Elektron. **12**, 572 (1967).

Translated by R. M. Durham

Photorefractive slit waves

S. M. Shandarov and E. S. Shandarov

State Academy of Control Systems and Radioelectronics, Tomsk
(Submitted February 5, 1997)
Pis'ma Zh. Tekh. Fiz. **23**, 30–35 (August 12, 1997)

It is shown that photorefractive slit waves may exist, localized near a narrow gap between two similar photorefractive crystals with a diffusion mechanism of nonlinearity and oppositly directed polar axes. © *1997 American Institute of Physics.* [S1063-7850(97)00608-3]

Nonlinear self-channeling of beams in photorefractive crystals is observed at low optical intensities[1–7] and has therefore been studied in detail for some time. Self-channeling effects are specifically observed as the formation of spatial solitons when the diffraction-limited divergence of an optical beam is compensated by self-induced changes in the refractive index of the crystal.[1–3] The authors of Ref.4 predicted the existence of photorefractive surface waves in crystals with diffusion type of response. In this case, self-channeling occurs near one of the boundaries of a layer of finite thickness embedded in a dielectric of lower refractive index, or along the interface between two photorefractive crystals having nonlinearity parameters of opposite sign. Beam self-channeling effects near boundaries have been observed experimentally for photorefractive $BaTiO_3$ (Ref.5) and $Bi_{12}TiO_{20}$ crystals.[6]

Here we consider the possibility and fundamental characteristics of light self-channeling near a slit separating two similar photorefractive crystals with a diffusion response and oppositely directed polar axes. By analogy with similar waves of an acoustic nature in piezocrystals,[8,9] we shall call these photorefractive slit waves.

We consider a structure formed by two layers of thickness L, comprising identical photorefractive crystals with the refractive index n_2, and separated by a linear dielectric layer of thickness $2h$ with the refractive index $n_1<n_2$ (Fig. 1). We shall assume that the polar axes of the crystals are in opposite directions and the action of an optical beam with the intensity distribution $I(x)$ produces a steady-state space charge field as a result of the diffusion mechanism

$$E_{sc}(x)=\frac{k_BT}{e}\frac{1}{I}\frac{dI}{dx}, \tag{1}$$

where k_B is the Boltzmann constant, T is the absolute temperature, and e is the electron charge. Relation (1) was derived neglecting the dark conduction of the medium and agrees with the well-known logarithmic model of photorefractive nonlinearity.[4,5,7] If the thickness of the layer separating the crystals is substantially greater than the wavelength of light ($2h>\lambda$), the optical fields in the crystals are not coupled. This case corresponds to the photorefractive, TE-polarized, surface waves considered in Refs. 4 and 5 where, for a solution in the form $E_y(x,z)=A(x)\exp(i\beta z)$, the Schrödinger equation for the transverse field distribution is linearized:

$$\frac{d^2A}{dx^2}+(k_2^2-\beta^2)A+2q\frac{dA}{dx}=0, \tag{2}$$

where $k_2=(2\pi/\lambda)\,n_2$, β is the propagation constant, and the photorefractive nonlinearity parameter q is defined in terms of the effective electrooptic constant r_{eff} by

$$q=\left(\frac{2\pi}{\lambda}n_2^2\right)^2 r_{\text{eff}}\frac{k_BT}{e}. \tag{3}$$

For a crystal of thickness $L\leqslant 1/q$, a photorefractive surface wave exists throughout the bulk and the spectrum of propagation constants β_m is discrete. In thick samples where $L\gg 1/q$, the field of this wave is localized near one of the boundaries. The propagation constant can then have any value in the range defined by

$$\sqrt{k_2^2-q^2}>\beta>\frac{2\pi}{\lambda}n_1. \tag{4}$$

Bringing the crystals closer so that $2h<\lambda/2$, leads to appreciable interpenetration of the fields of the photorefractive surface waves and exchange of optical energy between the crystals. For thin crystals ($L\leqslant 1/q$), assuming for simplicity metallized crystal boundaries $x=\pm(h+L)$, we obtained the following expressions for the transverse distribution of the optical field in a photorefractive slit wave:

$$A(x)=\exp[q(h+x)]\sin[\chi(h+L+x)],\quad \text{for } -h\geqslant x\geqslant -(h+L), \tag{5a}$$

$$A(x)=A_0[\exp(\gamma_0 x)\pm\exp(-\gamma_0 x)],\quad \text{for } h\geqslant x\geqslant -h, \tag{5b}$$

$$A(x)=\pm\exp[-q(x-h)]\sin[\chi(L+h-x)],\quad \text{for } L+h\geqslant x\geqslant h, \tag{5c}$$

where $A_0=[\chi\cos(\chi L)+(\gamma_0+q)\sin(\chi L)]\exp(\gamma_0 h)/\gamma_0$, $\chi=\sqrt{k_2^2-\beta^2-q^2}$ is the transverse propagation constant for the fields in the photorefractive layers, and $\gamma_0=\sqrt{\beta^2-(2\pi n_1/\lambda)^2}$ is the decay constant of the field in the slit between the crystals. The plus and minus signs in the second and third equations correspond to the symmetric and antisymmetric modes of the slit waves. The dispersion equations for these modes define a discrete spectrum of transverse propagation constants, and may be obtained in the form

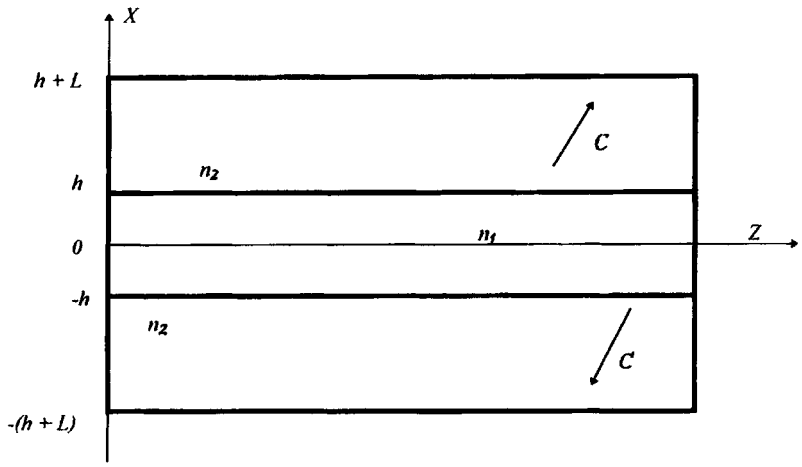

FIG. 1. Structure formed by two identical photorefractive crystals separated by a dielectric layer with the refractive index n_1. The C polar axes of the crystals are in opposite directions.

$$[\chi\cos(\chi L)+(\gamma_0+q)\sin(\chi L)] = \pm\exp(-2\gamma_0 h)[(\gamma_0-q)\sin(\chi L)-\chi\cos(\chi L)]. \tag{6}$$

Self-channeling may also take place along the twinning or domain boundaries of the crystal for $h=0$ (Ref. 4). The transverse propagation constants for the antisymmetric propagation mode are then expressed in explicit form from the dispersion equation (6)

$$\chi_{asm}=m\frac{\pi}{L}, \quad m=1, 2, 3, \ldots, \tag{7}$$

and for the symmetric mode

$$\chi_{sm}L-\arctan\frac{q}{\chi_{sm}}=(2m-1)\frac{\pi}{2}. \tag{8}$$

Figure 2 shows the transverse distributions of the optical field ($\lambda=633$ nm) for the symmetric and antisymmetric $m=5$ modes in a structure with the parameters $L=20$ μm and $h=0$. For the calculations, we used values of the refractive index and the electrooptic constant $n_2=2.4$ and $r_{\text{eff}}=10^{-9}$ m/V, typical of a 45° cut $BaTiO_3$ crystal in which the existence of photorefractive surface waves has been confirmed experimentally.[5] Note that the photorefractive nonlinearity parameter in this case is $q\approx 0.08$ μm^{-1}. For an air gap between the crystals ($n_1=1$), the decay constant is $\gamma_0\sim 20$ μm^{-1} and for $h\geqslant\lambda/4$ the optical field distribution in both cases corresponds to photorefractive surface waves.

In the limiting case of thick samples, $L\gg 1/q$, the transverse distribution of the optical field in the antisymmetric mode of the photorefractive slit wave may be given by

$$A_{as}(x)=\exp[q(h\pm x)]\sin\left[\chi(x\pm h) \mp\arctan\frac{\chi\sinh(\gamma_0 h)}{\gamma_0\cosh(\gamma_0 h)+q\sinh(\gamma_0 h)}\right], \tag{9}$$

where the upper and lower plus or minus signs correspond to the structure layers $x\leqslant -h$ and $x\geqslant h$. For the symmetric mode, the distribution $A_s(x)$ in these structure layers is expressed as

$$A_s(x)=\exp[q(h\pm x)]\sin\left[\chi(h\pm x) -\arctan\frac{\chi\cosh(\gamma_0 h)}{\gamma_0\sinh(\gamma_0 h)+q\cosh(\gamma_0 h)}\right]. \tag{10}$$

For the discrete spectrum of propagation constants, the optical field distribution in the gap between the crystals, $A(x)$, is described by Eq. (5b). The amplitude of the field for the antisymmetric and symmetric modes, A_{0as} and A_{0s}, may be obtained from Eqs. (9) and (10) for $x=h$. Figure 3 shows

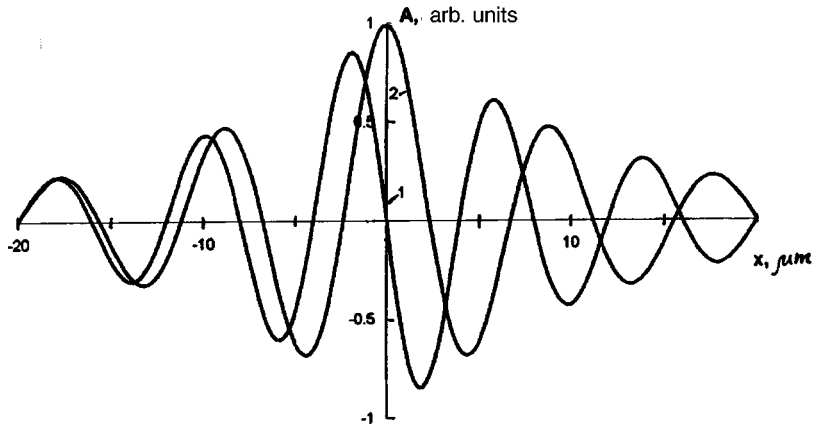

FIG. 2. Optical field distribution for the antisymmetric (*1*) and symmetric (*2*) $m=5$ modes of a photorefractive wave propagating along the interface between the crystals (Fig. 1, $h=0$). The $x=\pm 20$ μm crystal faces are metallized.

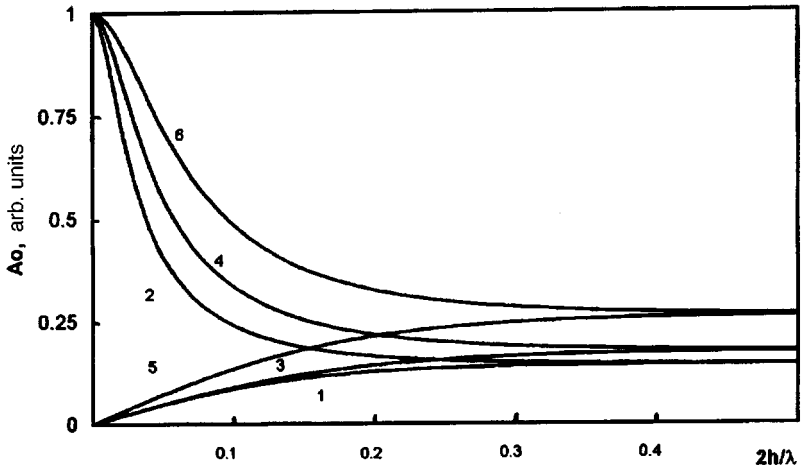

FIG. 3. Amplitudes A_{0as} and A_{0s} of the field for the antisymmetric (*1*, *3*, and *5*) and symmetric (*2*, *4*, *6*) modes of a photorefractive slit wave in the gap between the crystals as a function of its relative width $2h/\lambda$ for various values of the refractive index n_1 of the separating dielectric and the transverse propagation constant χ: *1*, *2* — $n_1=1$, $\chi=\pi$; *3*, *4* — $n_1=1.6$, $\chi=\pi$; *5*, *6* — $n_1=1.6$, and $\chi=1.5\pi$.

the amplitude of the field in the gap between the crystals as a function of $2h/\lambda$. For $h>0$ the amplitude of the field in the gap increases with the refractive index n_1 of the dielectric filler material and with the transverse propagation constant χ of the photorefractive slit wave.

To sum up, photorefractive slit waves localized near the gap separating the crystals can propagate in a structure formed by two similar photorefractive crystals with a diffusion response and having oppositely directed polar axes.

[1] G. C. Duree Jr., J. L. Schultz, G. J. Salamo *et al.*, Phys. Rev. Lett. **71**, 533 (1993).
[2] M. Taya, M. C. Bashaw, M. M. Fejer *et al.*, Phys. Rev. A **52**, 3095 (1995).
[3] M. Morin, G. Duree, G. Salamo, and M. Segev, Opt. Lett. **20**, 2066 (1995).
[4] G. S. Garcia Quirino, J. J. Sanchez-Mondragon, and S. Stepanov, Phys. Rev. A **51**, 1571 (1995).
[5] M. Cronin-Golomb, Opt. Lett. **20**, 2075 (1995).
[6] A. A. Kamshilin, E. Raita, V. V. Prokofiev, and T. Jaaskelainen, Appl. Phys. Lett. **67**, 3242 (1995).
[7] O. V. Lyubomudrov and V. V. Shkunov, Kvantovaya Elektron. (Moscow) **19**, 1199 (1992) [Sov. J. Quantum Electron. **22**, 1121 (1992)].
[8] Yu. V. Gulyaev and V. P. Plesskiĭ, Usp. Fiz. Nauk **157**(1), 85 (1989) [Sov. Phys. Usp. **32**, 51 (1989)].
[9] M. K. Balakirev and I. A. Gilinskiĭ, *Waves in Piezoelectric Crystals* [in Russian] (Nauka, Moscow, 1982).

Translated by R. M. Durham

Compensation of excess noise in a fiber-optic gyroscope with a 3×3 directional coupler

É. I. Alekseev and E. N. Bazarov

Institute of Radio Engineering and Electronics, Russian Academy of Sciences, Fryazino
(Submitted March 6, 1997)
Pis'ma Zh. Tekh. Fiz. **23**, 36–38 (August 12, 1997)

It is shown theoretically that the excess noise of the radiation source can be compensated in a fiber-optic gyroscope with a 3×3 ring directional coupler and a differential amplifier at the exit. This noise is one of the main factors limiting the precision of a fiber-optic gyroscope. © *1997 American Institute of Physics.* [S1063-7850(97)00708-8]

One method of enhancing the precision of fiber-optic gyroscopes involves using superfluorescent fiber radiation sources.[1] These sources have properties similar to those of thermal sources and are characterized by a high level of excess noise. Experiments show that the excess noise predominates over other noise sources at powers of the order of 10 mW at the photodetector.[2] Thus the problem of reducing the influence of this noise on the precision of gyroscopes is of major interest.

In coherent-optics communications excess heterodyne noise is suppressed by means of balanced detection.[3] Balanced detection can also be applied to fiber-optic gyroscopes, by using the source radiation, delayed by the time taken for the light to propagate in the optical channel of the fiber-optic gyroscopes, as the reference signal. However, the implementation of balanced detection in the usual ''minimal'' configuration of fiber-optic gyroscopes with input and 2×2 ring directional couplers is fraught with difficulties associated with achieving coherent interaction between the information and reference signals. Here we show that the problem can be resolved considerably more simply by incorporating a 3×3 directional coupler in the fiber-optic gyroscope configuration.

Figure 1 shows a simplified configuration of a fiber-optic gyroscope with a 3×3 directional coupler. Radiation from a source *3* passes through a 3×3 coupler *4* to the input of a sensing ring *5* and then to photodetectors *1* and *2*, whose outputs are connected to a differential amplifier *6*. Although this type of fiber-optic gyroscope configuration was encountered earlier in Refs. 4 and 5, as far as we are aware, the problem of excess noise has not so far been addressed.

Each of the counterpropagating waves L and S in the circuit (see Fig. 1) is simultaneously an information-carrying (signal) wave and a reference wave for the other wave, and apart from a multiplicative factor (we shall subsequently omit this reservation), we have for an ideal directional coupler:

$$L = A\ \exp(i\varphi)\exp(-i\varphi_0),$$

$$S = A\ \exp(i\varphi)\exp(i\varphi_0). \tag{1}$$

Here A and φ are the amplitude and phase of the waves, respectively, and φ_0 is the nonreciprocal (Sagnac) phase shift.

The signals reaching the photodetectors are:

$$E_1 = S + \exp(i\varphi_1)L,$$

$$E_2 = L + \exp(i\varphi_1)S, \tag{2}$$

where φ_1 is the phase difference between the signals propagating through the directional coupler via the ''forward'' and ''cross'' channels.

The photodetector currents (which are assumed to be identical) are given by:

$$I_1 = |S|^2 + |L|^2 + \exp(i\varphi_1)LS^* + \exp(-i\varphi_1)SL^* + n_1,$$

$$I_2 = |S|^2 + |L|^2 + \exp(i\varphi_1)SL^* + \exp(-i\varphi_1)LS^* + n_2, \tag{3}$$

where n_1 and n_2 are the photodetector noise.

At the exit from the differential amplifier we have

$$I_{\text{out}} = 2|A|^2\ \sin\ \varphi_1 \cdot \sin(2\varphi_0) + n_1 - n_2. \tag{4}$$

Thus the excess noise caused by the background illumination of the photodetectors is compensated. It also follows from Eq. (4) that a fiber-optic gyroscope with a 3×3 directional ring coupler and balanced detection operates in a quadrature mode and its optical scale factor is the same as that for the minimal configuration, although the electrical scale factor is smaller, since $\varphi_1 \neq \pi/2$.

This configuration is of interest for low- and moderate-precision fiber-optic gyroscopes. A modified minimal configuration with a 3×3 directional coupler can be used for high-precision fiber-optic gyroscopes.

The authors would like to thank V. P. Gubin and N. I. Starostin for useful discussions.

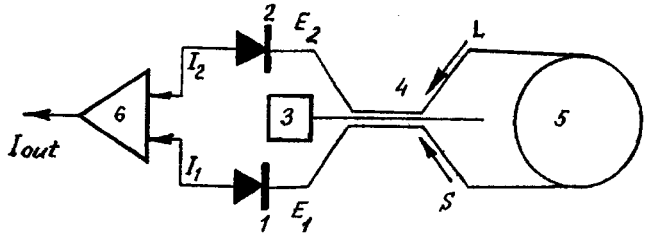

FIG. 1. Diagram of fiber-optic gyroscope with 3×3 coupler.

This work was supported by the Russian Fund for Fundamental Research, Grant No. 96-02-18434.

[1] P. E. Wysocki, M. J. F. Digonnet, B. J. Kim, and H. J. Shaw, J. Lightwave Technol. **12**, 550 (1994).
[2] W. K. Burns, R. P. Moeller, and A. Dandridge, IEEE Photon. Technol. Lett. **2**, 606 (1990).
[3] R. Sterlin, R. Batting, P. D. Heinchoz, and H. P. Weber, Opt. Quantum Electron. **18**, 445 (1986).
[4] W. K. Burns, R. P. Moeller, and C. A. Villarruel, Electron. Lett. **18**, 648 (1982).
[5] H. Poisel, G. F. Trommer, W. Bühler *et al.*, Electron. Lett. **26**, 69 (1990).

Translated by R. M. Durham

2.2 μm cw single-mode diode lasers with thermoelectric cooling

A. A. Popov, V. V. Sherstnev, and Yu. P. Yakovlev

A. F. Ioffe Physicotechnical Institute, Russian Academy of Sciences, St. Petersburg
(Submitted April 7, 1997)
Pis'ma Zh. Tekh. Fiz. **23**, 39–45 (August 12, 1997)

Continuous-wave lasing in the 2.2 μm region is reported for single-mode GaAlAsSb/GaSb/GaInAsSb double-heterostructure diode lasers with thermoelectric cooling. The temperature dependences of the threshold current near room temperature are investigated for the cw and pulsed pumping regimes. A record characteristic temperature $T_0=132$ K has been achieved.
 [S1063-7850(97)00808-2]

Single-mode infrared semiconductor lasers are an invaluable source of tunable radiation with a high spectral power density for the detection of various molecular components by tunable diode laser adsorption spectroscopy (TDLAS) with a detection limit of 10^{-9}–10^{-12} (Refs. 1 and 2). The range near 2.2 μm is particularly promising for the detection of nitrogen-containing molecules such as N_2O, NO_2, and others.[3] Lasers utilizing strained InGaAs/InP heterostructures have been successfully grown for wavelengths shorter than 2.0 μm (Ref. 4). The development of longer-wavelength sources involves using narrow-gap GaInAsSb/GaSb solid solutions.[5–7] Lasing at 2.1 μm in GaInAsSb multi-quantum-well lasers with a broad stripe and a characteristic temperature of 110–115 K ($T<40$ °C) was reported in Refs. 8 and 9. Single-mode lasing in GaInAsSb lasers was studied in Refs. 10 and 11. The wavelength range of this type of laser was recently extended to 2.7 μm (Refs. 12 and 13). These semiconductors are the most attractive material for the development of diodes operating in the range of stronger absorption lines, which can enhance the detection sensitivity by two orders of magnitude. The requirement for single-frequency cw lasing with thermoelectric cooling is one of the major constraints imposed on laser diodes for spectral applications.[1]

In this article we report single-mode cw lasing in thermoelectrically cooled GaInAsSb semiconductor lasers in the 2.2 μm wavelength range. The temperature dependence of the threshold current was investigated for the cw and pulsed modes and a characteristic temperature as high as $T_0=132$ K was achieved for the first time, this being the highest known for this type of narrow-gap semiconductor laser.

Double heterostructure lasers with an n-GaInAsSb active region were investigated. The active region was bounded symmetrically on both sides by GaAlAsSb emitter layers. A deep mesa stripe structure with a stripe width of 6–10 μm prepared by photolithography provided the lateral confinement. A p-GaSb layer was used as the contact layer. The GaInAsSb active layer had an indium content of 0.16 ($E_g=0.64$ eV) and was doped with Te to a concentration of $(1–2)\times10^{17}$ cm^{-3}. The wide-gap n- and p-type GaAlAsSb layers adjacent to the active region had an Al content of 0.50 ($E_g=1.11$ eV) and were doped with Te and Ge to concentrations of $(2–4)\times10^{18}$ cm^{-3} and $(6–8)\times10^{18}$ cm^{-3}, respectively. The thickness of the active region was 1.0 μm, the GaAlAsSb layers were each 2.5 μm thick, and the contact layer was 0.8 μm thick. The structures were grown by liquid-phase epitaxy. Laser diodes with a 150–350 μm Fabry–Perot cavity were formed by cleaving and were attached by the substrate to a TVZ-1.3 three-stage thermoelectric cooler mounted in a standard SDL-3050 casing (Fig. 1). The peak heat-transfer power was limited to 3.5 W. The casing also contained a 500 μm diameter feedback photodiode, fabricated from a GaInAsSb solid solution, and a temperature-stabilizing thermistor.

The lasers were tested at the operating temperatures of the Peltier cooler in the cw and pulsed pumping modes. Pulsed lasing with a low inverse duty cycle, and also the results of low-temperature measurements obtained with cryogenic cooling, were used to make a comparative study of the temperature dependence of the threshold current. The pulse length was 100 ns and the inverse duty cycle 10^{-5}. The optical signal was detected by a GaInAsSb photodetector and amplified by a differential amplifier with a 30 ns response time. The radiation spectrum was monitored using an MDR-2 monochromator with a resolution better than 0.5 ns. Single-frequency lasers emitting in the 2.2 μm range at room temperature were selected.

Continuous-wave lasing was observed up to -24 °C. Lasing at higher temperatures was limited by the power of the thermoelectric cooling system and by the thermal conductivity of the laser crystal. At all the test temperatures, the lasing was single-mode up to pump currents 2.5 times higher than the lasing threshold I_{th}. With increasing temperature a long-wavelength shift of the emitted mode was observed at an average rate of -2.4 cm^{-1}/K, which is similar to the temperature dependence of the band gap. As the temperature varied, mode jumps were observed to the neighboring long-wavelength mode, separated by an intermode spacing of ~6.7 cm^{-1}.

The temperature dependence of the threshold current is plotted in Fig. 2. In the cw mode, the threshold current increased from ~53 mA at -194 °C to 440 mA dc at -24 °C. The measurements revealed an exponential increase in the threshold current with temperature. The characteristic temperature T_0 was 85 K for the range between -194 °C and -30 °C and 33 K above -30 °C. A bend was observed on the characteristic near ~-30 °C.

To study the physical factors limiting the range of operating temperatures, we consider characteristic features of the temperature dependence of the threshold lasing current for

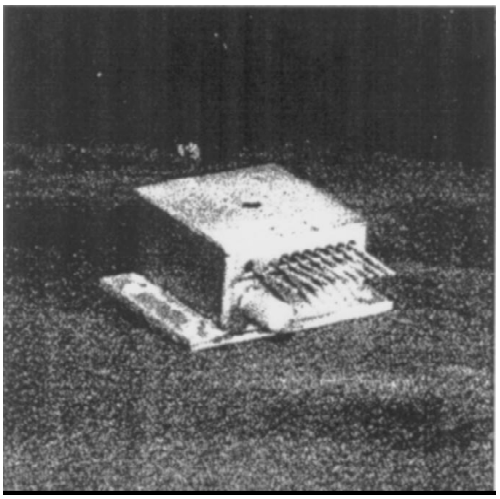

FIG. 1. External view of LD22 (V22716) laser diode mounted in a standard SDL-3050 hermetically sealed casing. The casing also contains a TVZ-1.3 three-stage thermoelectric cooler, a GaInAsSb feedback diode 500 μm in diameter, and a temperature-stabilizing thermistor. The right of the figure shows the cw lasing spectrum recorded at -35°C. The pump current was 300 mA dc.

pumping by short laser pulses with a low inverse duty cycle (pulse length ~ 100 ns, inverse duty cycle $\sim 10^{-5}$). The most significant differences from the cw mode are as follows. Over the entire range of measured temperatures the lasing threshold was observed at lower pump currents and the difference increased with temperature. The maximum lasing temperature was substantially higher, $+84$ °C. The characteristic temperature T_0 for the two sections was significantly higher, at 132 and 65 K. The bend on the temperature dependence of the threshold current was shifted to $+62$°. We especially note that the characteristic temperature $T_0 = 132$ K was the highest reported so far for GaInAsSb lasers. We should also like to stress that this value is higher than the characteristic temperature $T_0 = 110$ K obtained for a 2 μm InGaAs/InP laser.[4]

We now analyze the possible losses limiting the operating temperature of 2.2 μm single-mode GaInAsSb semiconductor lasers. A theoretical analysis of the possible nonradiative losses influencing the threshold current and maximum lasing temperature of GaInAsSb lasers was reported earlier in Ref. 14. It was shown that at temperatures between -208 °C and $+30$ °C, the temperature dependence of the threshold current density corresponds to three mechanisms for recombination of nonequilibrium charge carriers in the active region. Up to -70 °C, radiative recombination predominates, between -70 °C and $+20$ °C CHHS Auger recombination is the dominant mechanism, and above $+20$° the CHCC Auger process predominates. The current dependence of the threshold current for pulsed pumping is broadly consistent with this model. However, the results obtained by us for cw lasing exhibit appreciable differences. A comparative analysis (Fig. 2) indicates that the inverse duty cycle of the pump current strongly influences the nonradiative losses in GaInAsSb. It was shown in Ref. 15 that the main factors limiting the power-current characteristic of narrow-gap semiconductor lasers are current heating of the active region by the Joule heat, hot carrier injection, Auger recombination, leakage across the heterobarrier, and absorption by free charge carriers. By analyzing the ratio of the characteristic nonradiative recombination times in GaInAsSb solid solutions, it was established[16] that the relaxation of the excess hot-carrier energy is determined by the interelectron interaction. Under our experimental conditions, the pump pulse length was greater than the characteristic recombination times in GaInAsSb[16] and the temperature tuning of the lasing wavelength corresponds to the temperature coefficient of the active-region band gap. Thus these results should be attributed to overheating of the active region which is one of the main factors suppressing cw lasing near room temperature. This temperature dependence of the threshold current yields the important conclusion that Auger processes, hot carrier injection, and carrier leakage across the heterobarrier do not make a significant contribution to the heating when deter-

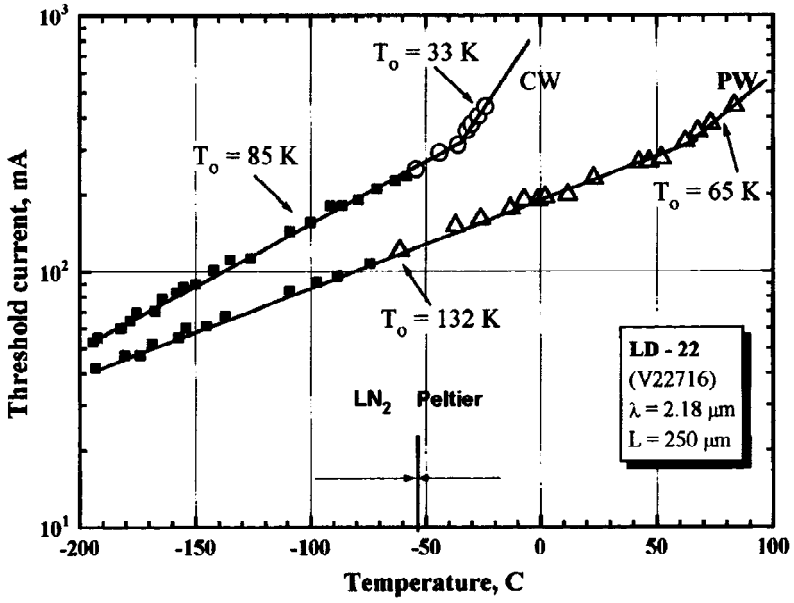

FIG. 2. Temperature dependence of the threshold current of the diode laser obtained in the cw (CW) and pulsed (PW) lasing modes near room temperature. In the pulsed mode the pump pulse length was 100 ns and the repetition frequency was 10 kHz.

mining the maximum cw lasing temperature. The high pump densities heating the active region intensify the Auger recombination which equalizes the rates of nonradiative and radiative recombination and suppresses cw lasing in GaInAsSb heterostructures.

To conclude, we have developed thermoelectrically-cooled cw laser diodes operating in the 2.2 μm range. It has been shown that the main factor limiting the operating temperature of the cw lasing in single-mode GaInAsSb lasers is current heating of the active region. The highest characteristic temperature of the threshold current $T_0 = 132$ K ($T < 60$ °C) recorded so far was obtained for the pulsed mode.

[1] P. Werle, R. Muecke, and F. Slemr, Appl. Phys. B **57**, 131 (1993).
[2] R. U. Martinelli, Laser Focus World No. 3, 77 (1996).
[3] L. S. Rothman, R. R. Gamache, R. H. Tipping, C. P. Rinsland, M. A. H. Smith, D. C. Benner, D. V. Malathy, J.-M. Flaud, C. Camy-Peyret, A. Perrin, A. Goldman, S. T. Massie, L. R. Brown, and R. A. Toth, J. Quant. Spectrosc. Radiat. Transfer **48**, 469 (1992).
[4] S. Forouhar, A. Ksendzov, A. Larsson, and H. Temkin, Electron. Lett. **29**, 574 (1993).
[5] C. Caneau, J. L. Zyskind, J. W. Sulhoff, T. E. Glover, J. Centanni, C. A. Burrus, A. G. Dentai, and M. A. Pollack, Appl. Phys. Lett. **51**, 764 (1987).
[6] A. E. Bochkarev, L. M. Dolginov, A. E. Drakin, P. G. Eliseev, and B. N. Sverdlov, Kvantovaya Elektron. (Moscow) **15**, 2171 (1988) [Sov. J. Quantum Electron. **18**, 1362 (1988)].
[7] A. N. Baranov, T. N. Danilova, B. E. Dzhurtanov, A. N. Imenkov, S. O. Konnikov, A. M. Litvak, V. E. Umanskiĭ, and Yu. P. Yakovlev, Pis'ma Zh. Tekh. Fiz. **14**, (1988) [Sov. Tech. Phys. Lett. **14**, 727 (1988)].
[8] A. N. Baranov, C. Fouillant, P. Grunberg, J. L. Lazzari, S. Gaillard, and A. Joullie, Appl. Phys. Lett. **65**, 616 (1994).
[9] H. K. Choi and S. J. Eglash, Appl. Phys. Lett. **61**, 1154 (1992).
[10] H. K. Choi, S. J. Eglash, and M. K. Connors, Appl. Phys. Lett. **63**, 3271 (1993).
[11] A. N. Imenkov, B. S. Kondrat'ev, A. A. Popov, and Yu. P. Yakovlev, Pis'ma Zh. Tekh. Fiz. **19**(23), 13 (1993) [Tech. Phys. Lett. **19**, 743 (1993)].
[12] A. N. Baranov, V. V. Sherstnev, C. Alibert, and A. Krier, J. Appl. Phys. **79**, 3354 (1996).
[13] D. Z. Garbuzov, R. U. Martinelli, R. J. Menna, P. K. York, H. Lee, S. Y. Narayan, and J. C. Connolly, Appl. Phys. Lett. **67**, 1346 (1995).
[14] A. A. Andaspaeva, A. N. Baranov, B. L. Gel'mont, B. E. Dzhurtanov, G. G. Zegrya, A. N. Imenkov, Yu. P. Yakovlev, and S. G. Yastrebov, Fiz. Tekh. Poluprovodn. **25**, 394 (1991) [Sov. Phys. Semicond. **25**, 240 (1991)].
[15] G. L. Belenky, A. Kastalsky, S. Luryi, P. A. Garbinski, A. Y. Cho, and D. L. Sivco, Appl. Phys. Lett. **64**, 2247 (1994).
[16] N. M. Kolchanova, A. A. Popov, G. A. Sukach, and A. B. Bogoslavskaya, Fiz. Tekh. Poluprovodn. **28**, 2065 (1994) [Semiconductors **28**, 1137 (1994)].

Translated by R. M. Durham

Dielectric properties of planar structures based on ferroelectric $Ba_{0.5}Sr_{0.5}TiO_3$ films

B. M. Gol'tsman, V. V. Lemanov, A. I. Dedyk, S. F. Karmanenko, and L. T. Ter-Martirosyan

A. F. Ioffe Physicotechnical Institute, Russian Academy of Sciences, St. Petersburg; Petersburg State Electrical Engineering University
(Submitted April 7, 1997)
Pis'ma Zh. Tekh. Fiz. **23**, 46–52 (August 12, 1997)

An experimental investigation has been made of the dielectric properties of planar $Cu–Cr/Ba_{0.5}Sr_{0.5}TiO_3$ and $YBa_2Cu_3O_{7-\delta}/Ba_{0.5}Sr_{0.5}TiO_3$ structures in the temperature range 78–300 K. It is shown that the use of $YBa_2Cu_3O_{7-\delta}$ electrodes in $Ba_{0.5}Sr_{0.5}TiO_3$ film structures ensures that there is no dielectric hysteresis in the paraelectric phase. At the same time, the dielectric nonlinearity is preserved and the dielectric losses are reduced. © *1997 American Institute of Physics.* [S1063-7850(97)00908-7]

A comparative investigation is made of the dielectric properties of planar structures consisting of $Ba_{0.5}Sr_{0.5}TiO_3$ (BST) polycrystalline films with electrodes made of Cu–Cr, Ni, and the high-temperature oxide superconductor $YBa_2Cu_3O_{7-\delta}$ (YBCO).

Ferroelectric BST films were prepared on an α-Al_2O_3 substrate by rf magnetron sputtering in an argon and oxygen atmosphere, followed by annealing in oxygen at 1150 °C (Ref. 1). The thickness of the films was 1–1.2 μm and they had a polycrystalline structure.

The metal electrodes were deposited by thermal deposition in vacuum. The high-temperature superconductor electrodes were deposited by dc magnetron sputtering. The thickness of the YBCO films was 0.4 μm and the transition temperature was in the range 83–90 K, with the width not exceeding 1–2 K. Contacts were applied to the YBCO electrodes by thermal evaporation of Ag in vacuum. The planar electrodes were prepared by liquid photolithography. The width of the gaps was $s = 5–10$ μm and the length varied in the range $l = 0.1–2.5$ mm (Fig. 1). Up to thirty two individual elements were formed on one 10×10 mm substrate.

Measurements were made of the temperature dependences of the capacitance C and tan δ at 1 MHz in the range 78–300 K, and the capacitance-voltage characteristics were also measured at 78 K and 300 K at voltages between -150 and $+150$ V. Approximately thirty samples of each structure with different electrode materials were prepared and used for the measurements.

The temperature dependences of the capacitance per unit length for planar structures with metal electrodes and YBCO electrodes revealed broad maxima at $T = 210–240$ K (Fig. 1) near the ferroelectric to paraelectric phase transition. The upper curve plotted in Fig. 1 for samples with Cu–Cr electrodes is typical for structures of this type. The capacitances for these samples differed by no more that 10% over the entire temperature range. The capacitances of the structures with YBCO electrodes were invariably lower and the spread of values between different samples was considerably greater than for structures with metal electrodes. The two curves plotted in Fig. 1 delimit the range of capacitances for YBCO/BST structures, which is most likely attributable to the diffusion of components of the YBCO film into the BST as a result of the preparation process.

Figure 2 shows the influence of the electrode material on the dielectric hysteresis.[2] The capacitance-voltage characteristics of the structures with metal electrodes show dielectric hysteresis ($\Delta C/C_0$, where C_0 is the initial capacitance) in both the ferroelectric phase ($T=78$ K) and the paraelectric phase ($T=300$ K). Most ($\sim80\%$) YBCO/BST structures do not exhibit hysteresis in the paraelectric phase ($T=300$ K), regardless of the $C(T)$ curve. For samples with YBCO electrodes the dielectric hysteresis in the ferroelectric phase ($T=78$ K) is smaller than that in this phase for Cu–Cr/BST structures. The fact that some YBCO/BST samples exhibit hysteresis in the paraelectric phase can probably be attributed to chemical processes at the electrode–film interface.[3] The controllability of nonlinear capacitor structures can be conveniently characterized by the coefficient $K=C_0C(U_{max})$ ($U_{max}=|150$ V$|$) (Ref. 4). It should be noted that at 300 K the controllability of YBCO/BST structures with hysteresis-free characteristics remained almost the same ($K=1.34$) as that for Cu–Cr/BST structures ($K=1.43$), if the temperature dependence of the capacitance was described by the upper curve in Fig. 1. For samples whose temperature dependence was described by the lower curve (Fig. 1), the controllability was considerably poorer ($K=1.15$).

The dielectric loss tangent tan δ (Fig. 3) for structures with YBCO electrodes was smaller than that for samples with metal electrodes at all temperatures.

The substantial broadening of the $C(T)$ peaks for $Ba_{0.5}Sr_{0.5}TiO_3$ films has already been discussed by us in Ref. 1. The main reasons for these broad peaks may be the nonuniform composition over the thickness and area of the film, and also the elastic stresses in the film. Changing the electrode material has little influence on the width of the peaks for the $C(T)$ temperature curves. The observed decrease in the capacitance of YBCO/BST structures is probably caused by changes taking place in the BST film when the YBCO electrode is applied and during its subsequent storage.[3] In particular, some chemical interaction takes place between the BST and YBCO layers.[5] This is accompanied by a reduction

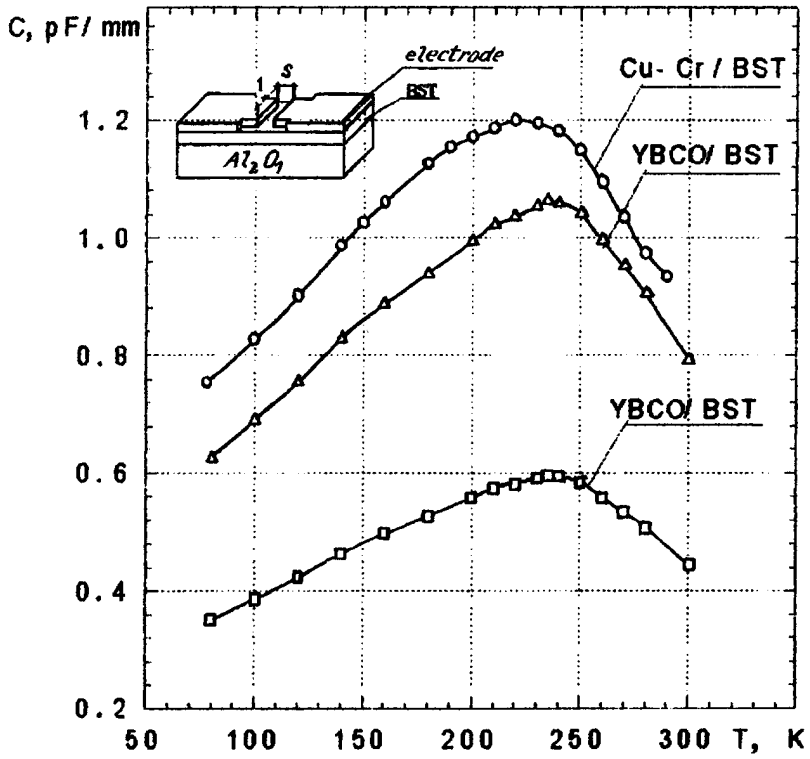

FIG. 1. Temperatures dependences of the capacitance of planar structures formed by $Ba_{0.5}Sr_{0.5}TiO_3$ films with Cu–Cr and YBCO electrodes.

in the effective capacitance of the entire structure and its corresponding permittivity. An approximate estimate of the permittivity of structures with metal electrodes at the operating temperature of 300 K gives $\varepsilon \cong 700$ (Ref. 1), whereas for structures with YBCO electrodes the permittivity is in the range $\varepsilon \cong$ 670–300. The upper limit corresponds to curve *2* and the lower limit to curve *3* (Fig. 1).

The use of YBCO electrodes influences the dielectric

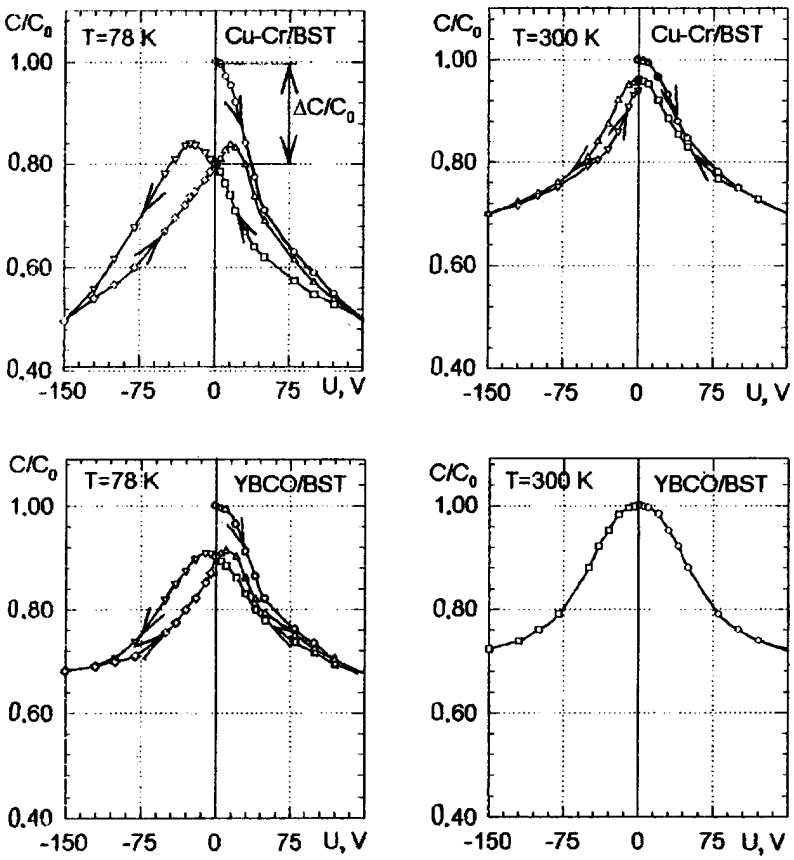

FIG. 2. Capacitance-voltage characteristics of planar structures with different electrode materials in the ferroelectric ($T = 78$ K) and paraelectric phases ($T = 300$ K).

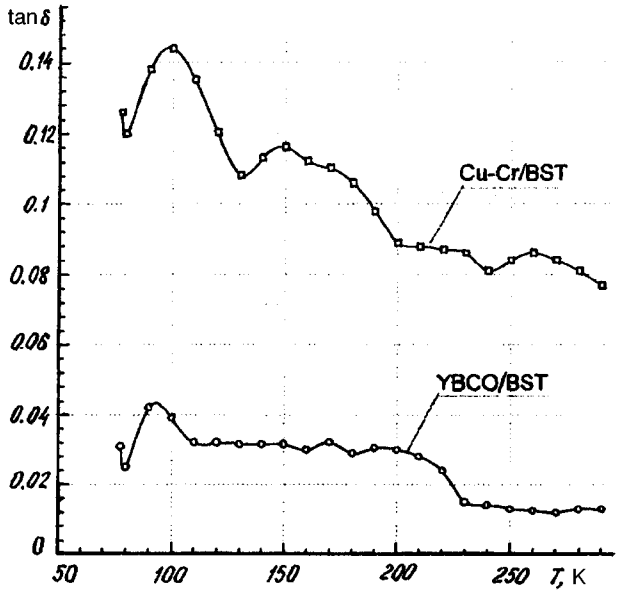

FIG. 3. Temperature dependences of the dielectric loss tangent for structures with Cu–Cr and YBCO electrodes.

hysteresis in the paraelectric and ferroelectric phases. For metal electrodes the dielectric hysteresis of structures with $Ba_{0.5}Sr_{0.5}TiO_3$ films in the paraelectric phase (Fig. 2, $T=300$ K) may be explained as for $SrTiO_3$ (Ref. 2): 1) by the formation of space charge at the metal/ferroelectric contact; if, as is usually the case, the work function of the metal (Φ_m) is lower than that of the ferroelectric (Φ_{fe}), a barrier is formed for holes;[6] 2) by injection of electrons from the metal electrodes. Capacitance-voltage characteristics without dielectric hysteresis were observed for single-crystal $SrTiO_3$ structures with YBCO electrodes at 4.2 K (where $\Phi_{YBCO}>\Phi_{fe}$ (Ref. 6)). For this ratio of work functions carrier injection from the electrodes is suppressed[7] and no dielectric hysteresis is observed. It may be postulated that this ratio of work functions is achieved for a YBCO/BST contact and no dielectric hysteresis is observed (Fig. 2, $T=300$ K).

When YBCO electrodes are used, the dielectric hysteresis of the structures in the ferroelectric phase is also smaller than that in the ferroelectric phase for structures with Cu–Cr electrodes (Fig. 2, $T=78$ K). This may be explained by the fact that the hysteresis in Cu–Cr/BST structures is caused not only by a ferroelectric transition but also by the formation and redistribution of space charge. The transition of YBCO to the superconducting phase most likely has no influence on the characteristics of the structures at 78 K, since the work function remains the same.[5,8] Our previous experiments using YBCO/STO structures (STO single crystal) have shown that no correlation is observed between the superconducting transition temperature and the existence of dielectric hysteresis.[6]

The reduction in the level of dielectric losses in YBCO/BST structures compared with those in Cu–Cr/BST structures may attributed to a change in the properties of the boundary layer of the BST film.

To sum up, the use of YBCO electrodes in planar structures consisting of $Ba_{0.5}Sr_{0.5}TiO_3$ thin films ensures that no dielectric hysteresis occurs in the paraelectric phase, while the dielectric nonlinearity is conserved and the level of dielectric losses reduced.

This work was carried out as part of Superconductivity Projects Nos. 94051 and 95014.

[1] B. M. Gol'tsman, A. I. Dedyk, V. V. Lemanov, L. T. Ter-Martirosyan, and S. F. Karmanenko, Fiz. Tverd. Tela (St. Petersburg) **38**, 2493 (1996) [Phys. Solid State **38**, 1368 (1996)].
[2] O. G. Vendik, A. I. Dedyk, R. V. Dmitrieva *et al.*, Fiz. Tverd. Tela (Leningrad) **26**, 684 (1984) [Sov. Phys. Solid State **26**, 412 (1984)].
[3] A. I. Dedyk, S. F. Karmanenko, and L. T. Ter-Martirosyan, *Abstracts of Papers presented at Conference on Electrical Relaxation in High-Resistivity Materials*, St. Petersburg, 1994, p. 1373.
[4] *Ferroelectrics in Microwave Engineering*, edited by O. G. Vendik [in Russian] (Moscow, 1979).
[5] M. Yu. Kupriyanov and K. K. Likharev, Usp. Fiz. Nauk **160**, 49 (1990) [Sov. Phys. Usp. **33**, 340 (1990)].
[6] A. L. Dedyk, N. W. Plotkina, and L. T. Ter-Martirosyan, Ferroelectrics **144**, 77 (1993).
[7] A. I. Dedyk, S. F. Karmanenko, M. N. Malyshev, and L. T. Ter-Martirosyan, Fiz. Tverd. Tela (St. Petersburg) **37**, 3470 (1995) [Phys. Solid State **37**, 1906 (1995)].
[8] S. I. Shkuratov, V. T. Mesyats, S. N. Ivanov *et al.*, Sverkhprovodimost' (KIAE) **3**, 1214 (1990) [Superconductivity **3**, 564 (1990)].

Translated by R. M. Durham

Characteristics of stimulated emission from an optically pumped GaN/AlGaN double heterostructure

M. V. Maksimov, A. V. Sakharov, V. V. Lundin, A. S. Usikov, B. V. Pushnyĭ, I. L. Krestnikov, N. N. Ledentsov, P. S. Kop'ev, Zh. I. Alferov, and V. P. Rozum

A. F. Ioffe Physicotechnical Institute, Russian Academy of Sciences. St. Petersburg; Scientific-Research Institute of Radiomaterials, Minsk

(Submitted April 15, 1997)
Pis'ma Zh. Tekh. Fiz. **23**, 53–59 (August 12, 1997)

The luminescence properties of a $GaN/Al_{0.1}Ga_{0.9}N$ double heterostructure grown by vapor-phase deposition from organometallic compounds are studied. When luminescence is observed from the end, the radiation intensity shows a sharply defined threshold dependence on the pump density. The threshold excitation density at $T=77$ K was ~ 40 kW/cm^2 and the wavelength of the stimulated emission was $\lambda=357$ nm. The long-wavelength shift of the emission line at high pump densities may be attributed to renormalization of the band gap caused by many-particle interactions in the electron–hole plasma. © *1997 American Institute of Physics.* [S1063-7850(97)01008-2]

Recent years have seen considerable progress in the development and investigation of InGaN–AlGaN light-emitting devices in the blue–green range. Lasing in an injection-pumped InGaN–AlGaN system was reported for the first time in Refs. 1 and 2.

Further progress towards shorter wavelengths, i.e., ultraviolet, may be achieved by using GaN–AlGaN and $Al_xGa_{1-x}N$–$Al_yGa_{1-y}N$ heterostructures. Lasing has been demonstrated by various authors in optically pumped epitaxial GaN layers and also in AlGaN/GaN double heterostructures.[3,4] The threshold excitation densities were 100 and 85 kW/cm^2 at room temperature for double-cleaved structures (50 kW/cm^2 at 77 K; Ref. 4). An investigation of stimulated emission and lasing processes with optical pumping is extremely important in order to assess the quality of the structure, its geometry and growth parameters, and also to study the lasing mechanisms.

In this article we investigate the structural and optical properties of an AlGaN–GaN double heterostructure grown by vapor-phase epitaxy from organometallic compounds. The structure was grown in a horizontal inductively heated reactor at a pressure of 200 mbar. The carrier gas was hydrogen, the source of group III elements was trimethylgallium and trimethylaluminum, and the nitrogen source was ammonia. A $(0001)\pm 30'$ oriented polished sapphire substrate was used. Before being inserted in the reactor, the substrate was degreased in organic solvents, etched with HF + HNO_3 (1:3), washed with water, and dried. The buffer layer was formed by GaN deposited at 510 °C. The fluxes of trimethylgallium, ammonia, and hydrogen were 45 μmol/min, 1.5 liter/min, and 4.5 liter/min, respectively. After the buffer layer had been annealed at 1000 °C in an ammonia atmosphere, an epitaxial layer of GaN began to be deposited at 1040 °C. The trimethylgallium, ammonia, and hydrogen fluxes were 36 μmol/min, 2.5 liter/min, and 4.5 liter/min, respectively. During growth of the AlGaN layers, a trimethylaluminum flux of 1.5 μmol/min was supplied to the reactor. The growth rate was 3 μm/h.

The structural quality of the sample was investigated by transmission electron spectroscopy. Bright-field images obtained for cross sections of the sample showed that dislocations of density exceeding 1.0×10^{10} cm^2 accumulate at the layer/substrate interface. The layers adjacent to the interface exhibit a block structure, where the boundaries of the blocks are defined by dislocations. The defect density decreases substantially with increasing proximity to the surface. The interfaces of the upper GaN and AlGaN layers are planar and the defect density at the upper interface is of the order of 5×10^7 cm^2.

Stimulated emission processes were investigated using a sample with one cleaved face, pumped by a pulsed nitrogen laser ($\lambda=337.1$ nm) with a pulse power of 1.5 kW. The laser beam was focused into a 5×0.3 mm spot by means of a cylindrical lens. The pump power was reduced by neutral filters. The photoluminescence spectra were recorded from the cleaved face of the sample. The radiation was detected by a cooled photomultiplier operated in the synchronous detec-

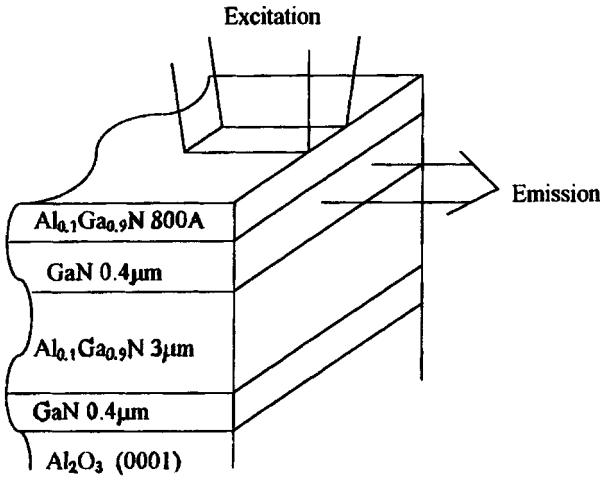

FIG. 1. Diagram of structure and experimental geometry.

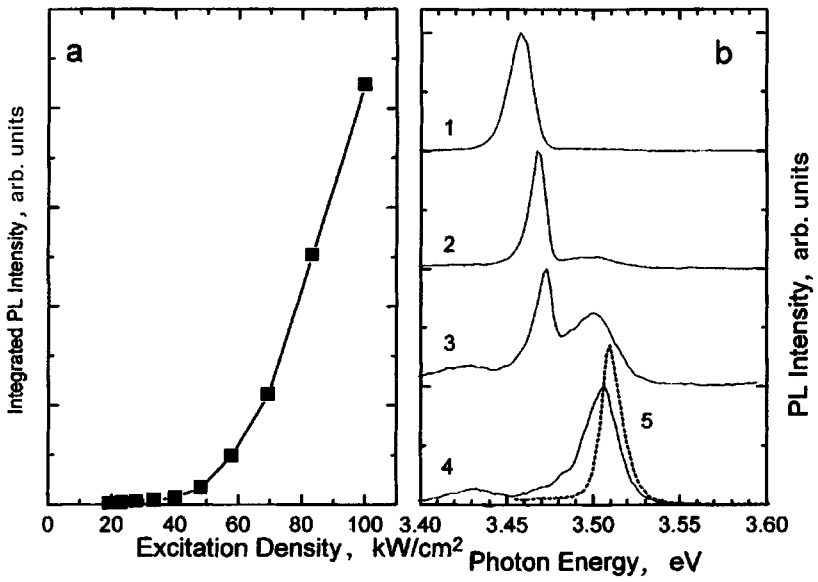

FIG. 2. a — Integrated intensity of luminescence from the end as a function of excitation density; b — spectra of luminescence from the end obtained at different excitation densities: *1* — 100 kW/cm^2, *2* — 58 kW/cm^2, *3* — 40 kW/cm^2, *4* — 19 kW/cm^2, and *5* — spectrum of photoluminescence from the surface (excitation density 1 W/cm^2).

tion mode. The experimental geometry and the structure are shown schematically in Fig. 1.

Luminescence spectra for various pump densities are shown in Fig. 2b, which also gives the spectrum of the photoluminescence from the surface of the sample excited by a He–Cd laser (1 W/cm^2). The slight difference between the spectra of the photoluminescence from the end and from the surface can be attributed to self-absorption as radiation is extracted from the end. It can be seen from Fig. 2b that at pump densities around 40 kW/cm^2 a narrow stimulated emission peak is observed at the long-wavelength wing of the spontaneous emission line. The integrated intensity of the photoluminescence from the end is plotted as a function of the pump power, $P(I)$, in Fig. 2a. The superlinear increase in intensity supports the observation of stimulated emission. An interesting result deduced from Fig. 2a is that the dependence of the integrated photoluminescence intensity on the pump density has a clearly defined kink. This effect is more usually associated with lasing than with stimulated emission and may be explained as follows. For the optical measurements the structure is cleaved into smaller pieces on the substrate side. This cleaving of the substrate in the epitaxial layer may produce cracks which may form well cleaved [0110] faces. Two neighboring cracks may form a cavity. Another possible explanation for this effect is that GaN films grown by organometallic chemical vapor deposition may exhibit domains having characteristic dimensions of 0.1–0.3 μm (Ref. 5). Thus these domain sizes are close to the wavelength of light in the crystal. The clearly defined threshold on the curve $P(I)$ may thus be caused by an effect similar to distributed feedback.

As far as we are aware, our threshold pump density (40 kW/cm^2) is comparable with the best results published for GaN/AlGaN double heterostructures at 77 K (50 kW/cm^2 (Ref. 4)) and is substantially lower than the threshold densities for GaN layers (500 kW/cm^2 (Ref. 6) at 10 K).

Figure 3 gives the full width at half-maximum and the peak position of the luminescence line (stimulated emission) as functions of the pump density. At pump densities above the threshold the photoluminescence line narrows abruptly and the position of its peak changes. With further increase in pump intensity, the line broadens slightly and begins to be shifted toward lower energies. The results of an approximation of the experimental data (Fig. 3, dashed curve) yield the

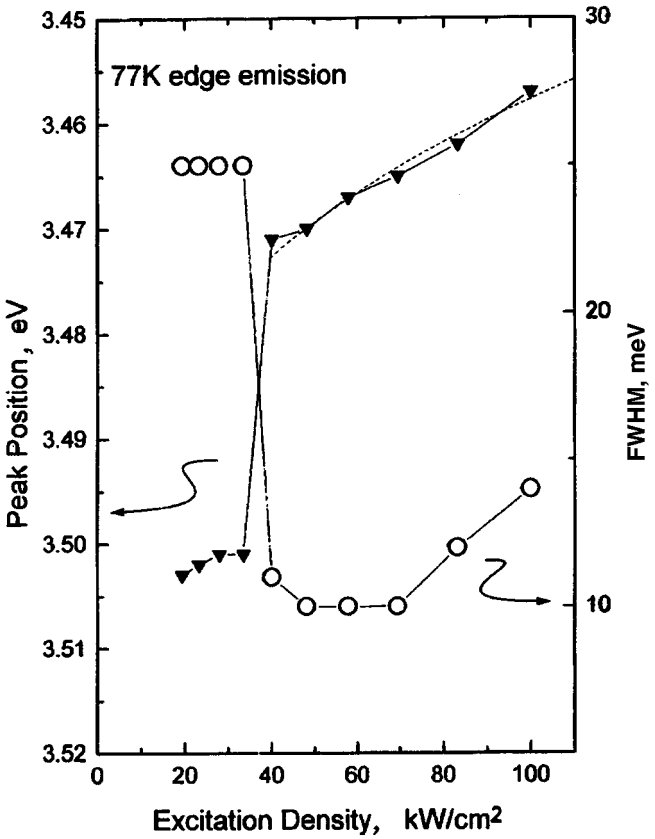

FIG. 3. Full width at half-maximum and peak position of luminescence line a functions of excitation density. The dashed curve gives the approximation using expressions (1) and (2).

following expression for the shift of the stimulated emission line as a function of the pump intensity:

$$E = E_g - 0.93 \times 10^{-8}(n^{1/3} + p^{1/3}), \quad (1)$$

where $n = p$ is the density of photoexcited carriers, which is related to the pump density W by:

$$n = \left(\frac{W\tau}{d}\right) \Big/ \left(\frac{hc}{\lambda}\right), \quad (2)$$

where d is the thickness of the GaN layer (0.4 μm), τ is the pulse length (5 ns), and $\lambda = 337.1$ nm.

Similar behavior was obtained for GaAs (Ref. 7) and was explained by invoking electron–electron and hole–hole interactions, which reduce the ground-state energy of the electron–hole plasma (i.e., decreases the band gap). Theoretical calculations[8] yield the following expression:

$$E = E_g - 1.6 \times 10^{-8}(n^{1/3} + p^{1/3}). \quad (3)$$

The good agreement between the theoretical calculations and the experimental data suggests that the stimulated emission involves band–band transitions while electron–electron and hole–hole exchange interactions are responsible for the long-wavelength shift of the stimulated emission line.

CONCLUSIONS

Stimulated emission has been demonstrated in an optically pumped AlGaN/GaN double heterostructure. The threshold pump density at 77 K was 40 kW/cm^2 which is comparable with the best results obtained for similar samples at this temperature.

[1] S. Nakamura, in *Proceedings of the International Symposium on Blue Laser and Light Emitting Diodes*, Chiba University, Japan, 1996.
[2] I. Akasaki, Jpn. J. Appl. Phys. Part 2 **34**, L1517 (1995).
[3] H. Amano, N. Watanabe, N. Koide, and I. Akasaki, Jpn. J. Appl. Phys. Part 2, **32**, L1000 (1993).
[4] R. L. Aggarwal, P. A. Maki, R. J. Molnar, Z. L. Liau, and I. Melngails, J. Appl. Phys. **79**, 2148 (1996).
[5] F. A. Ponce, D. P. Bour, W. Götz, and P. J. Wright, Appl. Phys. Lett. **68**, 57 (1996).
[6] X. H. Yang, T. J. Schmidt, W. Shan, J. J. Song, and B. Goldenberg, Appl. Phys. Lett. **66**, 1 (1995).
[7] H. C. Casey and F. Stern Jr., J. Appl. Phys. **47**, 631 (1976).
[8] P. A. Wolff, Phys. Rev. **126**, 405 (1962).

Translated by R. M. Durham

Phase conjugation in four-wave mixing of cw radiation under conditions of strong self-interaction

V. I. Ivanov, A. I. Illarionov, and I. A. Korosteleva

Far-East State Academy of Transportation, Khabarovsk
(Submitted November 10, 1996)
Pis'ma Zh. Tekh. Fiz. **23**, 60–63 (August 12, 1997)

An experimental investigation is made of the influence of strong self-interaction of the reference waves on phase conjugation in four-wave mixing of cw radiation in a medium with a thermal nonlinearity. It is shown that the thermal lens formed by the Gaussian reference beams reduces the nonlinear reflection coefficient appreciably (several-fold) and causes a deterioration in the phase conjugation quality. © *1997 American Institute of Physics.* [S1063-7850(97)01108-7]

Thermally induced nonlinearities are responsible for highly efficient nonlinear reflection in four-wave mixing of low-intensity radiation. However, in four-wave mixing of long pulses or cw radiation phase conjugation is accompanied by significant side effects which restrict the potential for optimizing the parameters of the phase-conjugating mirror. These effects include, for example, thermally induced convection and also the formation of a thermal lens induced by the nonuniform transverse distribution of the beam intensity. Self-interaction of the reference waves gives rise to significant distortions of the phase-conjugate wavefront since conjugate pump waves are required in a phase conjugation–four-wave mixing system.

The influence of a thermal lens on phase conjugation in four-wave mixing has been investigated by various authors (for example, Refs. 1 and 2) with the most detailed study being reported in Ref. 3, but these results were obtained under conditions of weak self-interaction whose description is confined to the paraxial approximation. The main aim of our experimental investigations described below was to examine strong self-defocusing of the radiation, where the aberrations of the thermal lens become appreciable.[4] In this case, the self-interaction of a Gaussian beam can only be analyzed theoretically in the wave optics approximation and numerical methods must be applied.[5]

In these experiments we investigated the transverse distribution of the laser beam intensity ($\lambda = 10.6\ \mu$m) beyond an acetone-containing cell of thickness $L = 230\ \mu$m as a function of the distance z before the cell. A detector with a 0.2×0.5 mm diaphragm was moved horizontally in the plane perpendicular to the beam to record the transverse intensity distribution. The power of the beam incident on the cell was 7.1 W. Transverse intensity profiles of the beam are shown in Fig. 1. In Fig. 1a the scale of the ordinate is reduced by a factor of ten compared with that in Fig. 1b. It can be seen that the after passage through the cell, the beam is converted into a ring whose diameter is between two and three times the characteristic size of the incident Gaussian beam.

Four-wave mixing experiments were carried out using a system where a second reference wave was formed by reflection from a retroreflecting mirror positioned beyond the cell containing the nonlinear medium. Figure 2a gives the nonlinear reflection coefficient R as a function of the distance z between the cell and the mirror forming the second reference wave. The transmission of the cell was close to the optimum (the absorption coefficient of the medium is $\alpha \sim L^{-1}$). The decrease in the reflection coefficient R with increasing z is caused by two factors.[3] For large z ($z > \omega/\sin\theta$), where ω is the beam radius in the plane of the cell), the behavior of $R(z)$ is caused by the action of the thermal lens. Since the local nonlinear reflection coefficient is proportional to the product of the reference wave intensities, a drop in the intensity of the second reference wave in the plane of the cell leads to a corresponding decrease in R as given by $R(z) \sim R_0(1 + zf^{-1})^{-2}$ (where R_0 is the nonlinear reflection coefficient in the absence of self-interaction and f is the focal length of the thermal lens). This conclusion is supported by the fact that the characteristic time for the decrease in the reflection coefficient R is the same as the time taken for formation of the thermal lens (Fig. 2b). The reflection coefficient reaches a maximum after 20 ms, which is determined by the period of the grating, and then over a period of a few minutes comes to a steady-state value approximately a third of the maximum for a few second. The abrupt increase in R with decreasing z (in the range $z < \omega/\sin\theta$) is caused by the additional contribution made by the grating recorded by the

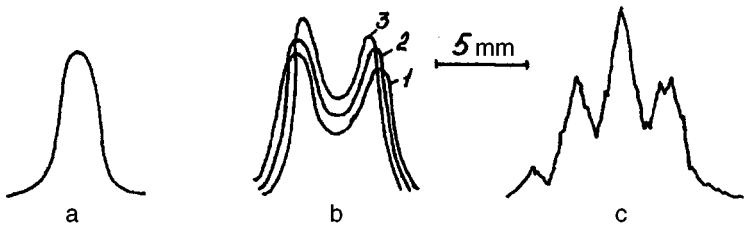

FIG. 1. Transverse intensity distribution: a — Gaussian beam before cell, b — reference beam after passage through liquid cell at different distances z from the cell, cm: *1* — 22, *2* — 30, *3* — 39; c — phase-conjugate waves — channel.

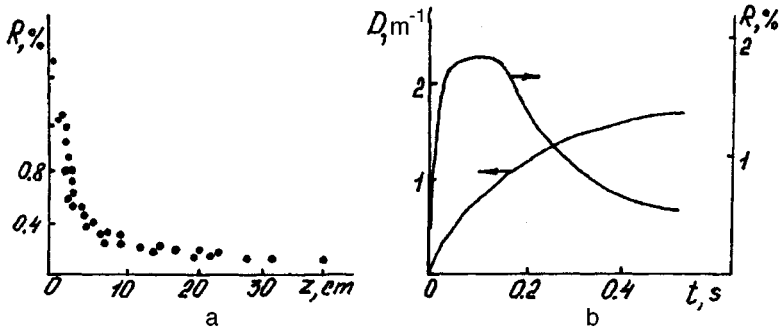

FIG. 2. Nonlinear reflection coefficient R versus: a — distance z between cell and mirror used to form second reference wave, b — time measured from the time of initiation of the radiation; D is the effective power of the thermally induced lens (experimental).

signal and reference waves reflected by the retroreflecting mirror. For $z=0$, the additional grating can increase the nonlinear reflection coefficient by a factor of four.[3] This contribution disappears when the reflected signal wave does not overlap the reference wave.

The transverse distribution of the wave intensity in the phase-conjugated wavefront channel is shown in Fig. 1c ($z=22$ cm). It can be seen that the phase-conjugated wavefront is a beam with a non-Gaussian structure and is much broader than the signal beam. Since the distortions are mainly caused by the thermal lens, in order to obtain high-quality phase conjugation the influence of this lens must somehow be reduced, for example, by focusing the signal wave using independent pump waves.

Steady-state phase conjugation was also observed experimentally. The maximum recording time was around 10 min, which is many times longer than the time taken to form the refractive index grating in the liquid, the lens formation time, and the ''convective'' time. The steady-state phase conjugation time was limited by the instability of the laser power and by boiling of the liquid.

These results can be used to assess the influence of self-defocusing on phase conjugation in four-wave mixing. First, in addition to the phase distortions induced by the thermal lens and the increasing divergence of the reflected wave,[3] the evolution of the transverse intensity distribution of the reference waves reduces the region of overlap of the interacting waves and thus decreases the reflection coefficient. Second, the experiments have demonstrated that strong defocusing of the reference waves causes a significant deterioration in the conjugation quality. Thus the action of the thermal lens must be restricted to obtain high-quality phase conjugation in four-wave mixing of quasi-cw radiation. Note that phase correction methods are only suitable for weak defocusing ($f \gg L$), because in the opposite case, the phase distortions are converted into amplitude distortions over the thickness of the nonlinear medium.

[1] V. B. Gerasimov, A. V. Golyanov, M. N. Goryacheva *et al.*, Kvantovaya Elektron. (Moscow) **13**, 338 (1986) [Sov. J. Quantum Electron. **16**, 223 (1986)].
[2] O. L. Antipov, Kvantovaya Elektron. (Moscow) **14**, 728 (1987) [Sov. J. Quantum Electron. **17**, 458 (1987)].
[3] O. L. Antipov, A. A. Betin, E. A. Zhukov *et al.*, Preprint No. 193 [in Russian], Institute of Applied Physics, Academy of Sciences of the USSR, Gorkiĭ (1988).
[4] D. C. Smith, Proc. IEEE **65**, 1679 (1977).
[5] I. Sh. Beluga, B. S. Vinevich, and L. L. Kolosovskaya, Opt. Spektrosk. **50**, 531 (1981) [Opt. Spectrosc. (USSR) **50**, 292 (1981)].

Translated by R. M. Durham

Thermoelectric elements based on compounds of silicon and transition metals

M. I. Fedorov, V. K. Zaĭtsev, F. Yu. Solomkin, and M. V. Vedernikov

A. F. Ioffe Physicotechnical Institute, Russian Academy of Sciences, St. Petersburg
(Submitted April 15, 1997)
Pis'ma Zh. Tekh. Fiz. **23**, 64–69 (August 12, 1997)

Semiconducting compounds based on silicides of 3d transition metals ($MnSi_{1.75}$ and CoSi) are promising thermoelectric materials for mass-produced thermoelectric generators. Their practical use has been delayed so far by the lack of reliable switching. Electrochemical surface treatment technology and metal deposition were used to obtain thermal-cycling-resistant, switching and antidiffusion metal coatings (Ni, Co, Fe, Cr) with an electrical resistivity up to $10^{-6}\ \Omega\cdot\mathrm{cm}^2$ in the metal–semiconductor region. This technology was applied to develop a series of thermoelements and thermoelectric generators having wide-ranging applications.
 [S1063-7850(97)01208-1]

In addition to high efficiency, crucial requirements for many important practical applications of thermoelectric generators include cheap starting materials, capacity to operate in air and in vacuum without any protection, high mechanical strength, and environmental friendliness. All these requirements can be fully met by compounds of silicon with transition metals.

Among the various silicide-based thermoelectric materials, the most promising are the high-silicon manganese silicide, $MnSi_{1.71-1.75}$ (HSM), solid solutions based on Mn_2Si, and cobalt monosilicide.[1] The efficiency of these compounds is comparable with that of conventional chalcogenide thermoelectric materials, but their physicochemical, mechanical, and cost parameters are considerably superior.[2] These materials are particularly promising for the mass production of thermoelectric generators, including generators for the cathodic protection of gas and oil pipelines from corrosion, thermoelectric generators designed to utilize waste heat, and also everyday standalone thermoelectric power supplies. Thermoelements and thermoelectric modules utilizing HSM as the *p*-branch material and cobalt or nickel monosilicide as the *n*-branch have now been developed at the Laboratory of Thermoelement Physics at the A. F. Ioffe Physicotechnical Institute of the Russian Academy of Sciences.

Until recently, the widespread use of these thermoelectric materials was delayed by the lack of reliable switching. The contacts need to retain their electrical parameters under repeated thermal cycling and should possess high mechanical strength. In addition, the high-temperature operating conditions impose additional constraints on the choice of switching materials and their fabrication technology. The metals used as contacts and the semiconductor material should have similar coefficients of linear expansion. It should also be borne in mind that metal may diffuse into the semiconductor, which frequently causes degradation of the devices. This diffusion may be reduced by incorporating intermediate antidiffusion layers.

The present authors have suggested using diffusion welding in vacuum for this purpose.[3] The bond is made by interdiffusion of the branch materials and switching elements at a temperature considerably higher than the operating temperature. At the lower operating temperature the diffusion rate is reduced by several orders of magnitude and the contacts may retain their properties over the entire operating life. The most reliable bonds are made by first depositing the switching element material onto the surfaces of the thermoelement branches.

The most suitable switching material for HSM and CoSi is nickel. Like cobalt monosilicide, it may also serve as a second (passive) branch for HSM-based thermoelectric generators.[4] Nickel can switch the generator branches up to 600 °C. At high temperatures it readily diffuses into HSM (Ref. 5) and may provide a reliable junction. However, the high coefficient of nickel diffusion into HSM may cause an excessively thick transition layer to form because of contact alloying. This alloying usually increases the resistance of the transition layer,[6] which reduces the efficiency of the thermoelement. Thus antidiffusion layers must be incorporated at the high-temperature junctions of the generators when nickel switching is used. These antidiffusion layers may be chromium[7] or iron.

Various methods of applying metal coatings are now used in semiconductor instrument manufacture. The most commonly used are vacuum deposition, compressing, and chemical and electrochemical deposition of the metal.

Electrochemical growth of metal coatings is an advanced method which combines preliminary treatment of the semiconductor surface (etching) and deposition of the metal coating in a single operation. This procedure reduces the thickness of the transition layer and therefore lowers the resistance of the metal–semiconductor interface. Unlike other methods, a wide range of materials can be used (directionally crystallized single crystals, textured and fused samples) and thick (up to 200 μm) metal coatings suitable for thermal diffusion welding with external current supplies can be grown rapidly. In order to obtain the highest-quality layers, the electrolyte must combine the properties of a polishing etchant with the correct composition for deposition of the metal layers.

The electrolytes were prepared by a procedure developed by the authors, where the base composition of the electrolyte is determined according to its absorption of light at a given wavelength. The composition of all these electrolytes is based on a water-soluble transition-metal salt and hydro-

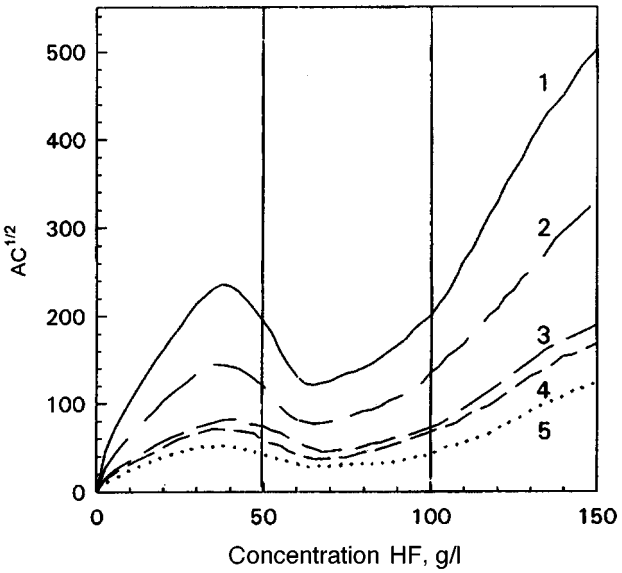

FIG. 1. Dependence of $AC^{1/2}$ on the hydrofluoric acid concentration for various solutions of transition metal sulfates: *1* — $FeSO_4$ (200 g/liter), *2* — $NiSO_4$ (400 g/liter), *3* — $NiSO_4$ (200 g/liter), *4* — $CoSO_4$ (300 g/liter), and *5* — $CoSO_4$ (200 g/liter).

luoric acid. The relation between the optical properties of the solution and its HF content was analyzed by plotting the ratio of the light transmission of an aqueous solution of HF of a given concentration to the transmission of a salt solution having the same concentration of hydrofluoric acid (the relative absorption A) at a given wavelength ($\lambda = 0.86$ μm) as a function of the HF concentration C: $A = f(C)$. It was shown experimentally that for HF concentrations of 50–100 ml/liter the relative absorption has a minimum for all the solutions. By analyzing these curves, plotted in the coordinates $AC^{0.5} = f(C)$ (see Fig. 1), and comparing them with the properties of the layers, we were able to identify a criterion for the applicability and efficacy of these compositions. The solutions can be used for concentrations near the relative absorption minimum if $AC^{1/2}$ is less than 1.5–1.6 times this minimum value.

This range of HF concentrations is common to all these solutions and may be used as the ''initial'' composition to develop electrolytes which combine the properties of polishing etchant and composition suitable for the deposition of metal layers (Fe, Ni, Co, Cr) on transition-metal silicides, silicon, and silicon carbide.

The resistivity of the metal–semiconductor transition region was measured by a microprobe method and did not exceed 10^{-6} $\Omega \cdot \mathrm{cm}^2$. Since these contacts are Ohmic, they can be used not only to develop and fabricate thermoelectric generators but also to study the physical properties of thermoelectric materials, During thermal cycling at temperatures of 300–1000 K the coatings withstood 100 cycles without any significant change in properties.

TABLE I. Total thermoelectric power versus hot junction temperature.

Hot junction temperature, K	Total thermoelectric power, V
400	0.1
600	0.25
700	0.35
800	0.45
850	0.55
920	0.6

In mechanical tearing tests the coatings came off together with the semiconductor material.

These thermoelectric materials and methods of preparing switching and antidiffusion layers were used to develop a series of thermoelements and thermoelectric generators for a wide range of applications, based on a thermoelectric module comprising a bank of ten elements. The p-branch was made of HSM and the n-branch of nickel. The optimum ratio of HSM and nickel cross sections is 50 and thus the n-branch may be made of nickel strip which also functions as a switching element. A chromium antidiffusion layer and a nickel switching layer were deposited on the contact areas of the p-branch to ensure a low-resistance, reliable electrical connection. All the elements in the bank were connected by diffusion welding in vacuum in a single process. The total thermoelectric power was measured as a function of the hot junction temperature for the modules under near-operating conditions (see Table I). All the modules had identical properties. Tests were also carried out on a prototype of the thermoelectric generator consisting of five series-connected modules. This generator delivered rated powers and working voltages of 1 W and 1.5 V, respectively.

To sum up, it has been shown that in principle general-purpose thermoelectric generators utilizing transition metal silicides can be produced commercially.

[1] V. K. Zaĭtsev and M. I. Fedorov, Fiz. Tekh. Poluprovodn. **29**, 946 (1995) [Semiconductors **29**, 490 (1995)].
[2] M. I. Fedorov, E. A. Gurieva, L. V. Prokof'eva, and V. K. Zaitsev, in *Proceedings of the 14th International Conference on Thermoelectrics*, St. Petersburg, 1995, pp. 254–258.
[3] M. I. Fedorov, A. E. Engalychev, V. K. Zaitsev, A. E. Kaliazin, and F. Yu. Solomkin, in *Proceedings of the 13th International Conference on Thermoelectric Energy Conversion*, Kansas City, 1994, pp. 324–327.
[4] M. I. Fedorov and V. K. Zaitsev, *Semimetals as Materials for Thermoelectric Generators*, in *CRC Handbook of Thermoelectrics*, edited by D. M. Rowe (CRC Press, New York, 1995), pp. 299–309.
[5] L. I. Petrova, L. D. Dudkin, and V. S. Khlomov, Neorg. Mater. **31**, 1216 (1995).
[6] I. A. Drabkin, *Thermoelectrics and Their Application* (St. Petersburg, 1997), pp. 132–135.
[7] L. I. Petrova, L. D. Dudkin, V. S. Khlomov, M. I. Fedorov, V. K. Zaĭtsev, and F. Yu. Solomkin, *Thermoelectrics and Their Application* (St. Petersburg, 1997), pp. 102–105.

Translated by R. M. Durham

Modification of the phase transition in cesium niobate under gamma irradiation

V. N. Belomestnykh and A. P. Mamontov

Tomsk Polytechnic University
(Submitted March 28, 1997)
Pis'ma Zh. Tekh. Fiz. **23**, 70–74 (August 12, 1997)

Ultrasonic techniques are used to study the phase behavior of cesium niobate under gamma irradiation. It is shown that the irradiation shifts the anomalies of the internal friction and velocity of sound toward lower temperatures as a result of structural ordering of cesium niobate crystals. © *1997 American Institute of Physics.* [S1063-7850(97)01308-6]

Cesium nitrate, $CsNO_3$, is an excellent material for studying radiation-stimulated processes in polymorphic crystals.[1–3] It has been established that the crystal structure of this compound undergoes high-temperature changes under gamma irradiation. The critical dose of ionizing radiation at which a transition takes place from the trigonal (pseudohexagonal) to the cubic modification is determined by the crystal growth conditions and depends on the concentration of structural defects. On exposure to high gamma radiation doses, the Curie point is shifted toward high temperatures as a result of the incorporation of radiation defects.[4]

It is interesting to study the phase behavior of $CsNO_3$ by ultrasonic techniques based on measuring the propagation characteristics of elastic waves. We present results of such studies and we show how low gamma radiation doses influence the phase behavior of $CsNO_3$ crystals.

The spectra of acoustic parameters (the internal friction Q^{-1} and the propagation velocity v of the longitudinal ultrasonic waves) were studied in unirradiated and irradiated $CsNO_3$ crystals in the temperature range 300–450 K, which includes the structural phase transition point $T_c \approx 427$ K (Ref. 5). The changes in Q^{-1} and v were determined using a composite piezoelectric vibrator at a frequency of $\sim 10^5$ Hz for which the relative amplitude of the bending modes was $\sim 10^{-7}$. The relative errors for the measured values were $\Delta v/v = 2\times 10^{-5}$ and $\Delta Q^{-1}/Q^{-1} = 5\times 10^{-2}$. The crystal temperature varied at a rate of ~ 0.1 K/min and was controlled to within 0.1 K.

Cesium nitrate polycrystals were prepared by hot pressing high-purity powder into pellets in vacuum. The density of the polycrystalline samples was 3.5 g/cm^3, which is close to the tabulated density of $CsNO_3$ II (Ref. 6). The samples were 2×2 mm rods whose length was selected to contain a half-wavelength of the ultrasound at the measurement frequency. All the samples underwent isothermal annealing at $T_{ann} \approx 400$ K and were cooled at a rate of 3 K/h. The samples were irradiated by gamma radiation from a ^{60}Co source using an ''Issledovatel'' gamma irradiation facility and were exposed to a dose of 10^3 R. The temperature of the samples during irradiation did not exceed 300 K.

The results of the measurements for Q^{-1} and v are plotted in Figs. 1 and 2, respectively, for unirradiated (curves *1*) and irradiated samples (curves *2*). It can be seen that the temperature spectra of the acoustic parameters for the unirradiated and irradiated samples show substantial differences. For the unirradiated samples, anomalies in the attenuation and velocity of the ultrasonic waves (a finite peak for the function $Q^{-1}(T)$ and a continuous negative step for the function $V(T)$) are recorded near $T = T_c$. In accordance with the classification given in Ref. 7, the anomalies of these parameters indicate that the phase transition in $CsNO_3$ should be considered to be isothermal to a considerable extent. These results also indicate an enhanced degree of orientational melting of the anion sublattice accompanying the $CsNO_3$ II $\rightarrow$ $CsNO_3$ I transition, which is typical of pseudoplastic materials. This last factor supports the model of well-defined dislocation preference which promotes a change in the concentration of unit vacancies in irradiated $CsNO_3$ crystals and helps to attain the critical value required for radiation-stimulated rearrangement of the crystal structure.

Gamma irradiation shifts the anomalies of $Q^{-1}(T)$ and $v(T)$ toward lower temperatures ($T = 373$ K), modifies the form of these anomalies (reduces the internal friction maximum and the sound velocity jump), induces a larger spread over temperature, and reduces the absolute value of the velocity of sound in the $CsNO_3$ II phase and increases it in the $CsNO_3$ I phase. All these factors indicate that in irradiated $CsNO_3$ samples, the acoustic anomalies lose the features characteristic of typical continuous phase transitions in solids and acquire the characteristic features inherent in the preferential removal of point defects.

The observed modification of the temperature spectra of the acoustic parameters of gamma-irradiated $CsNO_3$ crystal can be explained as follows. The $CsNO_3$ crystals are in initial states far from thermodynamic equilibrium. The estab-

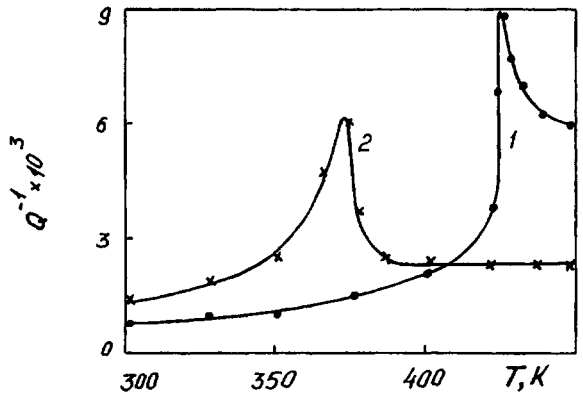

FIG. 1. Internal friction versus temperature of unirradiated (curve *1*) and gamma-irradiated cesium nitrate (curve *2*).

 1063-7850/97/080604-02$10.00

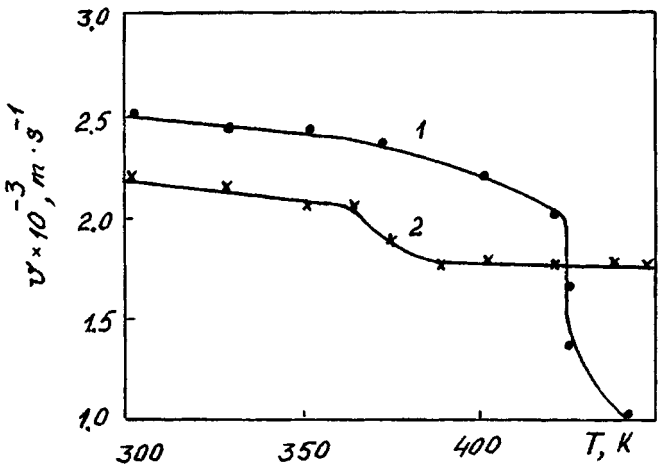

FIG. 2. Propagation velocity of longitudinal ultrasonic waves versus temperature of unirradiated (curve *1*) and gamma-irradiated cesium nitrate (curve *2*).

lishment of equilibrium is impeded by the energy parameters of the defect and impurity rearrangements. Exposure of $CsNO_3$ crystals to low gamma radiation doses can substantially reduce their initial degree of nonequilibrium. Exposure of $CsNO_3$ crystals to gamma radiation doses at which ionization processes predominate, promotes annihilation of interstitial atoms with genetically linked vacancies. This annihilation process produces θ-bursts, capable of inducing and sustaining self-limiting reactions involving the removal of point defects in the crystal. An increase in temperature in the defect annihilation zone removes stresses with a release of the energy stored in the crystal. This produces states with a lower entropy than the initial entropy, characterizing the ordering of the crystal structure. These highly unlikely states from the equilibrium thermodynamics point of view may exist indefinitely for a defect density above a certain critical value. These states are determined by the barrier height and the annihilation energy, and by the effective thermal conductivity and the transition frequency. The processes then become self-sustaining and lead to qualitative changes in the organization of the $CsNO_3$ crystals as a result of a transition from one quasistable state to another, which is observed as a shift of the observed anomalies in the $CsNO_3$ crystals exposed to low gamma radiation doses.

[1] E. V. Kolontsova, A. V. Korneev, and V. P. Lutsenko, Kristallografiya **23**, 656 (1978) [Sov. Phys. Crystallogr. **23**, 367 (1978)].
[2] E. V. Kolontsova, S. V. Red'ko, and V. P. Lutsenko, Dokl. Akad. Nauk SSSR **298**, 859 (1988) [Sov. Phys. Dokl. **33**, 144 (1988)].
[3] B. A. Maksimov, L. A. Muradyan *et al.*, Dokl. Akad. Nauk SSSR **298**, 1390 (1988) [Sov. Phys. Dokl. **33**, 92 (1988)].
[4] N. Mukhtarov and N. K. Yushin, Pis'ma Zh. Tekh. Fiz. **21**(21), 39 (1995) [Tech. Phys. Lett. **21** 879 (1995)].
[5] N. G. Parsonage and L. A. Stavely, *Disorder in Crystals* (Oxford University Press, Oxford, 1979) [Russ. transl., Mir, Moscow, 1982].
[6] *Handbook of Chemistry* [in Russian], Vol. 2 (Khimiya, Leningrad, 1971)
[7] V. N. Belomestnykh, *Abstracts of papers presented at the 11th Conference on Kinetics and Mechanism of Chemical Reactions in Solids*, Minsk-Chernogolovka, 1992 [in Russian], IKhFCh, p. 279.

Translated by R. M. Durham

Dynamics of surface damage in dry friction

Yu. A. Fadin

Institute of Problems in Mechanical Engineering, Russian Academy of Sciences, St. Petersburg
(Submitted November 15, 1996; resubmitted March 13, 1997)
Pis'ma Zh. Tekh. Fiz. **23**, 75–78 (August 12, 1997)

A new approach is proposed to describe friction, based on the dynamic interaction of surface roughnesses. An analysis is made of two types of interaction, one causing only deformation of the roughnesses and the other ultimately leading to the appearance of damage particles. [S1063-7850(97)01408-0]

The real surfaces of solids exhibit roughness. In dry friction the actual contact between the friction surfaces is discrete and the total area of contact is small. For instance, according to data given in Ref. 1, this area is 0.1–0.01% of the nominal area of the contact surface. High mechanical stresses are created in these roughness contact zones (which are usually called contact spots). We shall estimate these stresses for a single contact spot, for which the roughness contact is replaced by a Hertz contact (the contact between a sphere and an elastic half-space under the action of a static force P). Then, according to Hunt,[2] the maximum tangential stress $\tau_{\max}=0.465P/\pi r^2$ is created at the depth $h_{\max}=0.49r$, where r is the radius of the contact spot. The range of variation in the diameters of the contact spots for metals is 3–40 μm (Ref. 3). The maximum tangential stresses will be generated at a depth between 1.5 and 20 μm. For a solid at nominal pressures of 2–4 MPa, if the real area of contact does not exceed 0.1% of the nominal area, then $\tau_{\max}$ in the vicinity of a single spot reaches the enormous pressure of 1–2 GPa, and this is neglecting the friction force, which increases the tangential stresses still further. Estimated values of the tangential stress are thus quite suitable for most metals and are sufficient for the evolution of shear processes in the surface layers, following by cracking. The appearance of damage particles has been observed experimentally at the initial stages of friction, which suggests intensive subsurface cracking.[4] Contact between single roughness points exists for a finite time, which is determined by the sliding velocity. The dynamics of the contact spots creates a field of mechanical stresses, fluctuating over depth and time, in which surface cracks form and propagate. Thus the friction between solids can be treated as a surface dynamical process involving the simultaneous formation and breakup of numerous contact spots.

In this article, particular attention is devoted to the temporal aspect of the relation between the evolution of the dynamic system formed by the contact spots and the friction-induced surface damage process.

The roughness points have different heights and thus may interact differently in the formation of contact spots (Fig. 1). The present analysis is confined to a dynamical system consisting only of two types of elements. The first are the contact spots whose formation is accompanied by elastic or plastic deformation of the roughness points. As these contact spots break down, only the shape of their component roughness points changes. The other type of elements are contact spots which have appeared as a result of strong roughness interaction, where a microbinding zone forms between these roughness points. The breakdown of these contact spots ultimately leads to the appearance of damage particles. The behavioral dynamics of the proposed two-element system may be described mathematically using the ''predator–prey'' formalism, which is one of the simplest methods of describing the behavior of nonlinear systems (Lotka–Volterra model[5]). Let us assume that n is the number of contact spots at which the roughness points only undergo deformation and m are the contact spots which form microbinding zones followed by the formation of damage particles. We shall then call these particles contact-spot debris.

The changes in the number of the elements of the system with time are described by the nonlinear differential equations

$$\frac{dn}{dt}=\alpha n-\gamma nm, \quad \frac{dm}{dt}=-\beta m+\delta nm, \tag{1}$$

where γ and δ are constants characterizing an increase in elements n and m, respectively, and γ and β are constants characterizing a decrease in those parameters. The solutions of this system of nonlinear equations are periodic, phase-shifted, have a complicated form, and have been published in Ref. 5. The expression for the period T has the form

$$T=\frac{2\pi}{\sqrt{\gamma\beta}} \tag{2}$$

and depends only on the constants α and β of the elements of the system. Two conclusions can be drawn from the periodicity of the solutions of Eq. (1).

1. The periodic change in the number of spots producing debris implies that in dry friction, a finite volume of material is removed from the material over the time T and thus the damage to the surface (wear) takes place layer by layer and periodically.

2. The periodic change in the number of contact spots implies that during the friction process, the roughness of the contact surface is reproduced from one layer to another.

The constants α and β can be determined experimentally, for example by using acoustic emission. In the present study, it was observed that all the acoustic emission signals recorded for the dry friction of metals can be divided into two types, having durations which differ by one or two orders of magnitude (Fig. 2). In the time intervals containing

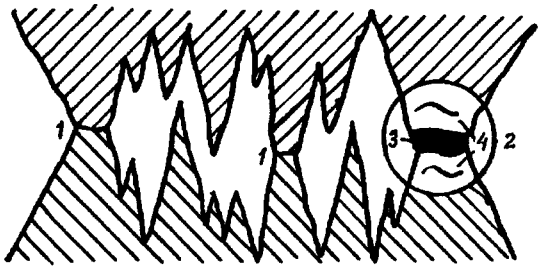

FIG. 1. Diagram of contact between rough surfaces: *1* — contact between roughness points accompanied by their deformation, *2* — contact zone with strong roughness interaction, *3* — microbinding zone, and *4* — surface cracks formed by breakdown of the contact.

the long acoustic emission signals, debris is observed, whereas in the time intervals containing only short signals, it is not. Thus the short acoustic emission signals may be attributed to deformation phenomena caused by impact between roughness points, while the long signals are associated with the appearance of debris. The appearance of the debris is associated with the loss of type m contact spots, i.e., with the constant β. The rates of generation of the two types of acoustic emission signals may be used as the constants in formula (2). For example, for aluminum at a pressure of 3 MPa and a velocity of 0.6 m/s, α is $\sim 5\ s^{-1}$ and $\beta \sim 0.01\ s^{-1}$ which gives $T \sim 28$ s, which is comparable with the average experimental value of the period of the layer damage obtained from the time dependence of the friction coefficients, ~ 40 s (Ref. 6).

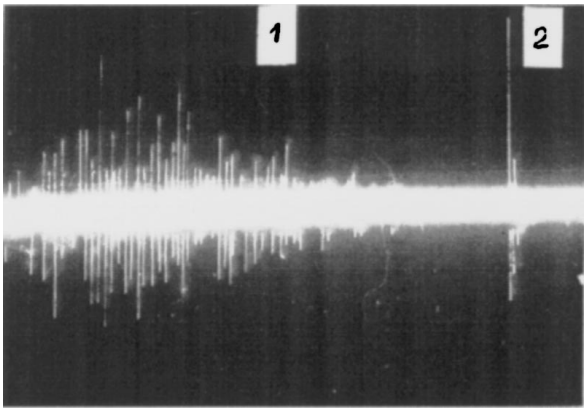

FIG. 2. Oscilloscope traces of acoustic emission signals for dry friction between aluminum and steel: *1* — ''long'' signal corresponding to the appearance of surface debris, *2* — ''short'' signal corresponding to impact of surface roughness points.

[1] F. P. Bowden and D. Tabor, *The Friction and Lubrication of Solids*, Part I (Clarendon Press, Oxford, 1950)
[2] E. B. Hunt, J. Appl. Phys. **26**, 850 (1955).
[3] N. B. Demkin, *Contact Between Rough Surfaces* [in Russian] (Nauka, Moscow, 1970).
[4] Yu. A. Fadin, A. M. Leksovskiĭ, B. M. Ginzburg, and V. P. Bulatov, Pis'ma Zh. Tekh. Fiz. **19**(5), 10 (1993) [Tech. Phys. Lett. **19**, 136 (1993)].
[5] V. Volterra, *Leçons sur la Théorie de la Lutte pour la Vie* (Gauthier-Villars, Paris, 1931) [Russ. transl., Nauka, Moscow, 1976].
[6] V. P. Bulatov, O. I. Polevaya, E. B. Sedakova, and Yu. A. Fadin, Pis'ma Zh. Tekh. Fiz. **22**(19), 1 (1996) [Tech. Phys. Lett. **22**, 777 (1996)].

Translated by R. M. Durham

Dependence of the empirical model parameters of the surface resistance of a high-temperature superconducting film on the parameters of the technological process

I. B. Vendik, E. K. Gol'man, S. V. Razumov, A. A. Svishchev, and A. V. Tumarkin

St. Petersburg State Electrical Engineering University
(Submitted April 4, 1997)
Pis'ma Zh. Tekh. Fiz. **23**, 79–84 (August 12, 1997)

The dependence of the surface resistance on the substrate heater temperature has been investigated for the purpose of optimizing the conditions for preparing $YBa_2Cu_3O_{7-\delta}$ films. It is shown that the resistance R_{sur} is highly sensitive to the accuracy of maintaining the substrate holder temperature to minimize the surface resistance of the films and maximize the parameter γ, which determines the temperature-dependent curves $\sigma(t)$ and $\lambda_L(t)$.
 [S1063-7850(97)01508-5]

The surface resistance R_{sur} of a high-temperature superconductor measured in the microwave range (1–90 GHz) is an objective integral criterion to determine the suitability of films for applications in microelectronics. By minimizing the surface resistance during development of the technological process of film deposition, it is possible to find the required optimum technological conditions to prepare such films.

The surface resistance of a thin high-temperature superconducting film is satisfactorily described by the phenomenological model:[1]

$$R_{sur}(t)=\begin{cases}\dfrac{1}{\sigma_n(t)d} & t\geqslant t_c,\\ \dfrac{(\omega\mu_0)^2\sigma_n(t)}{1+[\omega\mu_0\sigma_n(t)\lambda_L^2(t)]^2}\dfrac{\lambda_L^4(t)}{d} & t<t_c,\end{cases} \tag{1}$$

where $t=T/T_c$, T is the temperature, T_c is the superconducting transition temperature, $\sigma_n(t)$ is the conductivity involving normal carriers, $\lambda_L(t)$ is the London penetration depth of the magnetic field in the high-temperature superconductor, ω is the frequency, and μ_0 is the magnetic permeability of vacuum.

The temperature dependences of the conductivity $\sigma_n(t)$ and $\lambda_L(t)$ are given by

$$\sigma_n(t)=\begin{cases}\sigma_n(1)t^{-1} & t\geqslant 1,\\ \sigma_n(1)[t^{\gamma-1}+\alpha(1-t^{\gamma})] & t<1,\end{cases} \tag{2}$$

$$\lambda_L(t)=\frac{\lambda_L(0)}{\sqrt{1-t^{\gamma}}}. \tag{3}$$

Four fitting parameters are used: the dimensionless coefficient α, which characterizes the residual conductivity, the coefficient γ, which determines the temperature dependences $\sigma(t)$ and $\lambda_L(t)$, the film conductivity $\sigma(1)$ at the superconducting transition temperature ($t=1$), and the London depth $\lambda_L(0)$ at zero temperature ($t=0$). Typical values of the parameters for thin films of $YBa_2Cu_3O_{7-\delta}$ (YBCO) superconductor lie within the range indicated in Table I (Ref. 2).

An analysis of numerous experimental measurements of the temperature dependence of $\lambda_L(0)$ has suggested that high-quality YBCO films have a smaller London penetration depth. At the same time, an investigation of the temperature dependence of the resonant frequency of microstripe YBCO-film resonators[3] has shown that a higher Q and lower surface resistance of the films correspond to an increase in the parameter γ in the model (1)–(3). It can therefore be assumed that the model parameters γ and $\lambda_L(0)$ are interrelated.

At low temperatures ($t<0.3$), the resistance R_{sur} is determined by the residual resistance parameter α and it is almost impossible to calculate $\lambda_L(0)$ from the measured surface resistance. At temperatures near the transition point ($0.7<t\leqslant 1$), the parameter γ has the greatest influence on R_{sur}. Thus the model parameters γ and α can be determined by measuring the surface resistance of high-temperature superconducting films of different quality in the superconducting state at two temperature points (near the transition ($0.7<t\leqslant 1$) and for $t\to 0$).

Here we present results of a statistical analysis of the measured surface microwave resistance of YBCO films at $t=0.855$ ($T=77$ K). The films were prepared by magnetron sputtering of a stoichiometric target in a pure oxygen atmosphere. The substrate was r-cut sapphire with a CeO_2 buffer layer. The thickness of the films varied in the range 0.2–0.3 μm.

The dependence of the surface resistance of the high-temperature superconducting films on the parameters of the technological process was investigated to optimize the film preparation conditions. The substrate heater temperature T_h was selected as the control parameter for the process. The deposition temperature was monitored with a detector mounted on the substrate heater. The measurement error for the heater temperature was $\pm 0.5°$C. The rate of deposition

TABLE I.

Parameter	Notation	Range of variation
Residual resistance	α	1–20
Temperature coefficient	γ	1.4–2.45
Film conductivity	$\sigma(1)$	$(1-3.5)\times 10^6$ S/m
London penetration depth	$\lambda_L(0)$	0.130–0.260 μm
Transition temperature	T_c	88–93 K

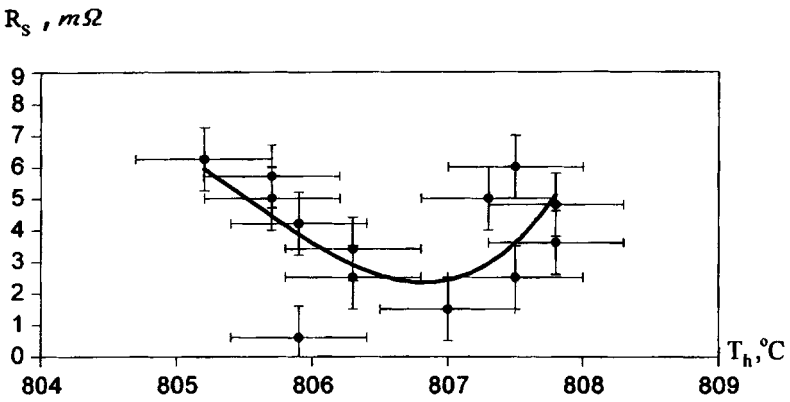

FIG. 1. Measured surface microwave resistance R_{sur} of high-temperature superconducting films fabricated at different substrate holder temperatures T_h.

and the working gas pressure were kept constant from one process to another and were ~10.7 Å/min and 1 Torr, respectively. The surface microwave resistance was measured by a parallel-plate cavity method[4] at a frequency of 10 GHz and $T=77$ K. The measurement error is estimated as being of the order of $\pm$ mΩ. The results of measurements of the surface microwave resistance of thirteen samples are plotted in Fig. 1. The solid curve gives the least-squares approximation to the experimental data by a third-order polynomial. Quite clearly there is an optimum substrate holder temperature for which these films have the lowest surface resistance.

Using the model (1)–(3), we determine the parameters γ and $\lambda_L(0)$ for each sample for selected fixed fitting parameters: $T_C=90$ K, $\sigma(1)=2\times10^6$ S/m, and $\alpha=6$. The thickness of all the films was assumed to be 0.25 μm. We postulate that there is a unique correspondence between the parameters γ and $\lambda_L(0)$, such that their relative variation lies within the possible values given in Table I. We can then find the empirical relation between these parameters:

$$\lambda_L(0)=0.13\exp(1.27-0.5\,\gamma)(\mu\text{m}). \tag{4}$$

The values of γ and $\lambda_L(0)$ calculated using Eq. (4) for the various film samples are plotted in Figs. 2a and 2b, respectively. The solid curves give the least-squares approximation. The high-quality films have a minimum surface resistance, maximum γ, and minimum $\lambda_L(0)$.

In summary, by applying a phenonenological model of the surface resistance of a YBCO film to the results of measurements, we have established a relationship between the model parameters $\lambda_L(0)$ and γ, which allows the parameter γ to be treated as the film quality parameter.

It has been shown that the value of R_{sur} is highly sensitive to the accuracy of maintaining the substrate holder temperature to minimize the surface resistance of the YBCO

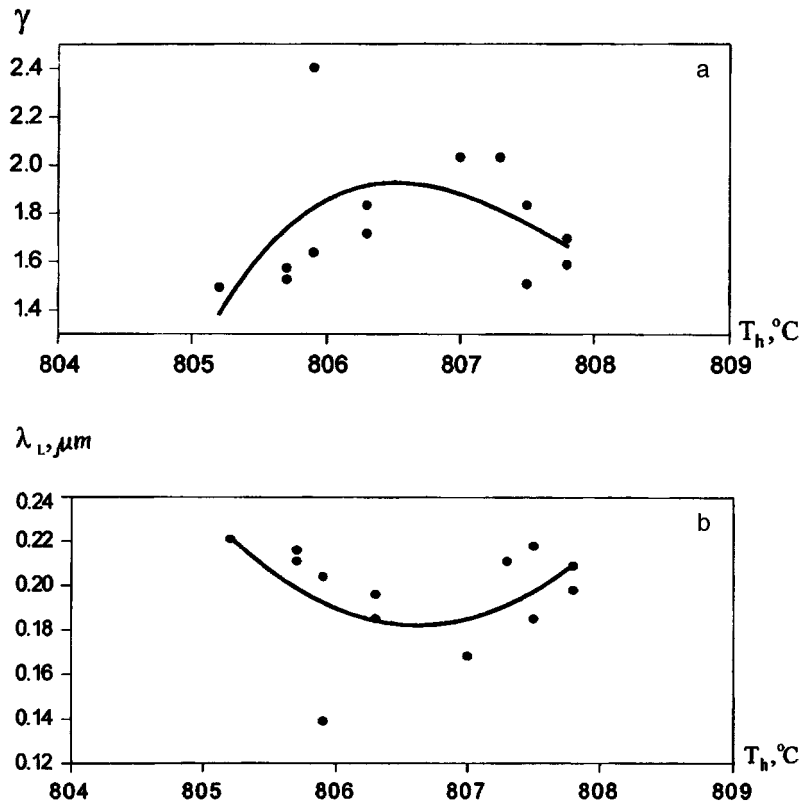

FIG. 2. Calculated values of the parameters γ and $\lambda_L(0)$ for high-temperature superconducting films fabricated at different substrate holder temperatures T_h: a — γ, b — $\lambda_L(0)$.

films and thereby maximize γ. Further measurements of the surface resistance for samples of different quality at low temperatures ($t<0.3$) are required to the determine the interrelation between the parameters γ and α.

This work was carried out under project Nos. 95062 and 95061 (State Program on ''Topical Problems in the Physics of Condensed Media'').

[1] O. Vendik and E. Kollberg, Microwaves RF No. 6, 118 (1993).
[2] O. G. Vendik, A. Yu. Popov, and S. P. Zubko, Pis'ma Zh. Tekh. Fiz. **21**(15), 6 (1995) [Tech. Phys. Lett. **21**, 585 (1995)].
[3] I. B. Vendik, S. S. Gevorgian, D. I. Kaparkov *et al.*, in *Proceedings of the 25th EuMC*, Vol. 2 (Nexus Media, Bologna, 1995), pp. 1205–1208.
[4] R. C. Taber, Rev. Sci. Instrum. **61**, 2200 (1990).

Translated by R. M. Durham

Prediction of interphase energies at the interface of heterogeneous metals

V. M. Yakovlev

Samara State Technical University
(Submitted March 24, 1997)
Pis'ma Zh. Tekh. Fiz. **23**, 85–89 (August 12, 1997)

An approach is proposed to estimate the equilibrium values of the free interphase energies at the interface between two metals using data on their surface energies, heats of vaporization, electron work functions, and Hertzfeld parameters. Examples of the application of this technique to separating binary compositions containing iron are presented. © *1997 American Institute of Physics.* [S1063-7850(97)01608-X]

In the recommended well-known relations used to approximate the interphase energy $\sigma_{A/B}$ in two-phase, two-component metal systems, the discrepancy between the calculations and the experimental data may be 1.5 orders of magnitude or more.[1] These discrepancies are caused mainly by neglecting various characteristic features of the chemical heteronuclear interaction at the metal interface.

It is demonstrated here that the role of interaction selectivity may be taken into account in estimates of $\sigma_{A/B}$ by using the properties of the initial simple substances: the free surface energies $\sigma_{A/B}$ at the interface with its own vapor, the heats of vaporization (for liquid) or sublimation (for the solid phase) $\Omega_{/A(B)}$, the electron work function $\Phi_{A(B)}$, and the dimensionless Hertzfeld parameters $\gamma_{A(B)}$. Examples selected to demonstrate the application of this approach were several compounds of iron with lower-melting metals, for which comparatively reliable experimental data are available for the interphase energies.

It was shown in Ref. 2 that the concept of surface broken bonds and concepts of the phase interface as a two-level energy system may be applied to express $\sigma_{A/B}$ in the form

$$\sigma_{A/B} \simeq |\sigma_A - \sigma_B| \left[1 - \exp\left(- \frac{\Omega_{A/B}}{\nu R T} \right) \right]. \tag{1}$$

Here, $\Omega_{A/B}$ is the interchange energy, R is the universal gas constant, and T is the absolute temperature; the exponential function gives the fraction of compensated bonds as a result of the establishment of equilibrium when an interphase contact is formed (the coefficient is $\nu = 8$ for systems including transition metals).

Relation (1) can give results which agree satisfactorily with the known experimental values of $\sigma_{A/B}$, but is difficult to use because no published experimental values of $\Omega_{A/B}$ are available for many alloys.

It is assumed that the argument of the exponential function in expression (1) gives the relative change in the bond energies accompanying the formation of the compound A/B, and existing models of this characteristic are taken into account. Approximating the main components in the latter, expression (1) is written as follows:

$$\sigma_{A/B} \approx |\sigma_A - \sigma_B| \{ 1 - \exp[- (a \Delta\Omega - B \Delta\Phi + c \Delta\gamma - D)] \}, \tag{2}$$

where $\Delta\Omega = |\Omega_A - \Omega_B|$, $\Delta\Phi = |\Phi_A - \Phi_B|$, $\Delta\gamma = |\gamma_A - \gamma_B|$, $\gamma_{A(B)} = \alpha_0 V^{-1}$, α_0 is the static dipole polarizability of an atom, $V = V_m N_0^{-1}$, V_m is the molar volume, N_0 is Avogadro's number, a, b, and c are proportionality factors, and D is the strengthening effect of the heteroatomic bonds caused by spd hybridization of the electron shells.[3] In formula (2) the parameter $\Delta\Omega$ expresses the imbalance of the homopolar interaction energies, and the term $\Delta\Phi$ is similar to the ionic correction.[4] According to the definition,[5] the value of $\Delta\gamma$ approximates the difference between the deformabilities in different-species neutral Wigner–Seitz cells and defines the energy used in equalizing the molar volumes of the ingredients during alloy formation [the relative deformability of the cell is taken as $\gamma_{A(B)}$ (Ref. 6)].

This analysis for binary systems formed by metals with different types of electron configuration has shown that formula (2) satisfactorily describes most of the known data on $\sigma_{A/B}$ for $a = b = 1$ eV^{-1} and $c = 1$. It has been established that $D \approx f(\Omega_A \Omega_B)^{1/2}$ ($f = 0.27 \pm 0.01$ eV^{-1}) for the compounds of transition and polyvalent nontransition metals with spd strengthening selected in Ref. 3. In systems incorporating only d-metals, including Cu, Ag, and Au, we find $D = 0$.

Table I gives results of estimating $\sigma_{A/B}$ from expression (2) for four systems formed by iron (A) in the liquid (l) and solid polycrystalline (s) states with molten copper, silver, tin, and lead (B), having positive deviations from ideality. The calculations were made using the well-known handbook data on $\Omega_{A(B)}$ and the metal densities at various temperatures, and also data on their atomic weights and volume coefficients of thermal expansion. The values of α_0 did not differ from those used in Refs. 7 and 8: 8.4, 6.0, 7.2, 8.8, and 7.0 (10^{-30} m^3) for Fe, Cu, Ag, Pb, and Sn, respectively. The electron work function of iron is taken as 4.8 eV (Ref. 9)[1)] for the solid phase and 4.31 eV (Ref. 10)[2)] for the liquid phase. Since there are no sufficiently reliable experimental data, the values of Φ_B for molten Cu and Ag were calculated by the formulas presented in Refs. 7 and 11 using the effective number of free electrons per atom[12,13] (4.11 and 3.95 eV, respectively). The work functions of Pb (3.54 eV at 1373 K) and Sn (3.53 eV at 1809 K) were obtained by extrapolating the linear curves $\Phi_B(T)$ obtained in Ref. 14. Measurements of the surface tension and its temperature coefficient for the γ-phase of iron[15] were used as the surface energy of solid-state Fe. Experimental values of $\sigma_{A(B)}$ given in Ref. 16 were taken for the liquid metals.

It can be seen from the data presented in Table I that for these systems the calculated and experimental values of the

 1063-7850/97/080611-02$10.00

TABLE I. Values of the characteristics $V_{A(B)}(10^{-30}\ \mathrm{m}^3)$, $\Delta\Omega$ (eV), $\Delta\Phi$ (eV), D, and also of the surface and interphase energies ($\mathrm{mJ}\cdot\mathrm{m}^{-2}$) at temperature T (K).

Parameter	System $A-B$			
	Fe_sCu_l	Fe_sAg_l	Fe_sPb_l	Fe_lSn_l
T	1398	1373	1373	1809
V_A	11.72	11.70	11.70	13.22
V_B	13.18	19.49	34.92	31.66
$\Delta\Omega$	0.835	1.39	2.39	1.27
$\Delta\Phi$	0.69	0.85	1.26	0.78
D	0	0	0.72	0.875
σ_A	2552.5	2590	2590	1862
σ_B	1320.5	896	380	428
$\sigma_{A/B}$ (calc.)	410	997	1289	35
$\sigma_{A/B}$ (exp.)	430 (Ref. 17)	970 (Ref. 17)	1270 (Ref. 17)	30 (Ref. 18)

interphase energy are similar. This means that $\sigma_{A/B}$ can be estimated using the characteristics of the initial simple substances in a given temperature range.

To conclude, the proposed approach can, in principle, take into account the specific interaction characteristics in a specific pair of metals, without recourse to experiments.

[1)]It is assumed that there is no jump in the electron work function for the $\beta\rightarrow\gamma$ polymorphic transformation in iron.[10]

[2)]The recommended value for a highly disordered structure.

[1] M. P. Dokhov, Pis'ma Zh. Tekh. Fiz. **22**(12), 25 (1996) [Tech. Phys. Lett. **22**, 489 (1996)].
[2] V. M. Yakovlev and A. V. Fomichev, Tr. SNO, Samara State Technical University, 40 (1996).
[3] R. Boom, F. R. de Boer, A. K. Niessen *et al.*, Physica B/C **115**, 285 (1983).
[4] V. M. Yakovlev, A. P. Bakulin, and T. V. Lekomtseva, Deposited Paper No. 2055-V96 [in Russian], VINITI (1996).
[5] C. H. Hodges and M. J. Stott, Philos. Mag. **26**, 375 (1972).
[6] V. M. Yakovlev and B. B. Alchagirov, Izv. Ross. Akad. Nauk Ser. Fiz. **58**(10), 146 (1994).
[7] V. M. Yakovlev, Poverkhnost' No. 12, 18 (1994).
[8] V. M. Yakovlev and B. B. Alchagirov, Deposited Paper No. 81-V95 [in Russian], VINITI (1995).
[9] R. Kh. Burshteĭn, N. A. Shurmovskaya, T. V. Kalish *et al.*, Élektrokhimiya **13**, 799 (1977).
[10] V. S. Fomenko, *Emission Properties of Materials* [in Russian], Naukova Dumka, Kiev (1981).
[11] V. M. Yakovlev, Deposited Paper No. 2385-B93 [in Russian], VINITI (1993).
[12] F. J. Blatt, *Physics of Electronic Conduction in Solids* (McGraw-Hill, New York, 1968).
[13] F. Faber, *Physics of Metals. I. Electrons* [Russ. transl., Mir, Moscow, 1972].
[14] B. B. Alchagirov, Kh. Kh. Kalazhokov, and Kh. B. Khokonov, Poverkhnost' No. 7, 49 (1982).
[15] Kh. B. Khokonov, *Surface Effects in Melts and Solid Phases Formed From Them* [in Russian], Shtiintsa, Kishinev (1974).
[16] B. J. Keene, Int. Mater. Rev. **38**, 157 (1993).
[17] V. Missol, *Surface Energy of Phase Separation in Metals* [in Russian], Metallurgiya, Moscow (1978).
[18] A. A. Zhukov, S. I. Popel', and I. L. Maslova, *Adhesion of Melts and Soldering of Materials* [in Russian], Naukova Dumka, Kiev (1982).

Translated by R. M. Durham

Compensation of parasitic polarization modulation in a fiber-optic gyroscope

É. I. Alekseev and E. N. Bazarov

Institute of Radio Engineering and Electronics, Russian Academy of Sciences, Fryazino
(Submitted March 17, 1997)
Pis'ma Zh. Tekh. Fiz. **23**, 90–94 (August 12, 1997)

It has been shown that the influence of parasitic polarization modulation on the precision of a fiber-optic gyroscope may be reduced substantially by incorporating reflection-type phase modulators with conversion of polarization modes. © *1997 American Institute of Physics.* [S1063-7850(97)01708-4]

Parasitic polarization modulation accompanying the operation of fiber and integrated-optics phase modulators is a serious factor that limits the precision of a fiber-optic gyroscope.[1–3] One method of reducing parasitic polarization modulation involves constructing the phase modulator as two nominally identical halves, between which is inserted a mode converter that converts the polarization modes from one to another.[3] The differential phase modulation of the polarization modes generated in the first half of the phase modulator is compensated by differential phase modulation of the opposite sign in the other half of the modulator. When the phase modulator is constructed using a single-mode fiber waveguide, the mode converter may take the form of suitably positioned fiber compressors, a double symmetric twisted section of fiber of a specific length, a welded or cemented fiber joint with axes of birefringence turned through 90°, and so forth. However, since it is difficult to achieve exactly identical phase-modulator halves and identical ambient conditions, this method of compensation for parasitic polarization modulation is inadequate in many cases. The situation is improved substantially if the phase modulator is designed such that, after the polarization modes have been converted, the radiation then propagates in the forward or return directions along the same path as before the conversion without any time delay. It is obviously technically easier to achieve return propagation. Thus, we shall confine our analysis to this possibility and we shall call the corresponding type of phase modulator a reflection type of modulator.

The Jones matrix of a mode converter in a reflection phase modulator may be expressed, to within a multiplicative factor, as follows

$$K_1=\begin{Vmatrix} 0, & 1 \\ -1, & 0 \end{Vmatrix} \quad \text{or} \quad K_2=\begin{Vmatrix} 0, & 1 \\ 1, & 0 \end{Vmatrix}. \tag{1}$$

In the first case, the entire field pattern is rotated through 90° and in the second case, the mode fields rotate in opposite directions.

We assume that we are dealing with the first type of mode converter. If $N(t)$ is the Jones matrix of the fiber section (or integrated-optics waveguide) where modulation takes place, the Jones matrix $M_1(t)$ of the entire phase modulator (the prime indicates a transposition operation) will be written as:

$$M_1(t)=N'(t)\cdot K_1 N(t)=[\det N(t)]K_1. \tag{2}$$

When writing formula (2), we utilized the fact that the Jones matrices of reciprocal elements for counterpropagating radiation are related by a transposition operation.

It can be seen from Eq. (2) that the time dependence of the Jones matrix of the modulator is only contained in the numerical phase factor, which indicates that parasitic polarization modulation is not observed in this case. Any type of parasitic polarization modulation is eliminated in this case, including that caused by modulation of the dichroism, and the phase modulation efficiency is twice that achieved for single propagation of the radiation in the modulating fiber section or integrated-optics waveguide.

Figures 1a and 1b show a possible design of reflection phase modulator with the first type of mode converter using a Faraday mirror, and methods of incorporating this into a cavity fiber-optic gyroscope and an interferometric fiber-optic gyroscope, respectively. The reflection phase modulators *3* and *3′*, consisting of modulating sections of fiber or integrated-optic waveguide *5* and *5′*, Faraday cells *6* and *6′* with a 45° rotation angle, and mirrors *7* and *7′*, are indicated by the dashed lines in these figures. The interferometric fiber-optic gyroscope (see Fig. 1b) not only incorporates a ring directional coupler *1* but another directional coupler *4*, which is used to connect one or two of the reflection phase modulators to the sensing fiber-optic ring *2*. When the two phase modulators are used in the interferometric fiber-optic gyroscope, the modulation frequencies and the rules of phase variation in the modulators may be the same or different. The optical path lengths with the pigtails to the modulators *3* and *3′* may be the same or may differ by an amount much greater than the coherence length of the radiation source. This offers additional possibilities for processing the signal from the interferometric fiber-optic gyroscope and for its design solutions. Obviously, it is not essential to install two phase modulators in the interferometric fiber-optic gyroscope. If only one phase modulator is installed, the free output of the directional coupler *4* may be used for other purposes. Note also that in order to eliminate the influence of the reflected signal, the radiation source should be connected to the optical channel of the fiber-optic gyroscope via an optical isolator (not shown in the figures).

When the second type of mode converter is used in the phase modulator, Eq. (2) will be replaced by:

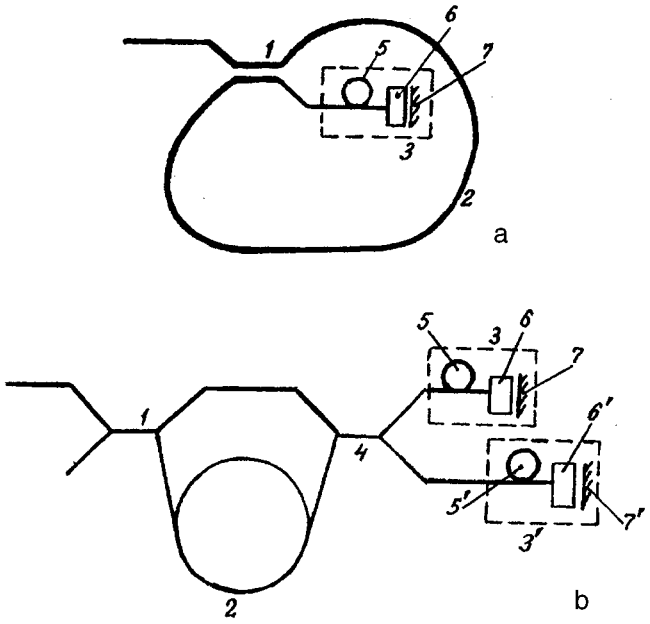

FIG. 1. Methods of connecting a reflection phase modulator to a fiber-optic gyroscope.

$$M_2(t)=N'(t)K_2N(t)$$
$$=\begin{Vmatrix} 2n_{11}n_{21}, & n_{11}n_{22}+n_{12}n_{21} \\ n_{11}n_{22}+n_{12}n_{21}, & 2n_{12}n_{21} \end{Vmatrix}. \quad (3)$$

Here $n_{ij}=n_{ij}(t)$ $(i, j=1,2)$ are the elements of the matrix $N(t)$ introduced above. Equation (3) indicates that, unlike the previous case, the parasitic polarization modulation is not eliminated for an arbitrary matrix $N(t)$. However, we assume that the elements of $N(t)$ satisfy the relation $n_{11}n_{21}=n_{12}n_{22}=0$. Then, instead of Eq. (2), we have

$$M_2(t)=[\mathrm{per}N(t)]K_2, \quad (4)$$

where $\mathrm{per}N(t)=n_{11}n_{22}+n_{12}n_{21}$ is the permanent of the matrix $N(t)$.

Thus, if the equality (4) is satisfied, parasitic polarization modulation will be eliminated in a modulator with the second type of mode converter.

Let us consider one particular case. We suppose that the modulating section of fiber or integrated-optics waveguide is a linear phase plate for which the azimuth of the fast axis is 0°. Then[4] we find $n_{12}=n_{21}=0$, so that the parasitic polarization modulation will be compensated. One possible variant of a reflection phase modulator with a second type of mode converter comprises a series-connected linear phase plate with a time-varying phase delay and 0° fast-axis azimuth, a quarter-wave phase plate with a 45° fast axis azimuth, and a mirror. This type of phase modulator can be incorporated into an interferometric fiber-optic gyroscope as in the previous case.

The authors would like to thank V. P. Gubin and N. N. Starostin for their continuous interest in this work and for useful discussions.

This work was supported by the Russian Fund for Fundamental Research, Grant 96-02-18434.

[1] P. Gangding, H. Shangyuan, and L. Zongqi, Electron. Lett. **22**, 1337 (1986).
[2] E. Kiesel, Proc. SPIE **838**, 129 (1987).
[3] B. Szafraniec and J. Blake, J. Lightwave Technol. **12**, 1679 (1994).
[4] R. M. Azzam and N. M. Bashara, *Ellipsometry and Polarized Light* (North-Holland, Amsterdam, 1977) [Russ. transl., Mir, Moscow, 1970].

Translated by R. M. Durham

Magnetic-field control of gas flow in a supersonic intake

Yu. P. Golovachev, S. A. Il'in, and S. Yu. Sushchikh

A. F. Ioffe Physicotechnical Institute, Russian Academy of Sciences, St. Petersburg
(Submitted May 6, 1997)
Pis'ma Zh. Tekh. Fiz. **23**, 1–5 (August 26, 1997)

A numerical simulation is used to assess the potential for controlling the flow structure in the air intake of a supersonic aircraft by means of an external magnetic field. [S1063-7850(97)01808-9]

1. A pressing problem in the aerodynamics of supersonic aircraft is to ensure that the air intakes operate in the rated mode as the flight conditions change. Here we assess the possibility of solving this problem by means of an external magnetic field.

An analysis is made of two-dimensional steady-state flow of a preionized gas in an air intake shown in Fig. 1. The external magnetic field **B** is directed perpendicular to the plane (X,Y). The flow is described by a system of magnetogasdynamic equations[1] under the following assumptions: $\mathrm{Re}\gg 1$, $\mathrm{Re}_m \ll 1$, and $\alpha \ll 1$, where Re is the Reynolds number, Re_m is the magnetic Reynolds number, and α is the degree of ionization. These assumptions allow us to use the model of an inviscid gas, to assume that the magnetic induction is constant, and to neglect the influence of ionization on the thermodynamic properties (in the calculations, we set the ratio of the specific heats of the gas to $\gamma = 1.4$).

The external magnetic field influences the flow of an electrically conducting gas via the ponderomotive force $\mathbf{F} = \mathbf{j} \times \mathbf{B}$ and the Joule energy release $Q = \mathbf{j} \cdot \mathbf{E}$, where **j** is the density of the electrical conduction current and **E** is the electric field strength. For a given magnetic induction **B**, these quantities are determined by the general form of Ohm's law

$$\mathbf{j} + \mu_e(\mathbf{j} \times \mathbf{B}) = \sigma(\mathbf{E} + \mathbf{V} \times \mathbf{B}), \tag{1}$$

where μ_e is the electron mobility, σ is the electrical conductivity, and **V** is the gas velocity. Under these conditions, the electric field vector lies in the (X,Y) plane. The calculations only take into account the y component of this vector, which corresponds to flow in a two-dimensional MHD channel with solid electrodes. This component of the electric field strength is calculated using the load factor k as given by

$$E_y = -k(\mathbf{V} \times \mathbf{B})_y. \tag{2}$$

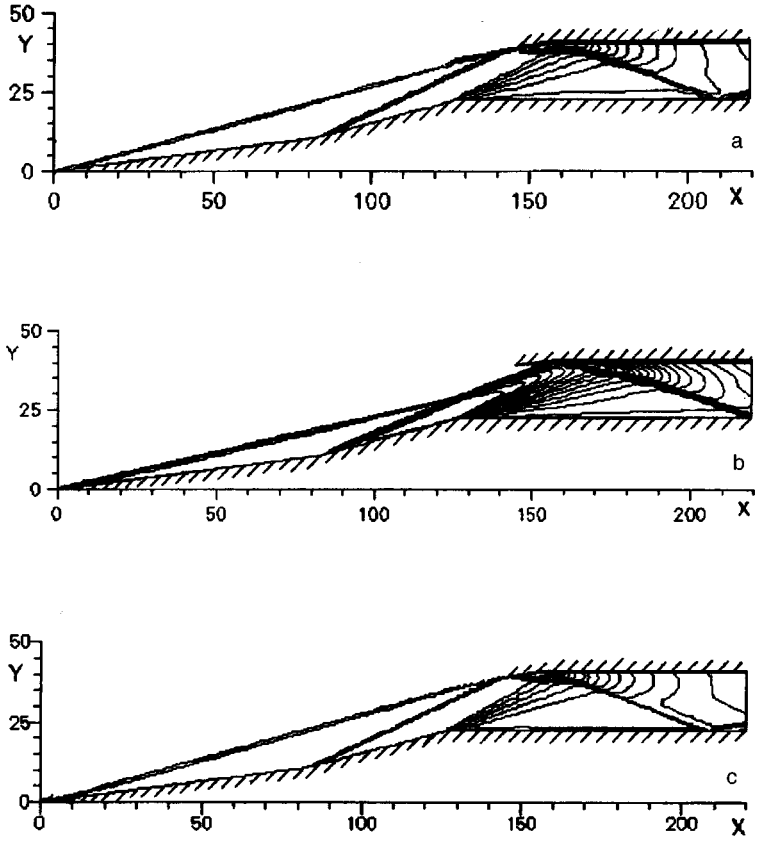

FIG. 1. Density contours: $M = 6$, $B = 0$ (a), $M = 8$, $B = 0$ (b), and $M = 8$, $B \neq 0$ (c).

 1063-7850/97/080615-02$10.00

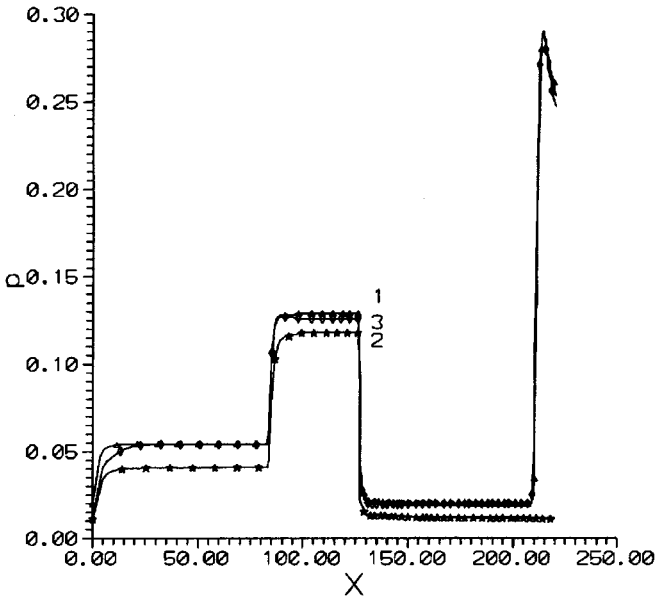

FIG. 2. Pressure distribution over lower wall of channel: $M=6$, $B=0$ (*1*), $M=8$, $B=0$ (*2*), and $M=8$, $B\neq 0$ (*3*).

Under these assumptions, the mass, momentum, and energy balance equations in terms of dimensionless variables have the form

$$\frac{\partial(\rho u)}{\partial x}+\frac{\partial(\rho v)}{\partial y}=0, \tag{3}$$

$$\frac{\partial(\rho u^2+p)}{\partial x}+\frac{\partial(\rho uv)}{\partial y}+S\frac{1}{1+\beta^2}(1-k)u=0, \tag{4}$$

$$\frac{\partial(\rho uv)}{\partial x}+\frac{\partial(\rho v^2+p)}{\partial y}+S\frac{\beta}{1+\beta^2}(1-k)u=0, \tag{5}$$

$$\frac{\partial[(\rho e+p)u]}{\partial x}+\frac{\partial[(\rho e+p)v]}{\partial y}+S\frac{k(1-k)}{1+\beta^2}u^2=0. \tag{6}$$

Here, ρ, p, and e are the density, pressure, and total specific energy of the gas, and u and v are the velocity components along the x and y axes. The interaction between the flux and the magnetic field is characterized by the Hall parameters $\beta=\mu_e B$ and by the Stewart number $S=\sigma B^2 L/\rho_0 V_0$, where L is the characteristic linear flow scale, and ρ_0, V_0 are the scaling values of the density and gas velocity.

It is assumed that the projection of the gas velocity on the x axis exceeds the velocity of sound over the entire calculation range, so that the system (3)–(6) is x-hyperbolic. The parameters of the incoming flux, which is assumed to be parallel to the x axis, are defined as the initial conditions for $x=0$. The condition of vacuum tightness is used at the walls of the channel. The problem is solved numerically using an explicit sustaining shock-capturing scheme.[2]

2. Figure 1 shows contours of the density field demonstrating the structure of the gasdynamic field of this flow, which contains density discontinuities and rarefaction waves, formed at kinks on the air intake profile and interacting with the channel walls and with one another. Figures 1a and 1b show results for flows without a magnetic field. Figure 1a corresponds to the rated operating mode of the air intake where the incoming flux has the Mach number $M=6$. In this case, the density discontinuities formed at the kinks on the profile of the lower wall converge at the front edge of the rim. Figure 1b gives results for flow with the nonrated Mach number $M=8$. Figure 1c shows flow with Mach number $M=8$ in the presence of an external magnetic field. In this case, the Stewart number was assumed to be constant, $S=0.005$ for $0<x<12$, decaying linearly to zero for $12<x<22$ and equal to zero for $x\geqslant 22$. The Hall parameter was $\beta=0.1$ and the load factor was $k=0.5$. The results demonstrate that a shock wave structure consistent with the rated operating mode of the air intake can be reconstructed with the aid of an external magnetic field. Figure 2 shows the pressure distributions over the lower wall of the air intake for the conditions corresponding to Figs.1a–1c. The pressure is given relative to the total pressure in the incoming flux.

The authors would like to thank N. I. Akatnov for useful discussions of this work.

This work was supported by the Russian Fund for Fundamental Research (Grant No. 99-01-00596).

[1] M. Mitchner and C. H. Kruger, Jr., *Partially Ionized Gases* (Wiley, New York, 1973) [Russ. transl., Mir, Moscow, 1976].
[2] A. V. Rodionov, Zh. Vychisl. Mat. Mat. Fiz. **27**, 1853 (1989).

Translated by R. M. Durham

High-temperature high-dose implantation of N^+ and Al^+ ions in 6H–SiC

R. A. Yankov, M. Voelskow, W. Kreissig, D. V. Kulikov, J. Pezoldt, W. Skorupa, Yu. V. Trushin, V. S. Kharlamov, and D. N. Tsigankov

Rossendorf Research Center, Dresden, Germany;
A. F. Ioffe Physicotechnical Institute, Russian Academy of Sciences, St. Petersburg;
Ilmenau Technical University, Ilmenau, Germany
(Submitted April 5, 1997)
Pis'ma Zh. Tekh. Fiz. **23**, 6–14 (August 26, 1997)

A series of experimental and theoretical investigations has been initiated for 6H–SiC samples sequentially implanted with high doses of N^+(65 keV) + N^+(120 keV) + Al^+(100 keV) + Al^+(160 keV) ions at temperatures between 200 and 800 °C. Nitrogen and carbon distribution profiles are measured by ERD and structural defect distributions are measured by Rutherford backscattering with channeling. A comparison between the experimental data and the results of computer simulation yields a physical model to describe the relaxation processes of the implanted SiC structure, where the entire implanted volume is divided into regions of different depth, having different guiding kinetics mechanisms. [S1063-7850(97)01908-3]

INTRODUCTION

Wide-gap semiconductors based on SiC solid solutions have recently attracted considerable interest for the development of new optoelectronic and high-temperature devices. The quasibinary system $(SiC)_{1-x}$ $(AlN)_x$ is probably the most promising for these applications at the present time. However, the published data apply mostly to polycrystalline ceramics fabricated by sintering[1] and to epitaxial layers.[2]

EXPERIMENTAL AND CALCULATED DATA

Experimental investigations were made of $(SiC)_{1-x}$ $(AlN)_x$ samples fabricated by ion beam synthesis. Wafers of (0001)-oriented *n*-type 6H–SiC were bombarded with N^+ and Al^+ ions at elevated substrate temperatures using the Danphysik accelerator at the Rossendorf Research Center, Germany. The implantation parameters were selected to obtain buried layers of $(SiC)_{1-x}(AlN)_x$ with $x=0.2$. Each sample was bombarded in the following order: first with 65 keV nitrogen ions at a dose of 5×10^{16} cm^{-2}, then with 120 keV nitrogen ions at a dose of 1.3×10^{17} cm^{-2}, followed by 100 keV aluminum ions at a dose of 5×10^{16} cm^{-2} and then 160 keV aluminum ions at a dose of 1.3×10^{17} cm^{-2}. The ion energies were selected so that the distribution profiles of the N^+ and Al^+ ions overlapped under the overall bombardment. During implantation the ion current density was maintained between 0.6 and 1 μA/cm^2 at substrate temperatures of 200, 400, 600, and 800 °C, for which we used an Ohmically heated, temperature-calibrated substrate holder. After implantation, the samples were investigated by Rutherford backscattering in conjunction with channeling (RBS/C) method[4] using a 1.4 MeV He^+ ion beam, and also by the ERD method, to determine the depth distribution of nitrogen and carbon. The RBS spectra were processed using a computer program developed at the Rossendorf Research Center, which yielded depth distributions of structural defects (Fig. 1a).

The TRIRS and DYTRIRS computer codes[4–6] were used to calculate the ballistic distributions of the implanted ions and defects, and also to calculate the changes in the density of the SiC components for high-temperature implantation at the corresponding doses. Ballistic distributions of N^+ and Al^+ ions (DETRIRS) (Fig. 1a, curve *1*) and total defect distributions (Fig. 1a, curve *2*) were obtained. Ballistic distributions of implanted nitrogen (as a result of all four successive bombardments at the doses used experimentally) are plotted in Fig. 1b) (DYTRIRS).

A comparison between the ballistic data (see curve *2* in Fig. 1a) and the RBS results for irradiation at 200 °C shows that this at this temperature the modified (''amorphous'') material does not anneal at the deposition depth of the implanted nitrogen and aluminum ions (curve *1*).

Assuming, for a rough estimate, that all vacancies and interstitial atoms separated by spontaneous recombination distances (see, for example, Refs. 7 and 8) recombine athermally, the residual intrinsic defects and implanted ions will give an overall profile lying below the RBS experimental data (curve *3*). The two limiting cases (only ballistic distributions — curve *2* and allowance for total recombination — curve *3*) show substantial differences, and a comparison between these and the experimental data (RBS)[3] reveals the role of diffusion processes in high-temperature implantation in regions of the irradiated SiC of different depth.

At higher irradiation temperatures however, the distribution profiles of the scattering centers change with depth. Since RBS is sensitive to any scattering centers for He^+, including implanted ions, single intrinsic defects (vacancies and interstitial atoms in Si and C sublattices), and clusters (both intrinsic and impurity defects), the experimentally determined[3] different behavior of the scattering center profiles over depth indicates that different annealing mechanisms operate at different depths in the implanted material.

The distribution profiles of N^+ ions (Fig. 1b, ERD) were determined experimentally (ERD) for SiC samples irradiated at different temperatures. A comparison between these pro-

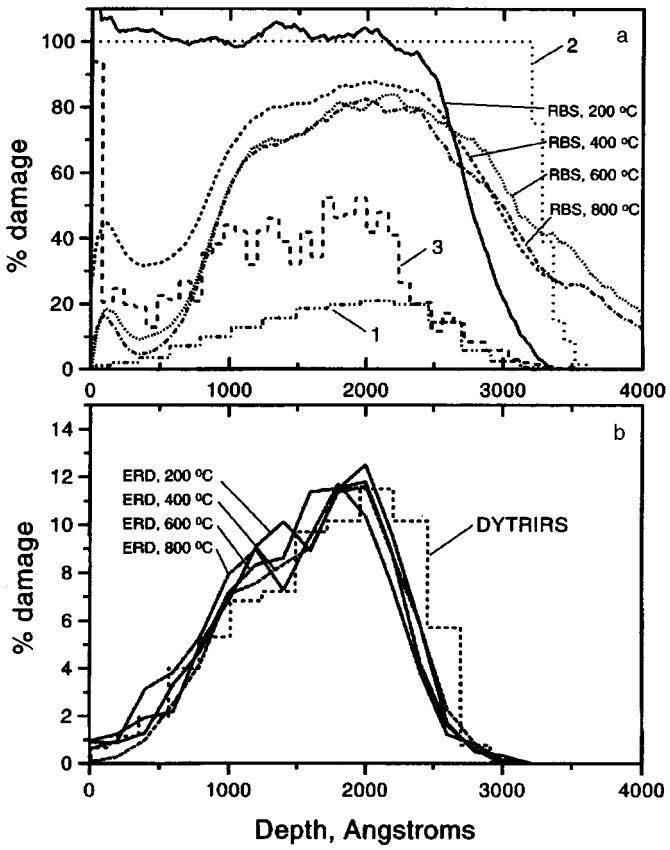

FIG. 1. Comparison between experimental and calculated ballistic characteristics of implanted silicon carbide; a — RBS experimental profiles of defect distribution at various substrate temperatures; *1* — calculated profile of implanted nitrogen and aluminum ions, *2* — calculated total defect profile allowing only for ballistic (cascade) processes, *3* — calculated ballistic defect profile allowing for total athermal recombination; b — ERD profiles of nitrogen distribution at various substrate temperatures; DYTRIRS — calculated ballistic profile of nitrogen distribution taking into account all successive irradiation processes.

files and the calculated ballistic nitrogen profile for the entire bombardment sequence at the corresponding experimental doses (Fig. 1b, DYTRIRS) shows that at all the temperatures used, the implanted nitrogen undergoes very little diffusion which, reflects the slight change in the overall distribution profiles of the scattering centers for the central regions of the implanted SiC obtained by RBS.

The influence of N^+ and Al^+ irradiation can also be seen in a change in the concentration of SiC components. A very common consequence of implantation is the formation of carbon nonuniformity. A comparison between the change in the carbon concentration produced only by the ballistic action of the implanted ions (Fig. 2, DYTRIRS) and the experimentally determined (ERD) depth dependences of the carbon concentrations at various irradiation temperatures (Fig. 2) suggests that an increase in implantation temperature leads to diffusion-induced changes in the structure of the material. However, like the RBS data, these experiments indicate that the structure of the material during high-temperature implantation evolves differently in regions of different depth.

The entire irradiated material may thus be divided into five regions according to depth (regions *A*, *B*, *C*, *D*, and *E* in Fig. 1) in which different diffusion reactions may play a dominant role in the kinetics.

PHYSICAL MODEL

By comparing the experimental RBS and ERD data with the ballistic calculations, we will now give a qualitative description of the main physical reactions determining the kinetics of the radiation defects in SiC in regions of different depth in order to put forward a physical model to describe the annealing processes in high-temperature implantation.

We shall begin with the most defect-saturated region *D* (Fig. 1).

REGION *D* (BETWEEN 1500 AND 3000 Å)

This region has the highest concentration of scattering centers (up to 80%). At high irradiation temperatures, between 400 and 800 °C, the structure of the region changes relatively little. It receives the highest concentration of implanted N^+ and Al^+ ions (Fig. 1, curve *1*) and electron microscopy reveals fairly good long-range order. Since temperatures up to 800 °C have little influence on the number of

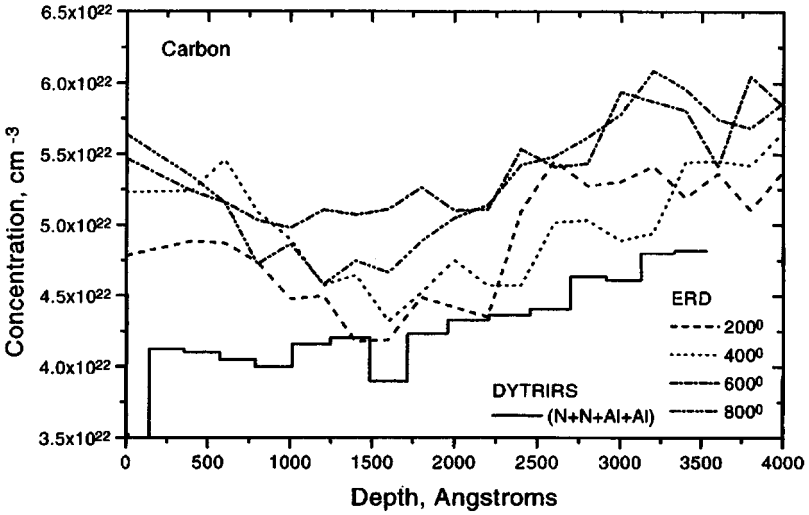

FIG. 2. Comparison between experimentally determined (ERD) carbon distributions at various substrate temperatures with ballistic calculated carbon profile (DYTRIRS).

scattering centers in this region (Fig. 1, RBS) and the quantity of carbon increases with increasing irradiation temperature (Fig. 2, ERD), we may postulate that the implanted N^+ and Al^+ ions are distributed in Si and C vacancies as a result of spontaneous recombination of interstitial ions with existing radiation-induced vacancies. Mobile defects may accumulate around these vacancies as a result of local distortions (replacement of Si and C ions by N and Al ions). These structures clearly do not dissociate at the temperatures used and make a major contribution to the He^+ scattering. Some decrease in the defect concentration in this region (up to 20%) is caused by defects mobile by diffusion, such as carbon interstitial atoms (for which the migration activation energy is $\varepsilon_{iC}^m = 1.47$ eV (Ref. 9)). However, it also follows from Ref. 9 that the energy of formation of a carbon vacancy is $\varepsilon_{vC}^f = 2.63$ eV. Thus some radiation-induced mobility of carbon vacancies may occur at these irradiation temperatures. It can be seen from Fig. 2 that a change in the carbon concentration is observed in this region and may be attributed to the formation of clusters of interstitial carbon atoms with increasing irradiation temperature.

Assuming that the mobile defects (as can be seen from Figs. 1 and 2) are intrinsic carbon defects — interstitial atoms and vacancies — we can describe the kinetics of the increase in the carbon concentration in region *D* as resulting from the formation of carbon atom clusters and from exchange reactions between sites of matrix and impurity atoms in overstressed local zones of enhanced implanted ion concentrations. Since we have postulated that the nitrogen and aluminum ions can occupy Si and C vacancies, the carbon clusters may also be fairly regularly distributed in the lattice and may grow as a result of the attachment of mobile defects.

REGION *E* (DEPTHS GREATER THAN 3000 Å)

The behavior of the RBS spectra in implanted SiC and the calculated concentrations of centers which contribute to the scattering of He^+ ions (Fig. 1), shows that in this region the distribution profiles of the scattering centers are not very sensitive to changes in the irradiation temperature between 400 and 800 °C. This behavior may be attributed to stopping of mobile defects (of the carbon subsystem) caused by the formation of clusters of intrinsic defects. It should also be borne in mind that this region contains almost no implanted ions (Fig. 1, curve *1*). The clusters of intrinsic defects appearing in this region should therefore be formed homogeneously (unlike those in region *D*). The irradiation parameters of the samples at different temperatures were the same and thus the diffusion fluxes of irradiation-generated mobile defects are also the same, differing only in terms of their diffusion rates. The defect ranges according to the RBS data[3] (Fig. 1) are almost independent of the irradiation temperature. The same tendency can be identified from the experimental results plotted in Fig. 2. This should imply that the point-defect trapping parameter for cluster formation (the cluster formation parameter) depends only weakly on the irradiation temperature, since the cluster formation process is proportional to the concentration of mobile defects.

It may also be postulated that vacancy clusters are formed in this region since the distributions of scattering centers (Fig. 1, RBS) and the carbon distributions (Fig. 2, ERD) suggest monotonic changes in concentration which may be attributed to the mobility of vacancies.

REGION *C* (DEPTHS BETWEEN 750 AND 1500 Å)

In this region, predominantly interstitial carbon atoms may be considered to be mobile. Electron microscopy indicates that at 800 °C this region contains large stacking faults of the type interstitial dislocation loops having dimensions up to hundreds of angstroms in diameter. These loops may be formed from mobile interstitial carbon atoms during high-temperature irradiation. The changes in the RBS spectra in this region,[3] and therefore in the distribution profiles of the scattering centers (see Fig. 1), can thus be ascribed to drift of mobile defects with the formation of additional dislocation loops. This is accompanied by an increase in the carbon content (see Fig. 2).

REGION *B* (DEPTHS BETWEEN 200 AND 750 Å)

In this region, as in the deeper regions of the SiC samples, defects in the carbon subsystem are mobile by way of diffusion. However, as can be seen from the sharp drop in the defect concentration given by the RBS data (Ref. 3 and Fig. 1) and the recovery of the carbon concentration in the ERD experiments (Fig. 2), the largest contribution to the changes in the concentrations of scattering centers (compared with all the other thermally activated reactions) is made by a sink for mobile defects at the surface of the sample. As a result, the ordered crystal structure of the material is partially restored, even at 400 °C. The electron microscopy data indicate that the crystal structure is almost restored in this region (at 800 °C). It may be supposed that, as a sink, the surface predominantly influences the mobile defects in the form of interstitial carbon atoms (or even vacancies at higher temperatures). Thus, the drift to the surface is stronger than the other defect reactions, leading to rapid recovery of the structure.

REGION *A* (DEPTHS UP TO 200 Å)

The surface region of the irradiated samples (to depths of approximately 200 Å) is in fact a defect sink. This leads to an increased concentration of scattering centers as a result of diffusion, as is shown fairly clearly by the RBS data (Fig. 1a). The dominant mobile defects are interstitial carbon atoms, and their number should increase near the surface sink. The results of ERD experiments (Fig. 2) support this interpretation.

CONCLUSIONS

These experimental results of RBS measurements of the defect distribution profile and ERD measurements of the carbon and implanted nitrogen distributions, together with the

results of ballistic calculations of the same characteristics of irradiated 6H–SiC samples, have revealed regions of implanted silicon carbide at different depths which exhibit substantial differences in structure. By comparing the calculated and experimental data, it was possible to formulate a physical model to describe the evolution of the defect structure in implanted silicon carbide at high temperatures which takes into account the characteristics of the depth distribution of the radiation defects in the irradiated material.

The next step in our studies of the characteristics of implanted 6H–SiC samples will involve an electron microscope examination of the structure and the solution of a system of transport equations to describe the behavior of radiation defects, in accordance with the physical model described here.

This work was partially supported by the Russian Fund for Fundamental Research, Grant No. 96-02-1995.

[1] R. Ruh and A. Zangvil, J. Am. Ceram. Soc. **65**, 260 (1982).
[2] Sh. A. Nurmagomedov, A. N. Pikhtin, V. N. Razbegaev, G. K. Safaraliev, Yu. M. Tairov, and V. F. Tsvetkov, Pis'ma Zh. Tekh. Fiz. **12**, 1043 (1986) [Sov. Tech. Phys. Lett. **12**, 431 (1986)].
[3] R. A. Yankov, N. Natzopoulos, W. Fukarek, M. Voelskow, V. Hera, J. Pezoldt, and W. Skorupa, Mat. Res. Soc. Symp. Proc. **438**, 271 (1997).
[4] B. J. Ber, A. V. Merkulov, V. S. Kharlamov, Yu. V. Trushin, and E. E. Zhurkin, Zh. Tekh. Fiz. **66**(3), 54 (1996) [Tech. Phys. **41**, 261 (1996)].
[5] Yu. V. Trushin, B. J. Ber, V. S. Kharlamov, and E. E. Zhurkin, J. Nucl. Mater. **233/237**, 991 (1996).
[6] B. J. Ber, V. S. Kharlamov, Yu. V. Trushin, A. V. Merkulov, and E. E. Zhurkin, in *Proceedings of the Tenth International Conference on Ion Beam Modification of Materials*, Albuquerque, NM, 1996, paper Tu29.
[7] V. V. Kirsanov, A. L. Suvorov, and Yu. V. Trushin, *Radiation-Induced Defect Formation Processes in Materials* [in Russian], Énergoatomizdat, Moscow (1985).
[8] Yu. V. Trushin, *Theory of Radiation Processes in Metal Solid Solutions* (Nova Science Publishers, New York, 1996).
[9] H. Huang and N. Ghoniem, J. Nucl. Mater. **212/215**, 148 (1994).

Translated by R. M. Durham

Determination of the time-dependent plastic properties of solids by dynamic nanoindentation

Yu. I. Golovin, V. I. Ivolgin, V. V. Korenkov, and A. I. Tyurin

G. R. Derzhavin State University, Tambov
(Submitted March 13, 1997)
Pis'ma Zh. Tekh. Fiz. **23**, 15–19 (August 26, 1997)

A new method is described to determine the time-dependent elastoplastic and dissipative properties of solids in nanovolumes by recording the instantaneous values of the stress and depth of penetration of a rigid indenter. Measurements are also made of the energy W_1 supplied to the indenter, the energy U dissipated in the insertion process, and the energy W_0 returned to the indenter on unloading. Results of measurements of the dynamic microhardness and also of the energies W_0 and U for NaCl crystals are presented as functions of the duration of contact between the indenter and the surface for times between 1 ms and 10 s. © *1997 American Institute of Physics.* [S1063-7850(97)02008-9]

One of the simplest and most widely used methods of determining the mechanical properties of solids in microvolumes and nanovolumes involves indentation with a rigid indenter, followed by calculation of the hardness H as the ratio of the indentation force F to the area A of the resulting indentation (Refs. 1–3). In fact, both the conventional method and the ''nanoindentation'' technique, which has recently enjoyed great popularity,[4–6] estimate the quasistatic elasticoplastic properties of the material in thin surface layers. The hardness H determined in this way cannot reflect the dynamic properties of the material or the kinetic characteristics of any specific physical processes in this material since it sums *post factum* the results of all events which have taken place at different stages of formation of the indentation. Consequently, H does not have a clear physical meaning and cannot be correlated with known fundamental characteristics of the material. In many cases, the potential usefulness, behavior, and nature of the various secondary processes accompanying short-term contact interaction are determined by the dynamics of the structural defects and plastic flow in the contact zone and also by the absorbed energy. Such situations are frequently encountered, for example, in dry abrasive wear of contacting solids, surface damage by fine rap-

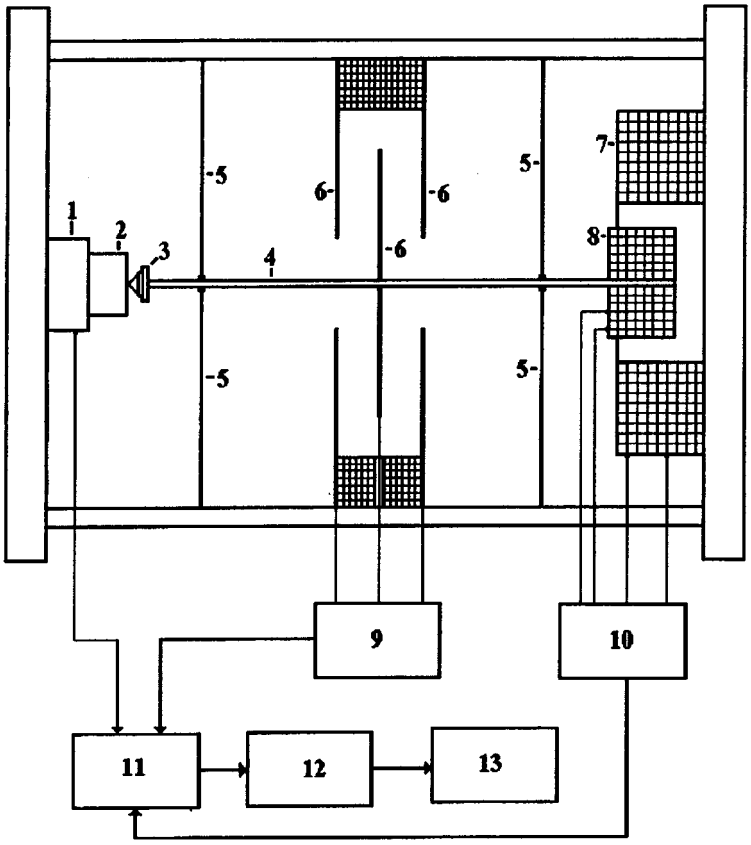

FIG. 1. Diagram of apparatus: *1* — piezoelectric transducer, *2* — sample, *3* — indenter, *4* — rod, *5* — rod suspension elements, *6* — capacitative displacement meter, *7* — fixed coil, *8* — moving coil, *9* — unit for processing signal from capacitative detector, *10* — current pulse generator, *11* — analog-to-digital converter with signal switch, *12* — computer, and *13* — printer.

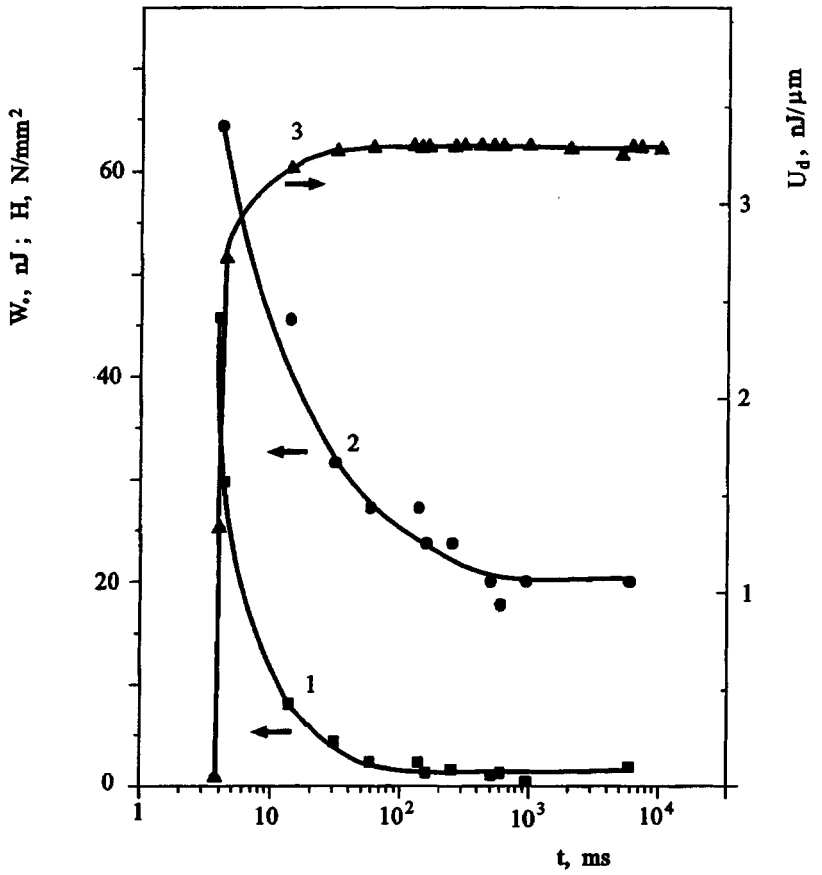

FIG. 2. Kinetic dependences of the recoil energy W_0 (1), the dynamic hardness H_d (2), and the reduced absorbed energy U_d (3) for dynamic nanoindentation of NaCl crystals.

idly impinging particles, crushing and fine grinding, mechanical alloying, at the tip of a rapidly growing crack in quasibrittle fracture, and so on.

In this article we describe a method of determining the dynamic values of the hardness H_d and the time-dependent component of the energy absorbed during indentation, and we present the first results. The method (Fig. 1) involves indenting the surface with a rigid indenter attached to the end of a horizontally suspended rod to which an electrodynamic drive mechanism applies an impulse $F(t)$ whose profile (rectangular, trapezoidal, triangular), amplitude (between 0.1 mN and 1 N), rise times, and duration (between 50 μs and 10 s) can be regulated. A capacitive displacement meter records the instantaneous depth of penetration $h(t)$ of the indenter with a resolution of 10 nm, and a piezoelectric transducer measures the penetration resistance force. The meters measuring the displacement, the forces, and the instantaneous value of the current in the drive mechanism are fed to a computer via an analog-to-digital converter. The program used to process the recorded information yields instantaneous values of h, H_d, the indenter recoil energy W_0, the energy U absorbed during indentation, and the reduced absorbed energy U_d. The energy U was determined from the difference between the work W_1 done by the drive mechanism (or the kinetic energy of the rod before contact between the indenter and the surface of the sample) and the kinetic recoil energy W_0 of the rod, and U_d was determined by normalizing U to the volume of the indentation.

The experiments were carried out at room temperature using nominally pure NaCl crystals, usually used to calibrate indentometers. The indenter was set in motion by a rectangular impulse $F=0.2$ N of duration τ between 1 ms and 10 s. Figure 2 shows that the dynamic hardness H_d has the usual value of 200 N/mm^2 for NaCl for $\tau \geqslant 1$ s and then increases rapidly with decreasing τ, reaching $\sim$650 N/mm^2 at $\tau=4$ ms. Similar behavior of $H_d(t)$ was observed in Refs. 7 and 8, when a long-term constant force was abruptly applied to the indenter. By terminating the loading in the early stages, it is possible to investigate the behavior of W_0 as a function of the loading time. This dependence proved to be even stronger than $H_d(\tau)$ (Fig. 2). For $\tau=4$ ms, W_0 was 45 nJ whereas for $\tau \geqslant 10^2$ ms, it was close to the amplitude of the mechanical fluctuations of the rod with the indenter ($\sim$1 nJ). The time-dependent component of the reduced absorbed energy U_d also varied by several factors of ten as τ increased from a few milliseconds to tens of milliseconds (Fig. 2). It is deduced from these results that H_d, W_0, and U_d are independent characteristics of the material, describing its time-dependent elastoplastic and dissipative properties in a contact zone of $\sim 1\ \mu$m^3 volume. The characteristic times of variation of H_d, W_0, and U_d are clearly determined by the dynamics of the plastic flow in the contact zone under the action of a short-term constant applied force. At the same time, they contain information on the dynamics of the nucleation and displacement of structural defects, which are elementary carriers of this information under conditions of high local stresses and relative deformation rates. In fact, the average contact stresses $\sigma \approx H_d$ for $\tau=4$ ms are almost 1000

times the yield stress for quasistatic uniaxial compression. Despite the low absolute rate of displacement of the indenter, $\dot{h}<1$ mm/s at the maximum, the rate of relative displacement $\dot{\varepsilon}\approx\dot{h}/h$ reaches values of $\sim 10^3$ s^{-1} for $h<1\,\mu$m, which are typical of the high-velocity impact of macroscopic solids.

To sum up, we have devised a method of studying the behavior of a material exposed to high-amplitude short-term applied stresses, which simulate the situations frequently encountered in the contact interaction between two solids. These results indicate that the rate of energy dissipation increases substantially with decreasing contact time ($\tau<20$ ms) and with increasing dynamic microhardness for $\tau<1$ s.

[1] V. K. Grigorovich, *Hardness and Microhardness of Metals* [in Russian], Nauka, Moscow (1976).
[2] É. V. Ryzhkov, Yu. V. Kolesnikov, and A. G. Suslov, *Contact Between Solids Under Static and Dynamic Loads* [in Russian] (Naukova Dumka, Kiev, 1982).
[3] A. A. Gudkov, and Yu. I. Slavskiĭ, *Methods of Measuring the Hardness of Metals and Alloys* [in Russian] (Metallurgiya, Moscow, 1982).
[4] M. F. Doerner, D. S. Gardner, and W. D. Nix, J. Mater. Res. **1**, 845 (1986).
[5] W. C. Oliver and G. M. Pharr, J. Mater. Res. **7**, 1564 (1992).
[6] Y. Mutakami, K. Tanaka, M. Itokazu, and A. Shimamoto, Philos. Mag. A **69**, 1131 (1994).
[7] Yu. I. Golovin and A. I. Tyurin, JETP Lett. **60**, 742 (1994).
[8] Yu. I. Golovin and A. I. Tyurin, Fiz. Tverd Tela (St. Petersburg) **38**, 1812 (1996) [Phys. Solid State **38**, 1000 (1996)].

Translated by R. M. Durham

Investigation of the photoluminescence and modification of InGaP/GaAs/InGaAs heterostructures by near-field scanning microscopy

S. V. Gaponov, V. F. Dryakhlushin, V. L. Mironov, and D. G. Revin

Institute of Physics of Microstructures, Russian Academy of Sciences, Nizhniĭ Novgorod
(Submitted March 14, 1997)
Pis'ma Zh. Tekh. Fiz. **23**, 20–25 (August 26, 1997)

This study deals with the local spectroscopy and modification of semiconducting InGaP/GaAs/InGaAs quantum-well heterostructures by near-field scanning optical microscopy. The spatial distribution of the photoluminescence intensity in these structures is investigated and spatial nonuniformity of the photoluminescence is observed as a result of the nonuniform properties of the InGaP layers. It is shown for the first time that local quenching of the photoluminescence may be achieved by optically induced impurity diffusion near the quantum well, and this may be utilized to develop low-dimension semiconducting devices. © *1997 American Institute of Physics.* [S1063-7850(97)02108-3]

One application of near-field scanning optical microscopes is the spectroscopy of semiconducting structures. For instance, the photoluminescence of quantum wells and wires in GaAs/AlGaAs structures was studied in Ref. 1. The diffusion length of the photoexcited carriers was determined from the change in the profile of the photoluminescence intensity from the quantum well at the boundary with a quantum wire. The authors of Ref. 2 studied the spatial distribution of the photoluminescence intensity near the etching boundary of quantum-well GaAs/AlGaAs structures. The size of the transition region of reduced photoluminescence intensity was ~ 2.5 μm, which, in the opinion of the authors, could be attributed to diffusion of nonequilibrium carriers toward the etching boundary, followed by nonradiative recombination. The photoluminescence of partially ordered GaInP structures was investigated in Ref. 3. It was shown that the degree of order of these structures may be assessed from the position and width of the spectral peaks. Another important trend is the use of near-field scanning optical gyroscopes to modify the properties of surfaces, including the development of new methods of nanolithography[4] and improving the information recording density.[5]

In the investigation reported here, near-field microscopy and spectroscopy are used to study the local photoluminescence of GaAs/InGaAs structures and also to assess the possibility of local suppression of the photoluminescence in these structures.

The experiments were carried out using a near-field optical microscope, developed at the Institute of Physics of Microstructures of the Russian Academy of Sciences, combined with a scanning tunneling microscope.[6] The probe was an adiabatic, tapered, single-mode fiber coated with a layer of metal by an angular deposition method. The aperture of the probes used to obtain images of test objects was $\leqslant 100$ nm. Probes with a ~ 1 μm aperture have been used in the experiments to study photoluminescence. The probe radiation source was a cw argon laser ($\lambda = 0.514$ μm). For the spectroscopic investigations, the photoluminescence radiation transmitted by the sample was passed through a bundle of multimode fibers to an MDR-23 monochromator and recorded with a photomultiplier. The sample itself functioned as a filter for the laser radiation and was transparent to the radiation from the quantum well.

We studied two structures: an InGaP/GaAs/InGaAs/GaAs/InGaP laser heterostructure and a GaAs/InGaAs/GaAs heterostructure, whose active regions were ~ 10 nm wide $In_{0.2}Ga_{0.8}As$ and ~ 8 nm wide $In_{0.22}Ga_{0.78}As$ quantum wells, respectively. Both structures were grown on (001) GaAs substrates by organometallic vapor-phase epitaxy, but differed in that one of the structures had InGaP confining layers. These structures are of interest because $In_xGa_{1-x}P$ ($x \sim 0.5$) is being increasingly widely used in heterolasers[7,8] and possesses unusual properties associated with the ordering of the Ga and In atoms, which are not distributed statistically but in alternate (111) or ($\bar{1}\bar{1}\bar{1}$) planes.[9] The photoluminescence spectra of the two heterostructures in the transparency region of GaAs exhibited intense peaks at ~ 980 nm, which correspond to the emission from the InGaAs quantum wells. Here we only studied this part of the photoluminescence spectra of the heterostructures. The photoluminescence signal was reliably recorded at room temperature.

Figure 1 shows the pattern of the integrated photoluminescence intensity of the InGaP sample, obtained with a near-field scanning optical microscope. The field of view was 50×50 μm. Regions of different photoluminescence intensity, elongated in one direction, are clearly visible. The transverse dimension of these regions was around 15 μm. The photoluminescence spectra obtained at different points in these regions had the same profile but differed in intensity. They were similar to the photoluminescence spectrum measured by the usual technique when the diameter of the laser beam focused on the sample is 50–100 μm. Investigations of the structure without InGaP revealed that its luminescence was highly uniform over the area. The nonuniformity of the luminescence from the InGaP structure can probably be ascribed to the presence of alternating ordered and disordered regions, or defects in the InGaP layer.

In addition to studying the photoluminescence properties, we also investigated the possibility of local quenching of the photoluminescence in InGaP structures as a result of stimulated diffusion of impurities from the surface of the sample toward the luminescent layer. For this purpose we

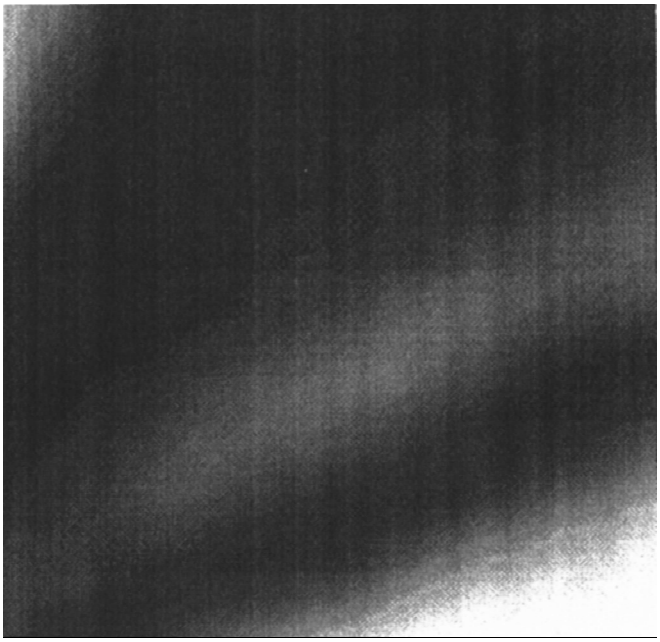

FIG. 1. Pattern of integrated photoluminescence intensity of InGaP/GaAs/InGaAs/GaAs/InGaP heterostructures at 300 K. The frame size is 50×50 μm. The maximum intensity corresponds to white light.

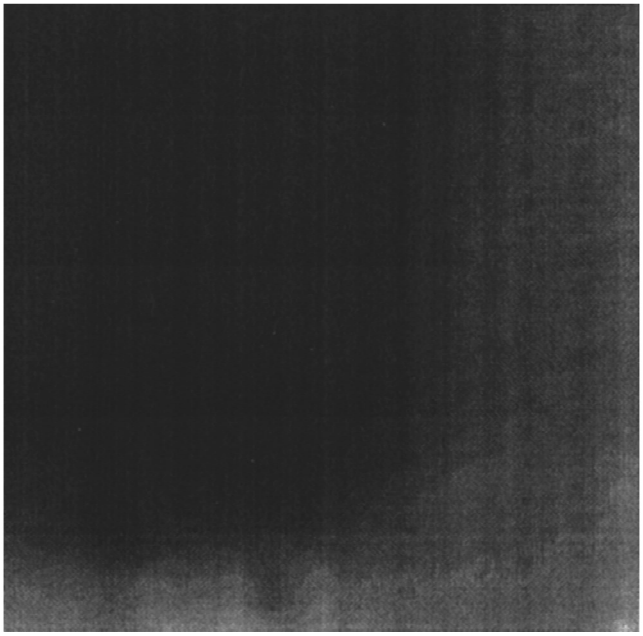

FIG. 2. Pattern of integrated photoluminescence intensity of InGaP/GaAs/InGaAs/GaAs/InGaP heterostructures at 300 K after part of the surface has been modified. The probe aperture ~1 μm and the frame size is 15×15 μm. The white color corresponds to the maximum photoluminescence intensity.

deposited a thin $\sim$20 nm layer containing a mixture of Cr and C atoms on the surface of the sample. This layer is a good conductor and transparent to the incident radiation. These impurities were chosen because Cr forms nonradiative recombination centers in GaAs. The experiments demonstrated that the incident radiation has a power density threshold above which the photoluminescence is quenched. According to our estimates, this threshold is $\sim10^5$ W/cm^2. Figure 2 shows the distribution of the photoluminescence intensity from the modified part of the surface. The size of the transition region of reduced photoluminescence intensity is ~2 μm, which is comparable with the value obtained in Ref. 2 for the etching boundary of a similar structure.

To conclude, we have obtained the pattern of integrated photoluminescence for InGaP/GaAs/InGaAs/GaAs/InGaP semiconducting laser heterostructures. Spatial nonuniformity of the photoluminescence intensity was observed in $\sim50\times50$ μm sections, probably caused by nonuniformity of the InGaP layer. This method may be used to diagnose the quality of luminescent heterostructures. It has been shown that the photoluminescence may be quenched by Cr diffusion stimulated by near-field laser radiation and this effect may be utilized to develop low-dimension objects with different optical properties.

The authors would like to thank B. N. Zvonkov and O. I. Khrykin for supplying the samples.

This work was supported financially by the Russian Fund for Fundamental Research (Grant No. 96–02–16990a) and by the ''Fundamental Metrology'' State Program (Grant No. 2.73).

[1] R. D. Grober, T. D. Harris, J. K. Trautman *et al.*, Appl. Phys. Lett. **64**, 1421 (1994).
[2] D. V. Kazantsev, N. A. Gippius, Zh. Oshinovo *et al.*, JETP Lett. **63** 550 (1996).
[3] M. J. Gregor, P. G. Blome, R. G. Ulbrich *et al.*, Appl. Phys. Lett. **67**, 3572 (1995).
[4] I. I. Smolyaninov, D. L. Mazzoni, and C. C. Davis, Appl. Phys. Lett. **67**, 3859 (1995).
[5] E. Betzig, J. K. Trautman, R. Wolfe *et al.*, Appl. Phys. Lett. **61**, 142 (1992).
[6] D. G. Volgunov, S. V. Gaponov, V. F. Dryakhlushin *et al.*, Prib. Tekh. Éksp. (in press).
[7] D. P. Bour, T. L. Paoli, R. L. Thornton *et al.*, Appl. Phys. Lett. **62**, 3458 (1993).
[8] V. Ya. Aleshkin, S. A. Akhlestina, B. N. Zvonkova *et al.*, Fiz. Tekh. Poluprovodn. **29**, 590 (1995) [Semiconductors **29**, 307 (1995)].
[9] A. Gomio, K. Kobayashi, S. Kawata *et al.*, J. Cryst. Growth **77**, 367 (1986).

Translated by R. M. Durham

Instability of a charged free surface of solutions of inactive substances

A. I. Grigor'ev, D. F. Belonozhko, and S. O. Shiryaeva

Yaroslavl' State University
(Submitted February 19, 1997)
Pis'ma Zh. Tekh. Fiz. **23**, 26–31 (August 26, 1997)

It is shown that the simultaneous buildup of instability of the free surface of a solution of an inactive substance in relation to its concentration and the Tonks–Frenkel instability, causes the branches of the dispersion equation describing each of these instabilities separately to close onto one another and form two new composite branches of unstable liquid motion. One of these branches has growth rates exceeding those made up of the initial instabilities separately. [S1063-7850(97)02208-8]

Inactive substances, which increase the surface tension of the liquid in which they are dissolved, may induce capillary wave instability at the surface of the solution. The interaction between this instability and the instability of the liquid surface in relation to its own charge or an induced charge (the Tonks–Frenkel instability) is of interest for numerous applications in technical physics, geophysics, and technology.

We shall calculate the spectrum of capillary motion in a viscous incompressible ideally conducting liquid of infinite depth, situated in a gravitational field **g** and in an electrostatic field **E** normal to the free surface. Let us assume that the liquid has the density ρ and kinematic viscosity ν, and that some surfactant with concentration C is dissolved in it. The surfactant will emerge onto the surface and be distributed in the unperturbed state with the surface concentration Γ_0. Let us assume that σ is the surface tension of the liquid surface in the presence of the surfactant, and μ_n and μ_p are the chemical potentials of the bulk and surface phases of the surfactant. We assume that the time taken for relaxation of the surfactant between the surface and the region of the bulk solution adjacent to the surface is shorter than the period $2\pi/\omega_0$ of the perturbation induced by a wave at the frequency ω_0. This implies that the surface and bulk phases of the solution are in a state of equilibrium. The electric field **E** at the surface is determined by the potential difference between the surface of the liquid maintained at the potential $\Phi_1=0$ ($z\to-\infty$) and a counterelectrode, parallel to the liquid surface at $z=b$, having the potential $\Phi_2=V$.

A Cartesian coordinate system is positioned such that the **z** axis is directed vertically upward $\mathbf{n}\|-\mathbf{g}$ ($\mathbf{n}_z$ is the unit vector of the Cartesian coordinate z) and the x axis lies in the direction of motion of a plane capillary wave $\sim\exp(st+ikx)$. It is assumed that the $z=0$ plane coincides with the free unperturbed surface of the liquid (s is the complex frequency, k is the wave number, t is the time, and i is the imaginary unit). The function $\xi(x,t)=\xi_0\exp(st+ilx)$ describes a small perturbation of an equilibrium flat liquid surface, induced by thermal capillary wave motion of extremely small amplitude, $\xi_0\sim(kT/\gamma)^{1/2}$, where k is the Boltzmann constant, T is the temperature, and $\mathbf{U}(\mathbf{r},t)$ is the velocity field of the liquid motion, induced by the perturbation $\xi(x,t)$, having the same order of smallness.

In dimensionless variables in which $g=\rho=\sigma=1$, the dispersion equation for the capillary motion of the liquid in our particular system is[1,2]

$$
\begin{aligned}
&-s^2(s+2\nu k^2)^2\{s+D_*k^2+L\sqrt{D(s+Dk^2)}\}\\
&+\omega_0^2\{\chi_0k^2s(k-\sqrt{k^2+s/\nu})-s^2\\
&\times(s+D_*k^*+L\sqrt{D(s+Dk^2)})\}\\
&+4\nu^2k^3s^2\{s+D_*k^2+L\sqrt{D(s+Dk^2)}\}\\
&\times\sqrt{k^2+3/\nu}-s^3\chi_0k^2\sqrt{k^2+s/\nu}=0;
\end{aligned}
\tag{1}
$$

$$
\omega_0^2=k^3+k-Wk^2\coth(kb);\quad \chi_0=\frac{\partial\sigma}{\partial\Gamma}\Gamma_0;
$$

$$
L=\left(\frac{\partial\mu_n}{\partial\Gamma_0}\right)/\left(\frac{\partial\mu_p}{\partial C_0}\right);\quad W=\frac{\varepsilon E_0^2}{4\pi};\quad E_0=V/b,
$$

where D_* is the surface diffusion coefficient of the surfactant and W characterizes the pressure of the electric field on the charged liquid surface, or equivalently, the surface charge density. The quantity χ_0 has the meaning of an elastic constant, and varies between -1 and $+1$. The range $\chi_0<0$ corresponds to the usual surfactants, which reduce the surface tension σ of the free liquid surface, while $\chi_0>0$ corresponds to inactive surfactants which increase σ; L has the meaning of the characteristic reciprocal linear length of variation of the volume concentration of surfactant near the surface: $L\sim(\sigma D^2/\rho g^3)^{-1/4}$.

It was shown in Ref. 2 that in a linear approximation in the small parameters U and ξ, the surface of the solution of an inactive substance (i.e. $\chi_0>0$) is unstable and the amplitudes of the thermal capillary waves increase exponentially with time, with a growth rate which increases with χ_0. The essence of the effect is that a reduction in the concentration of inactive substance lowers the surface tension, and the lower surface tension gives a larger free surface area of the solution. As the systems strives to attain a state with a lower surface energy, it increases its area, which causes a drop in the surface concentration of the inactive substance, i.e., the instability shows up as an increase in the surface area accompanied by a decrease in the surface concentration, and also in the parameter χ_0. Since the liquid is incompressible, the area

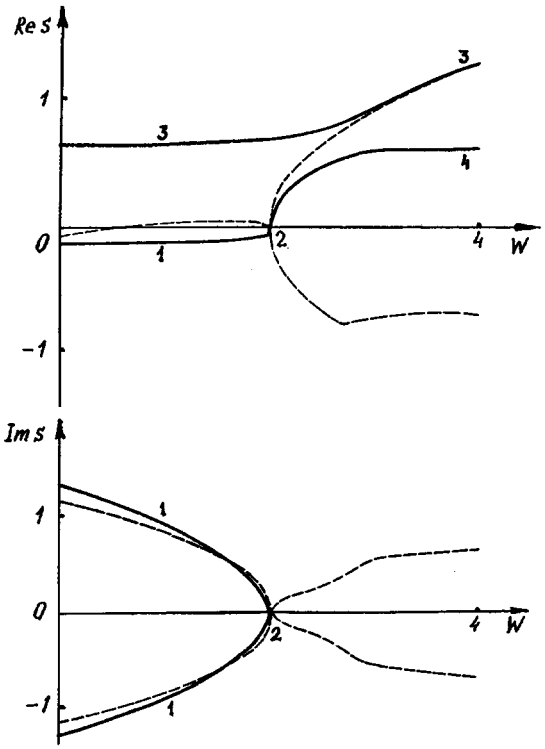

FIG. 1. Dependences of the real and imaginary parts of the dimensionless frequency on the dimensionless parameter W, characterizing the electric field pressure, $\mathrm{Res}=\mathrm{Res}(W)$ and $\mathrm{Ims}=\mathrm{Ims}(W)$, respectively, calculated for $k=1$, $\nu=0.1$, $L=500$, $D=3\times10^{-6}$, $D_*=3\times10^{-5}$, $\chi_0=0.5$, and $b=10$. The dashed curves give the unobservable branches lying on the lower sheet of the Riemann surface on which Eq. (1) was determined.

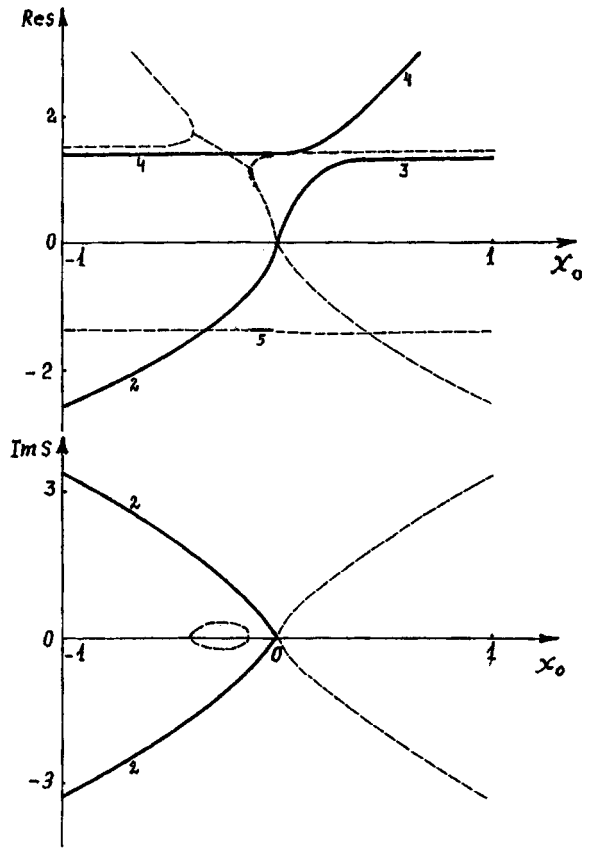

FIG. 2. Curves of $\mathrm{Res}=\mathrm{Res}(\chi_0)$ and $\mathrm{Ims}=\mathrm{Ims}(\chi_0)$ as functions of the dimensionless parameter χ_0 calculated for $k=1$, $\nu=0.01$, $L=500$, $D=10^{-6}$, $d_*=10^{-6}$, $W=2$, and $b=10$.

is increased by changing the relief of the free surface. This process will continue until the negative feedback between the surface and bulk phases of the inactive substance caused by diffusional exchange is unable to compensate for the changes in the surface concentration of the impurity (these are caused by the deformation of the free surface) in a time shorter than the characteristic time of the perturbation. In terms of linear theory in the small parameters, it is impossible to predict the amplitudes of the steady-state perturbations of the free surface associated with this effect, but since the variations in the coefficient of surface tension caused by local changes in the concentration of the inactive substance do not exceed a few tenths of the unperturbed value, we can expect the amplitudes of the thermal capillary waves to increase by approximately an order of magnitude — from a few angstroms to a few tens of angstroms. As a result of this instability, an irregular relief will form on the surface and a surface concentration $\chi_0=\chi_0(x)$ will be established, accompanied by periodic surface fluxes of inactive substance.

In addition to this instability, the Tonks–Frenkel instability[3] will also be established in the system for $W>2$. A detailed numerical analysis of the dispersion equation (1) shows that both these instabilities may interact, forming new composite instabilities, represented by branches *3* and *4* in Figs. 1 and 2. Branch *1* describes the capillary wave motion and branch *2* describes the wave motion associated with redistribution of the surfactant.

Figure 1 shows the dependences of the real and imaginary parts of the frequency on the dimensionless parameter W characterizing the surface charge density, $\mathrm{Re}\ s=\mathrm{Re}\ s(W)$ and $\mathrm{Im}\ s=\mathrm{Im}\ s(W)$, respectively. Figure 2 gives the dependences $\mathrm{Re}\ s=\mathrm{Re}\ s(\chi_0)$ and $\mathrm{Im}\ s=\mathrm{Im}\ s(\chi_0)$ on the dimensionless parameter χ_0 calculated numerically using Eq. (1). It is obvious that both dependences look qualitatively the same, although they have different arguments. Regardless of whether the initial instability is associated with the presence of an inactive substance in the solution ($\chi_0>0$) or with a high surface charge density ($W>2$), the increased influence of the second factors (W or χ_0, respectively) leads to an increase in the growth rate of the initial instability, whereas the growth rate of the second instability does not exceed that of the initial instability. When both instabilities build up simultaneously, the branches of the dispersion equation describing the Tonks–Frenkel instability and the capillary wave instability in the solution of an inactive substance are not independently realized close onto one another to form branches *3* and *4*.

[1] V. G. Levich, *Physicochemical Hydrodynamics* [in Russian], Fizmatgiz, Moscow (1959).
[2] D. F. Belonozhko, S. O. Shiryaeva, and A. I. Grigor'ev, Pis'ma Zh. Tekh. Fiz. **22**(15), 60 (1996) [Tech. Phys. Lett. **22** 626 (1996)].
[3] A. I. Grigor'ev, O. A. Grigor'ev, and S. O. Shiryaeva, Zh. Tekh. Fiz. **62**(9), 12 (1992) [Sov. Phys. Tech. Phys. **37**, 904 (1992)].

Translated by R. M. Durham

Influence of elasticity and dynamic surface tension on the wave motion spectrum of a charged liquid surface

S. O. Shiryaeva, A. I. Grigor'ev, and D. F. Belonozhko

Yaroslavl' State University
(Submitted February 19, 1997)
Pis'ma Zh. Tekh. Fiz. **23**, 32–37 (August 26, 1997)

It is shown that the combined influence of the relaxation of viscosity and surface tension on the position of the boundary of the capillary wave spectrum established in a system is not a simple summation of each effect separately because of the nonlinearity of the dispersion equation in the corresponding physical parameters.
[S1063-7850(97)02308-2]

The phenomenon of instability of a charged liquid surface plays an important role in various technical and technological devices.[1] Nevertheless, some aspects of the effect have not yet been studied. This particularly applies to the influence of relaxation processes on the capillary wave motion at a charged liquid surface, although the important part played by relaxation of viscosity and surface tension in the formation of the wave spectrum was indicated quite some time ago.[2] It was shown in Refs. 3 and 4 that relaxation of viscosity and surface tension at the interface between an electrically conducting liquid and a dielectric medium have very little influence on the buildup of instability of a charged liquid surface: they do not affect the critical conditions, and alter the instability growth rate only very slightly. In this context, we propose to study the interaction between the relaxation of viscosity and surface tension and its influence on the structure of the wave motion spectrum of the liquid.

Let us assume that an unbounded flat surface of a viscous, incompressible, ideally conducting liquid, uniformly charged with the surface charge density $\varkappa$, fills the half-space $z<0$ in a gravitational field ($\mathbf{n}_z \| -\mathbf{g}$, where $\mathbf{n}_z$ is the unit vector of the z Cartesian coordinate and $\mathbf{g}$ is the acceleration due to gravity) and is bounded by vacuum at $z=0$. The equation for the boundary surface in the absence of any perturbation is written as $z=0$. Let us take σ and ν to be the surface tension and the kinematic viscosity of the liquid, respectively, and ρ its density.

A detailed derivation of the dispersion equation for capillary waves on a flat surface of viscous liquid in the absence of any surface charge was given in Ref. 5. Repeating the same reasoning as in Ref. 5 except that the dynamic boundary condition for the normal component of the stress tensor now also includes a term for the electric field pressure that also takes into account the contribution made by the deformation of the uniform distribution of the electric charge over the liquid surface (caused by the capillary wave motion of the free surface),[6,7] it is easy to obtain the dispersion equation for the capillary motion of a charged liquid surface:

$$\omega^2+4i\nu k^2\omega-4\nu^2k^4\left(1-\sqrt{1-\frac{i\omega}{\nu k^2}}\right)=\frac{k}{\rho}(g\rho+\sigma k^2-4\pi k\varkappa^2), \tag{1}$$

where ω is the complex frequency in the time dependence of the thermal capillary wave amplitudes: $\xi\sim\exp(-i\omega t)$, k is the wave number, and i is the imaginary unit. The imaginary negative part of the complex frequency gives the damping rate of the capillary waves and the imaginary positive part gives the growth rate of the Tonks–Frenkel instability, which is established when the right-hand side of relation (1) (with increasing surface electric charge density) passes through zero and becomes negative. The real part of the complex frequency in this expression gives the frequency of the wave motion.

In the most general situation, the viscosity and surface tension are functions of frequency[2] which, within the framework of an idealized model of a continuous medium, is equivalent to allowance for the real molecular structure of the liquid, characterized by specific rates of transfer of intermolecular interaction, momentum transport, and by the presence of some ordering of the liquid structure in the surface layer of its interface with other media:

$$\sigma=\sigma_\infty-\sigma_*(1-i\omega\tau_s)^{-1}=\sigma_0-i\omega\tau_s\sigma_*/1-i\omega\tau_s,$$
$$\sigma_*=\sigma_\infty-\sigma_0, \quad \nu=\nu_0(1-i\omega\tau_v)^{-1}, \tag{2}$$

where ν_0 and σ_0 are the viscosity and surface tension at zero frequency, σ_∞ is the surface tension at high frequencies (where $\omega\tau_s\gg1$), and τ_v and τ_s are the characteristic viscosity and surface tension relaxation times.

Substituting Eq. (2) into Eq. (1), we obtain the dispersion equation for the capillary motion of a liquid with a charged free surface in a plane half-space allowing for the relaxation of viscosity and surface tension. In terms of dimensionless variables, this equation has the form:

$$(1-i\gamma y)[2-i\gamma y(1-i\delta y)]^2+\alpha^2(1-i\gamma y)(1-i\delta y)^2-if\gamma y(1-i\delta y)^2=4(1-i\gamma y)\sqrt{1-iy(1-i\delta y)}; \tag{3}$$

$$y=\frac{\omega}{\nu_0k^2}; \quad \alpha=\frac{\omega_0}{\nu_0k^2}; \quad \omega_0^2=\frac{k}{\rho}(g\rho+\sigma k^2-4\pi k\varkappa^2);$$
$$f=\sigma_*/\rho\nu^2k; \quad \delta=\nu_0k^2\tau_v; \quad \gamma=\nu_0k^2\tau_s.$$

It is easy to see that the physical parameters determining the relaxation effects (γ and δ) appear in the dispersion equation (3) in multiplicative and nonlinear form, and consequently, the result of their combined influence on the

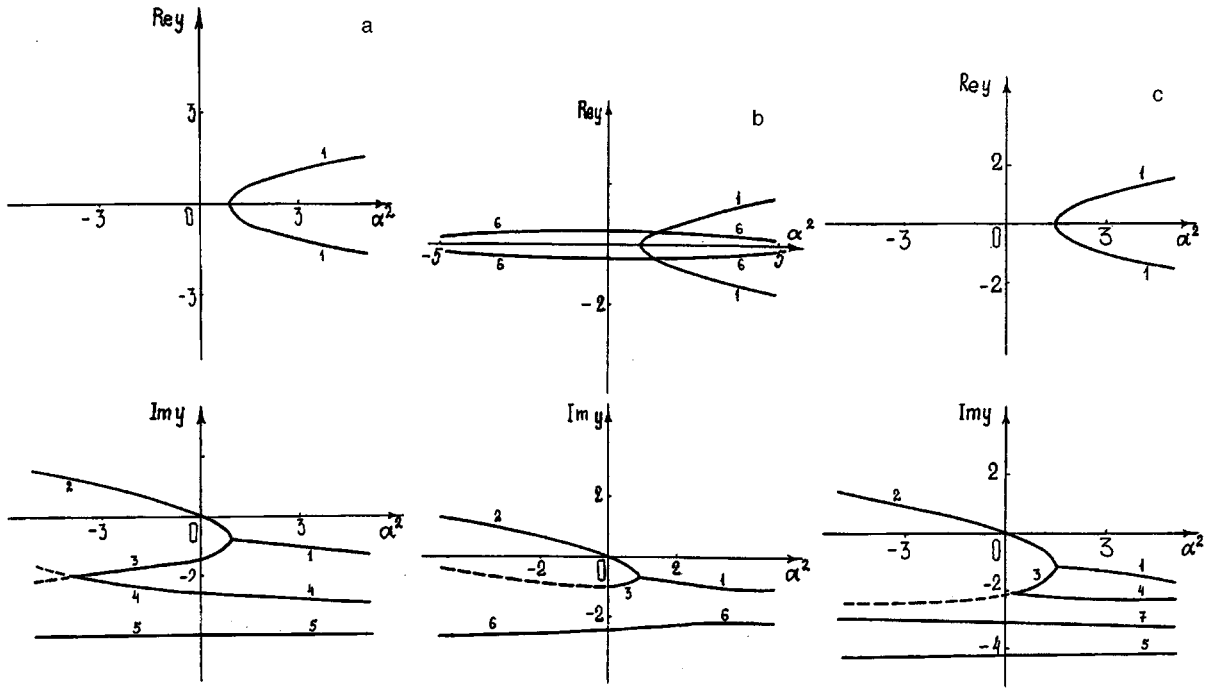

FIG. 1. Real Re $y=\mathrm{Re}\, y(\alpha^2)$ and imaginary Im $y=\mathrm{Im}\, y(\alpha^2)$ parts of the dimensionless frequency plotted as functions of the parameter α^2 characterizing the dividing balance on the free liquid surface for: a — $\gamma=0$, $\delta=0.25$; b — $f=1$, $\gamma=0.4$, $\delta=0$; and c — $f=1$, $\gamma=0.4$, $\delta=0.25$.

physical characteristics of the capillary liquid motion is not obvious. According to Refs. 3 and 4, the most important aspect of the influence of these relaxation effects is the high-wave-number limit imposed on the capillary wave spectrum. We therefore examine how the relaxation of the viscosity and surface tension influence the upper wave number limit for the thermal capillary waves separately and jointly.

Figure 1 gives the results of numerical calculations using Eq. (3) for $\gamma=0$, $\delta=0.25$ (Fig. 1a), $f=1$, $\gamma=0.4$, and $\delta=0$ (Fig. 1b), and $f=1$, $\gamma=0.4$, and $\delta=0.25$ (Fig. 1c). The dashed curves give the continuations of the realized branches of the dispersion equation, which go over to the lower sheets of the two-sheet Riemann surface on which the dispersion equation (3) was determined.

Branches *1*, *2*, and *3* correspond to capillary liquid motion induced by the thermal motion of the molecules and by surface tension, while branches numbered above 3 are generated by the action of viscosity and surface tension relaxation effects (for further details see Refs. 3 and 4).

It is easy to see that allowance for these relaxation effects produces a considerably more complex spectrum of capillary liquid motion. The numerical calculations show that interaction between viscosity relaxation and surface tension relaxation leads to deformation of the spectrum obtained by simply summing the new branches of the dispersion equation associated with each of these effects separately. For instance, the region of existence of the relaxation wave motion (branch *6*) in Fig. 1b, whose appearance is ascribed to relaxation of the surface tension, is contracted as the parameter δ increases from zero, and for $\delta=0.216$ the branch disappears completely.

It was shown in Ref. 8 that the maximum k (or equivalently, the minimum wavelength $\lambda=\lambda_{\min}$) for the capillary waves established in the system may be determined from the abscissa of the point of intersection of branches *1*, *2*, and *3*.

Denoting by $\alpha^2=C$ the abscissa of the point where branches *1*, *2*, and *3* diverge, the relation

$$\alpha^2=\frac{1}{\rho\gamma^2}\left(\frac{\sigma_0}{k}-\frac{4\pi\varkappa^2}{k^2}\right)=\frac{\sigma_0}{2\pi\rho\nu^2}\left(\lambda-\frac{2\varkappa^2}{\sigma_0}\lambda^2\right)=C$$

can then be used to find the minimum capillary wavelength in the system (which is not suppressed by viscosity or relaxation effects):

$$\lambda_{\min}\approx 2\pi\frac{\rho\nu^2 C}{\sigma_0}\left(1+\frac{\rho\nu^2 C}{\sigma_0}\,\frac{4\pi\varkappa^2}{\sigma_0}\right).$$

Confirmation of this reasoning comes from the specific example of water. According to data presented in Ref. 4, in the absence of relaxation effects for $\varkappa=0$, we have $C\approx 0.58$, which corresponds to $\lambda_{\min}\approx 0.05$ μm = 50 nm. From Fig. 1a for $\gamma=0$ it is easy to find $C\approx 0.91$, which gives $\lambda_{\min}\approx 78$ nm for $\varkappa=0$. Figure 1b for $\delta=0$ gives $C\approx 0.86$ and $\lambda_{\min}\approx 74$ nm for $\varkappa=0$. Finally, Fig. 1c for $\gamma=0.4$, $\delta=0.25$ gives $C\approx 1.47$ and $\lambda_{\min}\approx 127$ nm for $\varkappa=0$. For $\varkappa\approx 0.5\varkappa_*$ ($\varkappa_*$ is the critical surface charge density for the onset of Tonks–Frenkel instability), the values of $\lambda_{\min}$ are doubled. It is easy to see that when both these relaxation effects act jointly, their combined quenching influence on the capillary waves is nonadditive.

[1] A. I. Grigor'ev, and S. O. Shiryaeva, Izv. Ross. Akad. Nauk Ser. Mekh. Zhidk. Gaza. No. 3, 3 (1994).
[2] Yu. A. Bykovskiĭ, É. A. Manykin, P. P. Poluéktov *et al.*, Zh. Tekh. Fiz. **46**, 2211 (1976) [Sov. Phys. Tech. Phys. **21**, 1302 (1976)].
[3] S. O. Shiryaeva, O. A. Grigor'ev, and A. I. Grigor'ev, Zh. Tekh. Fiz. **66**(10), 31 (1996) [Tech. Phys. **41**, 989 (1996)].

[4] S. O. Shiryaeva, O. A. Grigor'ev, M. I. Munichev, and A. I. Grigor'ev, Zh. Tekh. Fiz. **66**(10), 47 (1996) [Tech. Phys. **41**, 997 (1996)].
[5] V. G. Levich, *Physicochemical Hydrodynamics* [in Russian], Fizmatgiz, Moscow (1959).
[6] I. N. Aliev and A. V. Filippov, MG No. 4, 94 (1989).
[7] A. I. Grigor'ev, O. A. Grigor'ev, and S. O. Shiryaeva, Zh. Tekh. Fiz. **62**(9), 12 (1992) [Sov. Phys. Tech. Phys. **37**, 904 (1992)].
[8] P. N. Antonyuk, Dokl. Akad. Nauk SSSR **286**, 1324 (1986) [Sov. Phys. Dokl. **31**, 102 (1986)].

Translated by R. M. Durham

Instability growth rate of a charged interface between immiscible electrically conducting liquids

A. I. Grigor'ev, D. F. Belonozhko, S. O. Shiryaeva, and S. I. Shchukin

Yaroslavl' State University
(Submitted April 2, 1997)
Pis'ma Zh. Tekh. Fiz. **23**, 38–40 (August 26, 1997)

It is shown by means of a numerical analysis of the dispersion equation that two types of aperiodic instability may occur at a charged planar interface between two viscous incompressible immiscible electrically conducting liquids, for which the growth rates increase or decrease, respectively as the conductivity ratio of the media increases. © *1997 American Institute of Physics.* [S1063-7850(97)02408-7]

The problem of the stability of the interface between two immiscible liquids having different physicochemical characteristics has frequently been solved in various limiting situations in connection with numerous applications in physics, engineering, and technology (see, for example, reviews presented in Refs. 1–3). Nevertheless, some related aspects have not yet been fully clarified. This particularly applies to studies of the characteristics features of the onset of instability of a charged liquid interface.

The following analysis is made using a model of incompressible viscous conducting liquids filling all of space in a gravitational field. Let us suppose that the unperturbed interface between the liquids coincides with the XY plane in a Cartesian coordinate system whose Z axis is directed upward in the opposite direction to the force of the gravitational field. Let us assume that the upper liquid having the kinematic viscosity ν_1, density ρ_1, and filling the half-space $z>0$, is electrically conducting with conductivity σ_1 and permittivity ε_1. The lower liquid fills the half-space $z<0$ and has the kinematic viscosity ν_2, density ρ_2, permittivity ε_2, and conductivity σ_2. We also assume that the unperturbed interface between the liquids is uniformly charged with a surface charge density ε and has a surface tension γ. The electrostatic fields in the upper and lower regions will be denoted by E_1 and E_2, respectively.

The dispersion relation for the capillary liquid motion in this system was derived in Ref. 4. In dimensionless variables, where $g=\rho_2=\gamma=1$, this has the form:

$$
\begin{aligned}
&-\alpha^2(s^2(1+s\beta)n+sk\Theta d)-sk^3H\lambda\\
&+(1+s\beta)^2(s^4(\rho+1)n-4s^2k^3\nu^2(\rho-1)^2d\\
&+4s^3k^2\nu(\rho-1)m+4\rho s^4k)\\
&+(1+s\beta)(s^3k^2\theta n+s^3k\theta(\rho+1)d\\
&+k(H+\Lambda s^2)(sm-2sk^2\theta\nu(\rho-1)d)=0, \qquad (1)
\end{aligned}
$$

where

$$
\begin{aligned}
&n=\rho(\sqrt{k^2+s/\nu_2}-k)+(\sqrt{k^2+s/\nu_1}-k),\\
&m=\rho(\sqrt{k^2+s/\nu_2}-k)-(\sqrt{k^2+s/\nu_1}-k),\\
&d=(\sqrt{k^2+s/\nu_1}-k)(\sqrt{k^2+s/\nu_1}-k),
\end{aligned}
$$

$$
\begin{aligned}
&\sigma=\frac{\sigma_1}{\sigma_2}\varepsilon=\frac{\varepsilon_1}{\varepsilon_2}\beta=\frac{\varepsilon_1+\varepsilon_2}{4\pi(\sigma_1+\sigma_2)}, \quad \rho=\rho_1,\\
&\alpha^2=(1+s\beta)(k(\rho-1)-k^3)+k^2F,\\
&F=W(1-\sigma)\left(s\beta\frac{1-\sigma}{1+\varepsilon}+\frac{1+\varepsilon\sigma^2}{1+\sigma}\right),\\
&H=W(1-\varepsilon\sigma)\left(s\beta\left[1-\frac{1-\sigma}{1+\varepsilon}\right]+\frac{2\sigma}{1+\sigma}\right),\\
&W=\frac{\varepsilon_1E_{10}^2}{4\pi}, \quad \Theta=W(1-\varepsilon\sigma)\beta\left(1-\frac{1+\sigma}{1+\varepsilon}\right),\\
&\Lambda=W(1-\varepsilon\sigma)\beta\left(1-\frac{1-\sigma}{1+\varepsilon}\right).
\end{aligned}
$$

Numerical calculations made using the dispersion equation (1) are plotted in Fig. 1 which gives the positive real component of the frequency Re s versus the ratio of the conductivities of the upper σ_1 and lower σ_2 liquids, Re $s(\sigma_1/\sigma_2)$. Both branches in the figure describe aperiodic instabilities of the Tonks–Frenkel type but behave differently with increasing σ_1/σ_2: branch *1* decays with increasing σ_1/σ_2 whereas branch *2* increases.

It should be noted that branch *1* begins on one axis of the coordinate system and ends on another. Branch *2* appears

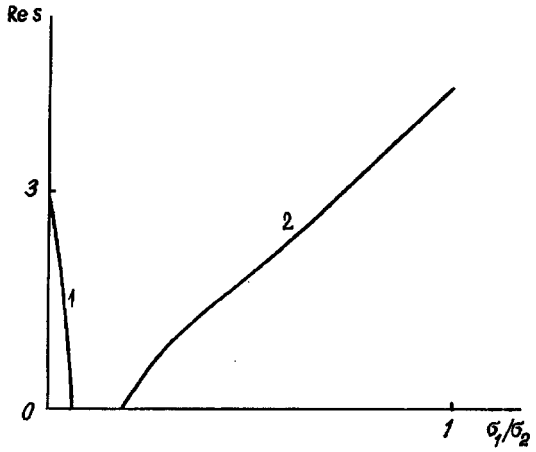

FIG. 1. Real part of the complex frequency, Re s, as a function of the ratio of the conductivities of the upper σ_1 and lower σ_2 liquids, Re $s(\sigma_1/\sigma_2)$, for $k=1$, $\nu=0.1$, $\varepsilon=0.1$, $\rho=0.01$, $\beta=0.01$, and $W=2.15$.

 1063-7850/97/080631-02$10.00

from the lower sheet of the two-sheet Riemann surface on which the dispersion relation (1) was determined in the region $\mathrm{Re}\, s<0$ and then goes over to the region $\mathrm{Re}\, s>0$.

[1] V. I. Kozhenkov and N. A. Fuks, Usp. Khim. **45**, 2274 (1976).
[2] A. G. Bailey, Atomisation Spray Technol. **2**, 95 (1986).
[3] A. I. Grigor'ev and S. O. Shiryaeva, Izv. Ross. Akad. Nauk Ser. Mekh. Zhidk. Gaza. No. 3, 3 (1994).
[4] J. R. Melcher and W. J. Schwarz, Phys. Fluids **11**, 2604 (1968).

Translated by R. M. Durham

Oscillatory instability of the interface between conducting liquids in a normal electric field

V. A. Saranin, A. N. Zharov, and D. F. Belonozhko

P. G. Demidov State University, Yaroslavl'
(Submitted February 18, 1997)
Pis'ma Zh. Tekh. Fiz. **23**, 41–44 (August 26, 1997)

It is shown that a new type of oscillatory instability, unlike the Tonks–Frenkel instability, may occur at a charged interface between two electrically conducting liquids in a perpendicular electrostatic field. © *1997 American Institute of Physics.* [S1063-7850(97)02508-1]

Studies of the stability of a charged flat liquid surface in relation to its own charges and induced charges are of considerable interest for numerous technical and technological applications.[1] However, there are many unresolved problems associated with the need to allow for relaxation processes in the liquid. In particular, the influence of the finite electrical conductivity of a real liquid on the characteristic features of the instability buildup in a charged liquid surface has not been studied sufficiently comprehensively.

The investigation reported in this article concerns the possible onset of oscillatory instability of the interface between two electrically conducting liquids in an electrostatic field normal to the interface, which may occur at a lower electric field strength than the Tonks–Frenkel instability.

1. Let us consider two immiscible conducting liquids filling the space between the plates of a plane-parallel capacitor and situated in a normal electric field. We select a Cartesian coordinate system x, y, z with the z axis directed vertically upward. Thus the equation for the unperturbed surface is $z=0$. We shall assume that the liquids have different densities where $\rho_2 \gg \rho_1$ but the same kinematic viscosities $\nu_1=\nu_2\equiv\nu$, where the subscripts 1 and 2 refer to the upper and lower liquids, respectively. We shall denote the surface tension of the interface by α. The liquids are situated in external constant uniform electrostatic fields $\mathbf{E}_{02}$ and $\mathbf{E}_{01}$, and also in a gravitational field $\mathbf{g}$.

It was shown in Ref. 2 that the dispersion equation for this system, cast in dimensionless form is:

$$(s^2L+\Omega_0^2L+B_1\Phi Lk^2(n_1-1)+s^2)$$
$$\times\left(s+\Theta B_1Lk^2\left(\frac{n_1}{n_2}-1\right)\right)-\left(B_1k^2\Psi L\left(\frac{n_1}{n_2}-1\right)\frac{1-n_3}{1+n_3}\right.$$
$$\left.+2\mu k^2sL\left(\frac{1-n_3}{1+n_3}\right)^2-s^2\left(\frac{1-n_3}{1+n_3}\right)^2\right)$$
$$\times\left(-s+2\mu k^2L+B_1k^2\Theta\left(\frac{n_1+n_2}{n_2}\right)\left(\frac{1+n_3}{1-n_3}\right)L\right)=0; \quad (1)$$

$$k_m=\left(\frac{g(\rho_2-\rho_1)}{\alpha}\right)^{1/2}; \quad \Omega_m=\left(\frac{\alpha k_m^3}{(\rho_2+\rho_1)}\right)^{1/2};$$

$$L=\left(1+\frac{s}{\mu k^2}\right)^{1/2}-1; \quad \mu=\frac{\nu k_m^2}{\Omega_m}; \quad n_1=\frac{\sigma_2}{\sigma_1}; \quad n_2=\frac{\varepsilon 2}{\varepsilon_1};$$

$$n_3=\frac{\rho_2}{\rho_1}; \quad B_1=\frac{\varepsilon_1E_{10}^2k_m^2n_2}{(\rho_1+\rho_2)\Omega_m^2n_1^2}; \quad \beta=\frac{\sigma_1+\sigma_2}{(\varepsilon_1+\varepsilon_2)\Omega_m};$$

$$\Phi=\frac{(1-n_1)s+\beta_1-\beta_2n_1}{(1+n_2)(\beta+s)};$$

$$\Psi=\frac{s(n_1+n_2)(1+n_1)+2\beta n_1(1+n_2)}{(1+n_1)(1+n_2)(\beta+s)};$$

$$\Theta=\frac{(n_1-n_2)}{(1+n_2)(\beta+s)}; \quad \beta=\beta\frac{(1+n_2)}{(1+n_1)};$$

$$\beta_2=\beta\frac{n_1(1+n_2)}{n_2(1+n_1)}; \quad \Omega_0=(k+k^3)^{1/2},$$

where s is the dimensionless frequency, k is the dimensionless wave number, i is the imaginary unit, σ_1 and σ_2 are the electrical conductivities of the liquids, and ε_1 and ε_2 are the permittivities.

For some values of the physical quantities, Eq. (1) contains the small parameter μ which has the meaning of the dimensionless viscosity. For instance, if we take $\rho_2=10^3$ kg/m^3, $\alpha=2\times10^{-2}$ N/m, and $\nu=10^{-6}$ m^2/s, we obtain $\mu\approx10^{-3}\ll1$.

2. The critical field strength, characterized by the parameter B_1, and the frequency of the unknown wave motion s will be sought as expansions in the small parameter μ:

$$B_1=b_0\mu+b_1\mu^2+\ldots; \quad (2)$$

$$s=i\Omega+(\omega_{r0}+i\omega_{i0})\mu+(\omega_{r1}+i\omega_{i1})\mu^2\ldots \quad (3)$$

Here b_0, b_1, ω_{r0}, ω_{i0}, ω_{r1}, and ω_{i1} are real numbers.

Substituting expressions (2) and (3) into the dispersion equation (1), we can determine the coefficients of the expansion. In the zeroth-order approximation with respect to μ, we find $s=i\Omega=i(k+k^3)^{1/2}$. In the first order in μ, we can derive equations linking the coefficients b_0, ω_{r0}, and ω_{i0}:

$$\omega_{i0}=\frac{k^2b_0}{2\Omega_0(\beta^2+\Omega_0^2)}\left\{\beta\left(\Phi_0-\frac{n_1-n_2}{n_2}\Psi_0\right)\right.$$
$$\left.-\Omega_0^2\left(2\Theta_0+\frac{n_1-n_2}{n_2}\Psi_1-\Phi_1\right)\right\};$$

$$\omega_{r0}=\frac{k^2b_0}{2(\beta^2+\Omega_0^2)}\left\{\beta\left(2\Theta_0+\frac{n_1-n_2}{n_2}\Psi_1-\Phi_1\right)\right.$$

 1063-7850/97/080633-02$10.00

$$+\left(\Phi_0-\frac{n_1-n_2}{n_2}\Psi_0\right)\Bigg\}-2k^2; \tag{4}$$

$$\Phi_0=-\frac{(n_1-1)^2}{n_2+1};\quad \Phi_1=\frac{(\beta_1-\beta_2 n_1)(n_1-1)}{n_2+1};$$

$$\Psi_0=\frac{n_1+n_2}{n_2+1};\psi\quad{}_1=\frac{2\beta n_1}{n_1+1};\quad \Theta_0=\frac{n_1-n_2}{n_2+1}.$$

It follows from Eq. (3) that if $\omega_{ro}>0$, the interface between the media exhibits unstable oscillatory motion which increases exponentially with time. According to Eq. (4), the condition for the onset of this instability has the form:

$$b_0>4(\beta^2+\Omega_0^2)\Bigg\{\beta\left(2\Theta_0+\frac{n_1-n_2}{n_2}\Psi_1-\Phi_1\right)$$
$$+\left(\Phi_0-\frac{n_1-n_2}{n_2}\Psi_0\right)\Bigg\}^{-1};$$

For $\beta=1$ this condition can be simplified substantially:

$$b_0>(1+\Omega_0^2)\frac{(n_1+1)(n_2+1)}{n_1(n_1-n_2)}. \tag{5}$$

It can be seen from condition (5) that oscillatory instability may develop when the condition $\sigma_2/\sigma_1>\varepsilon_2/\varepsilon_1$ is satisfied. If we take $n_1=2$, $n_s=1$, $\beta=1$, $\mu=10^{-3}$, and $k=10^{-2}$, oscillatory instability will develop in this system for $B_1=3\times10^{-3}$, whereas the Tonks–Frenkel instability is only established for $B_1=20$. Thus, for these parameters of the system, an oscillatory instability may develop at much lower values of the external electric field compared with the Tonks–Frenkel instability.

[1] A. I. Grigor'ev and S. O. Shiryaeva, Izv. Ross. Akad. Nauk Ser. Mekh. Zhidk. Gaza. No. 4, 3 (1994).
[2] J. R. Melcher and C. V. Smith, Phys. Fluids **12**, 778 (1969).

Translated by R. M. Durham

Reflection of light by domain walls in the uniaxial ferroelectric $Sn_2P_2S_6$

A. A. Grabar

(Submitted February 12, 1997)
Pis'ma Zh. Tekh. Fiz. **23**, 45–50 (August 26, 1997)

The occurrence of light scattering during light transmission is described for some orientations of an incident laser beam in polydomain crystals of the uniaxial ferroelectric tin thiohypodiphosphate. This scattering is probably caused by the presence of a reflecting layer near the 180° domain walls. A reflecting layer may be formed as a result of the appearance of charged nonparallel domain walls. © *1997 American Institute of Physics.*
[S1063-7850(97)02608-6]

The shape and orientation of the wall between ferroelectric domains is determined by the conditions for minimization of its elastic and electrostatic energy. In uniaxial ferroelectrics (i.e., those having a single direction of spontaneous polarization P_s and only antiparallel domains), walls parallel to the spontaneous polarization vector are energetically more favorable. The equilibrium thickness of the domain wall, defined as the region where the order parameter varies between $-P_s$ and $+P_s$, is of the order of a few crystal lattice constants.[1] This distance is two or three orders of magnitude less the wavelength of light λ. For this reason, a polydomain uniaxial ferroelectric is conventionally assumed to be an optically homogeneous medium (in terms of the linear refractive index).

It is known[2,3] that nonparallel domain walls or even domain walls perpendicular to P_s (opposed domains) may exist in crystals exhibiting fairly high conductivity because of screening by mobile charge carriers. The density of the corresponding surface charge is $\sigma=2|P_s|\cos\varphi$, where φ is the angle between the vector P_s and the normal to the domain wall. This screening charge is localized within layer whose thickness is of the order of the Debye screening length l_D. The nonuniform charge in this region creates electric fields which then cause local changes in the refractive index as a result of the electrooptic effect. In crystals with high values of P_s, $\cos\varphi$, conductivity, and electrooptic coefficients r_{ij}, this change and the layer thickness may be sufficient for reflection, scattering, or diffraction of light depending on the domain wall configuration. The directional light scattering effect described below may be explained as one manifestation of this screening of opposed domains.

Single crystals of tin thiohypodiphosphate were studied. These are uniaxial ferroelectric semiconductors belonging to the monoclinic system (class m) with a second-order phase transition $P2_1/n-P_n$ at $T_c=337$ K (Ref. 4). The samples were prepared by chemical transport reactions. This crystal is transparent in the 530–800 nm wavelength range and its optical properties were investigated previously in Ref. 5. To describe the orientation we used the system that characterizes these crystals,[6] where the X axis is parallel to the [100] crystallographic direction close to P_s and the Y axis is normal to the plane of symmetry m.

When studying the transmission of focused laser radiation through $Sn_2P_2S_6$ samples, we observed that the brightness of the light track inside the crystal was enhanced appreciably for certain orientations of the incident beam relative to the crystallographic axes and for an observation angle about 90° relative to the direction of the beam. This effect is not caused by defects since it is observed in all samples, including the most optically perfect ones.

Figures 1 and 2 show photographs (negatives) of $Sn_2P_2S_6$ samples, obtained when they were exposed to radiation from an LGN-215 He–Ne laser with a power around 40 mW. The dimensions of the sample were $5\times7\times4$ mm along the X, Y, and Z axes, respectively. In the photographs, the beam is incident on the surface parallel to (010) and scattering is observed through the (001) face. The laser radiation was focused by a spherical lens with focal length $f=500$ mm (Fig. 1) and by a cylindrical lens with $f=100$ mm (Fig. 2). Qualitatively, the images have the following characteristic features.

1. Scattering is only observed in polydomain samples. The effect is not observed in a single-domain sample, but is restored after the sample has been converted to the polydomain state by annealing.

2. The effect is only observed for certain specific relative orientations of the light beam and the observation point. These directions always form a large angle with the polar axis X and the effect is not observed if the incident beam or the direction of observation are close to this axis. The pattern is also observed if the direction of the light beam and the direction of observation are interchanged. When the crystal is rotated about the direction of observation, the ''blaze'' angle changes. In this case, the aperture of the scattering angle in the plane perpendicular to the incident beam is fairly small (a few degrees) and is tens of degrees in its plane of propagation.

3. If the sample is polarized such that part of the bulk is in the single-domain state, the scattering track is only observed in the unpolarized region (Fig. 1). On the whole the track is nonuniform and as the sample is displaced, scattering (luminous) and nonscattering (dark) regions are observed, most frequently resembling bands. When the sample is illuminated by a broad beam (Fig. 2), a parquet-like structure is clearly visible with bands positioned at a large angle to the polar direction.

4. When the crystal is heated to the phase transition temperature, the scattering intensity gradually decreases and al-

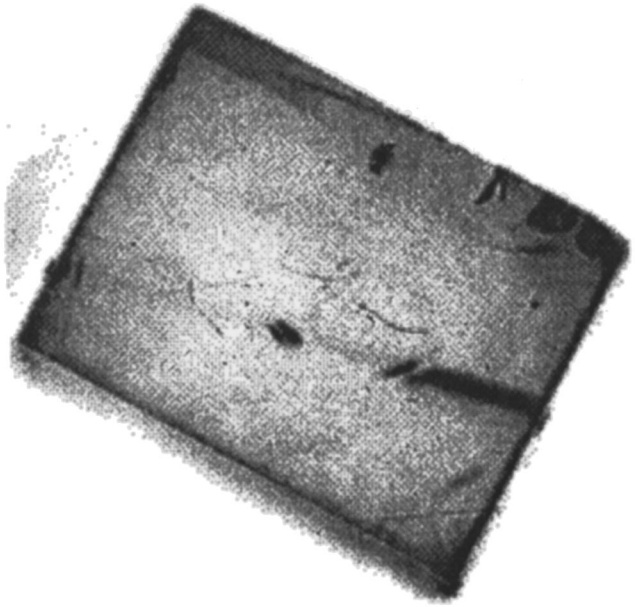

FIG. 1. Scattering of a helium–neon laser light beam focused by a spherical lens in a partially polarized $Sn_2P_2S_6$ sample (negative). A scattering track is observed in the polydomain region. The incident beam passes across the (010) face and observations are made perpendicular to (001).

most disappears 5–10 K before the transition is reached. No scattering is observed in the paraelectric phase. As the temperature is reduced and the sample returns to the ferroelectric phase, the scattering pattern is restored.

5. When the sample is switched by an external electrostatic field (up to 500 V/cm), various sections of the track inside the crystal are observed to switch on and off (total switching of the illuminated sample requires the application of a field above the breakdown value).

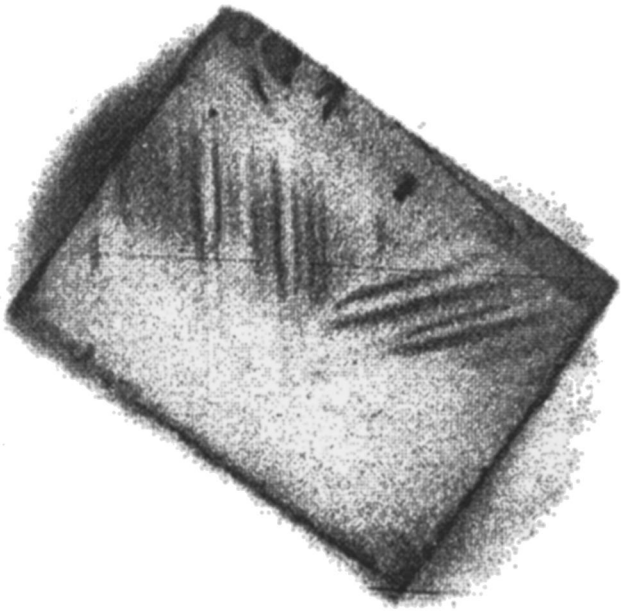

FIG. 2. Scattering pattern of a helium–neon laser light beam focused by a cylindrical lens in a polydomain $Sn_2P_2S_6$ sample. The orientation is the same as in Fig. 1.

The most probable cause of this scattering is the existence of a reflecting layer near the 180° domain walls. An analysis of the electric field distribution in the surface screening layer of the ferroelectric was reported in Ref. 2, where an estimated voltage drop $U \approx 1$ V for $l_D \approx 10^{-2}$ cm was obtained for ferroelectric semiconductors (SbSI, $BaTiO_3$). The electric field may reach 10^4–10^6 V/cm. Parameters similar to those of SbSI are obtained for $Sn_2P_2S_6$ at room temperature ($P_s = 15$ mC/cm^2, permittivity $\varepsilon_{11} = 200$–250 (Refs. 4 and 6), and conductivity $\sim 10^{-10}$ S/cm; Ref. 7). Taking the field strength in the screening layer as $E \sim 10^6$ V/cm, for the effective electrooptic coefficient $r_{\text{eff}} = 70$ pm/V and a refractive index $n \approx 3.0$ (at $\lambda = 632.8$ nm) (Ref. 5), the induced change in the refractive index may be $\delta n = n^3 r_{\text{eff}} E/2 \approx 10^{-3}$, which corresponds to the reflection coefficient $R = (\delta n/2n)^2 \approx 3 \times 10^{-8}$ for normal incidence. For the average equilibrium domain width of the order of 50 μm (Ref. 8), the net reflection coefficient per cm of the beam path may be of the order of 10^{-6}–10^{-5}. Similar effects near the walls of opposed domains may be caused by other phenomena. According to Ref. 9 for instance, regions of varying refractive index around 1 μm thick are formed in rapidly cooled high-resistivity $LiNbO_3$. These regions are induced by an explosive charge and can be observed in transmitted light by a polarizing microscope.

To conclude, the observed directional scattering effect is probably caused by reflection of the light wave by charged domain walls, which can only occur when these crystals contain domain walls nonparallel to the spontaneous polarization axis. This hypothesis contradicts the earlier conclusion[8] that $Sn_2P_2S_6$ has equilibrium domains in the form of cylinders elongated along P_s. The conclusions drawn in Ref. 8 were based on observations of domains at the surface of a sample using the liquid crystal method, whereas the pattern in the bulk may be more complex. The results obtained by studying the bulk distribution of P_s by a holographic method[10] agree qualitatively with the hypothesis of domain walls nonparallel to P_s. A more detailed study of directional light scattering in samples with different crystallographic orientation may provide additional information on the domain wall configuration.

This effect can be used to propose a new method of studying the domain structure of uniaxial ferroelectrics such as $Sn_2P_2S_6$, it can provide a very simple and convenient method of testing the degree of unipolarity of the samples, and also requires that these effects be taken into account in measurements of the optical parameters of polydomain ferroelectric semiconducting crystals.

[1] M. Lines and A. Glass Principles and Applications of Ferroelectrics and Related Materials (Clarendon Press, Oxford, 1977) [Russ. transl., Mir, Moscow, 1981].

[2] V. M. Fridkin, *Ferroelectrics-Semiconductors* [in Russian] (Nauka, Moscow, 1976).

[3] E. G. Fesenko, V. G. Gavrilyachenko, and A. F. Semenchev, *Domain Structure of Multiaxial Ferroelectric Crystals* [in Russian] (Rostov University Press, Rostov-on-Don, 1990).

[4] C. D. Carpentier and R. Nitsche, Mater. Res. Bull. **9**, 1097 (1974).

[5] A. A. Grabar, Yu. M. Vysochanskiĭ, S. I. Perechinskiĭ, L. A. Salo, M. I. Gurzan, and V. Yu. Slivka, Fiz. Tverd. Tela (Leningrad) **26**, 3469 (1984) [Sov. Phys. Solid State **26**, 2087 (1984)].
[6] Yu. M. Vysochanskiĭ and V. Yu. Slivka, *Ferroelectrics in the $Sn_2P_2S_6$ Family: Properties Near the Lifshitz Point* [in Russian], Oriana-Nova, L'vov (1994).
[7] V. P. Terban, A. D. Semak, and A. A. Grabar, *Optoelectronics Materials* [in Russian], Tekhnika, Kiev (1992).
[8] Yu. M. Vysochanskiĭ, M. M. Maĭorov, S. I. Perechinskiĭ, N. A. Tikhomirova, Kristallografiya **37**, 171 (1992) [Sov. J. Crystallogr. **37**, 90 (1992)].
[9] A. I. Otko and I. V. Stasyuk, Ferroelectrics **172**, 207 (1995).
[10] A. A. Grabar, A. I. Bercha, and I. M. Stoĭka, Pis'ma Zh. Tekh. Fiz. **21**(24), 72 (1995) [Tech. Phys. Lett. **22**, 1 (1996)].

Translated by R. M. Durham

Direct confirmation of the Coulomb mechanism for atomic displacement in heavy-ion tracks in a dielectric

V. K. Lyapidevskiĭ and M. I. Ryazanov

Moscow Engineering-Physics Institute
(Submitted October 11 1996; resubmitted April 10, 1997)
Pis'ma Zh. Tekh. Fiz. **23**, 51–54 (August 26, 1997)

It is shown that the results of two independent experiments confirm the Coulomb mechanism for atomic displacement in heavy-ion tracks in dielectrics. © *1997 American Institute of Physics.* [S1063-7850(97)02708-0]

1. It is known that atomic displacements take place in heavy-ion tracks, and various mechanisms have been put forward to explain this effect,[1,2] including Coulomb repulsion of the ions formed in the material.

However, no direct experimental evidence has been provided to support any particular mechanism. Here we show that the displacement of atoms in tracks as a result of Coulomb repulsion of ions formed in the track is directly confirmed by experiments to study the influence of impurity atoms on the properties of the track.

2. It is well known that atomic displacements in tracks do not occur in conducting media but do occur in dielectrics. It may thus be hypothesized that the atomic displacements in a track are associated with some local loss of electrical neutrality over a certain time. In conductors, local loss of electrical neutrality is immediately compensated by conduction electrons. The lifetime of local losses of electrical neutrality in dielectrics is determined by sequential hopping of electrons accompanied by capture of the most weakly bound atomic electrons by ions. The valence electron of an atom nearest to the ion is situated in the net ''two-well'' potential $U(\mathbf{r})$ of its atom $U'(\mathbf{r}-\mathbf{R})$ and the ion $U''(\mathbf{r})$ (the ion is at the origin and the atomic nucleus is at point $\mathbf{R}$). The potential barrier separating these two wells has a minimum at the point $r=b$ on the straight line connecting these two nuclei. The value of b is determined from the extremum condition $dU(b)/dr=0$. A rough estimate for b is obtained through the approximation of Coulomb potentials (Ze is the ion charge):

$$b=Rz^{1/2}/(1+z^{1/2}).; \quad U(b)=-(e^2/R)2(z+z^{1/2}). \quad (1)$$

If the binding energy of the valence electron is $I<|U(b)|$, the valence electron moves freely between nuclei, electrical neutrality is restored as rapidly as in a conductor, and the atoms are unable to undergo displacement. However, if $I>|U(b)|$, the electron has to percolate through the potential barrier, which takes a fairly long time compared with the displacement of the conduction electrons, and Coulomb repulsion is able to displace the ions. Thus the condition for the existence of atomic displacements in heavy-ion tracks has the form $I>|U(b)|$ or $I>e^2n^{1/3}$, if $Z=1$ in Eq. (1).

3. Impurity atoms have a different binding energy I' and particle number density n'. Loss of electrical neutrality can be suppressed by electron hopping via impurities when $I'<|U(b)|\sim e^2n'^{1/3}$. If $I>|U(b)|$ but $I'<|U(b')|$, no atomic displacements will take place in the track.

The incorporation of impurities with weakly bound electrons in a dielectric therefore facilitates the capture of atomic electrons by ions, reducing the lifetime for loss of electrical neutrality, and therefore reduces the number of atomic displacements in the heavy-ion tracks.

It is interesting to verify experimentally how impurities with weakly bound electrons affect the displacement of atoms in ion tracks.

4. It is known that when materials exhibiting thermoluminescence are exposed to gamma irradiation, localized electrons with a binding energy of around 1 eV are formed. In aluminophosphate glass, for example, the binding energy of these electrons is 0.4 eV (Ref. 3). The appearance of weakly bound electrons in a dielectric may also impede atomic displacements in the track if the concentration of localized electrons is fairly high.

It then follows that the nature of the atomic displacements in the tracks may be altered by irradiating the dielectric.

5. Atomic displacements in tracks are usually recorded by measuring the rate of acid etching along the track, using the dependence of this rate on the concentration of displaced atoms.[4] The authors of Ref. 5 investigated the decrease in the number of displaced atoms in tracks of 1 MeV xenon ions per coulomb in aluminum and tritium oxide crystals.[6] The addition of cerium oxide impurities to $Y_3Al_5O_{12}$ reduced the number of displaced atoms in the track, in direct proportion to the number of impurity molecules.

When aluminophosphate glasses were exposed to 1.25 MeV gamma radiation at a dose of 10^6 rad in Ref. 7, it was observed that the number of displaced atoms decreased in the tracks of nickel ions with an energy of 7 MeV per coulomb. An estimate of the concentration of localized electrons using the conversion efficiency yields a value of around 10^{17} cm^{-3} (Ref. 8).

6. It has thus been observed in two independent experiments[5,7] that the appearance of states with weakly bound electrons in a dielectric reduces the number of atomic displacements in heavy-ion tracks. This effect can only be explained in terms of one of the known mechanisms for atomic displacement in tracks — displacement as a result of Coulomb repulsion of product ions.

Hence these measurements may be considered as experimental evidence that the Coulomb mechanism is responsible for atomic displacements in heavy-ion tracks.

This work was supported by the Russian Fund for Fundamental Research (Grant No. 95-2-06059).

[1] R. L. Fleischer, P. B. Price, and R. M. Walker, *Nuclear Tracks in Solids: Principles and Applications* (University of California Press, Berkeley, Calif., 1975) [Russ. transl., Énergoizdat, Moscow, 1981].
[2] S. P. Tret'yakova, Fiz. Elem. Chastits At. Yadra. **23**, 364 (1992) [Sov. J. Part. Nucl. **23**, 156 (1992)].
[3] I. A. Bochvar, T. I. Timadova, I. B. Keirim-Markus *et al.*, *Infrared Spectroscopic Method of Dosimetry* [in Russian], Atomizdat, Moscow (1977).
[4] V. K. Lyapidevskiĭ, in *Solid-State Nuclear Track Detectors and Their Application* [in Russian], Joint Institute for Nuclear Research, Dubna (1990), p. 23.
[5] V. V. Averkiev, V. K. Lyapidevskiĭ, and N. B. Khokhlov, Izv. Akad. Nauk SSSR Ser. Fiz. **50**, 568 (1986).
[6] V. V. Averkiev, Ya. A. Valbis, A. Kh. Grigoryan *et al.*, in *Luminescence Detectors and Ionizing Radiation Converters* [in Russian], Nauka, Novosibirsk (1985), p. 30.
[7] V. K. Lyapidevskiĭ, in *Solid-State Nuclear Track Detectors and Their Application* [in Russian], Joint Institute for Nuclear Research, Dubna (1992), p. 19.
[8] S. A. Zverev, V. K. Lyapidevskiĭ, M. I. Svetlichnyĭ, and N. B. Khokhlov, Izv. Akad. Nauk SSSR Ser. Fiz. **50**, 542 (1986).

Translated by R. M. Durham

Characteristics of anomalous electron emission from the surface of $PbTiO_3$ and $Pb(Zr, Ti)O_3$ ferroelectric films

A. T. Kozakov, A. V. Nikol'skiĭ, I. V. Novikov, Vl. M. Mukhortov, and S. I. Shevtsova

Scientific-Research Institute of Physics at the State University, Rostov-on-Don
(Submitted March 11, 1997)
Pis'ma Zh. Tekh. Fiz. **23**, 55–61 (August 26, 1997)

The possibility of obtaining anomalous electron emission from thin ferroelectric films is investigated and the emission characteristics are compared with those of bulk samples. The results presented indicate that anomalous electron emission may only be observed in nonlinear dielectrics (i.e., those exhibiting ferroelectric instability). The sensitivity of the anomalous electron emission to perovskite structural elements in thin films with a pyrochlore structure is discussed. © *1997 American Institute of Physics.* [S1063-7850(97)02808-5]

Increasing interest has recently been shown in the phenomenon of electron emission from ferroelectric materials caused by a particular electrophysical state of the surface region of polarized ferroelectrics.[1–6] This interest has been stimulated by the various possible applications of the electron emission effect, such as the development of electron sources using ferroelectric materials (cold cathodes) and flat panel displays for various purposes.[5] To obtain electron emission in these studies, electrodes are deposited on either side of the sample and voltages of different polarity are applied at frequencies ranging between a few hundred hertz and several kilohertz.[5] This type of sample is a highly complex system, making it difficult to investigate the fundamental aspects of the effect. Electron emission has been obtained from the surface of bulk ferroelectric samples[1–4] and from thin ferroelectric films.[5]

In Ref. 6, we observed electron emission caused by the presence of an accelerating potential in the surface region when an electrodeless surface of the polarized ferroelectric-electret $PbMg_{1/3}Nb_{2/3}O_3$ ($10\times10\times1$ mm) is exposed to soft x-rays. The potential relief in the surface region responsible for the appearance and spectral profile of this emission is formed as a result of interaction between the charge field of the electrons injected into the sample and the electric polarization field of the ferroelectric which forms as the response of the ferroelectric to the injected charge field.[6] In both cases the fundamental principle of the electron emission is the spontaneous polarization of the ferroelectric sample, although the mechanisms that induce the effect may differ.[2,6] The experiments described in Ref. 6 are more suitable for identifying the fundamental aspects of electron emission from the surfaces of polarized ferroelectrics because there are no electrodes at the emitting surface to complicate the effect. In Ref. 6 the electron emission stimulated from the negative surface of a ferroelectric electret was described as anomalous because the mechanism for its occurrence differed from the photoemission mechanism. It was also shown that the spectrum of anomalous electron emission may be used to investigate ferroelectricity at the microscopic level.

In view of the potential applications of electron emission from the surfaces of thin-film systems,[5] it is interesting to study anomalous electron emission from thin films and to compare its characteristics with the anomalous electron emission from bulk samples. This is the aim of the present study.

The samples used were $PbTiO_3$ films having a perovskite structure and $Pb(Zr, Ti)O_3$ (PZT) films having a pyrochlore structure. Films around 100 nm thick were deposited on (100) MgO by rf cathode sputtering of stoichiometric targets using the technique described in Ref. 7. The films were polarized by the applied electrodes and the electret potential difference V_e was measured by the compensating field method.[8] The anomalous electron emission from the negative surfaces of the films (the surfaces with injected electron charge) was investigated by x-ray photoelectron spectroscopy[9] by a method described in Ref. 6. For comparison we also investigated the anomalous electron emission from the surface of a $PbTiO_3$ single crystal (300 μm thick and measuring 10×8 mm). The composition of the films and the single crystal was investigated by x-ray spectral microanalysis and the structure was studied by means of an x-ray diffractometer. The single crystal was also polarized by the use of applied electrodes. The maximum measured electret potential difference reached 15 V and then fell to zero over 8–15 min. This result is not unexpected: the weak electret properties of $PbTiO_3$ single crystals and ceramics were noted in Refs. 10 and 11. Thus no anomalous electron emission was recorded from the surface of the $PbTiO_3$ single crystal.

However, stable anomalous electron emission was observed from the surface of the $PbTiO_3$ films on (100)MgO and its properties and mechanism of occurrence had many anomalous features comparable to the anomalous electron emission of surface $PbMg_{1/3}Nb_{2/3}O_3$ described in Ref. 6.

In order to eliminate other types of electron emission which have been observed at different times from the surface of thin insulating films (such as SiO_2),[12,13] we carried out the following investigations. The applied electrodes were used to inject an electron charge into the (100) MgO surface and the compensating field method[8] was used to measure the time dependence of the electret potential difference. It was found that MgO is a fairly good electret. The maximum electret potential difference V_e exceeded 300 V and was maintained for several hours. When electrons were excited from this

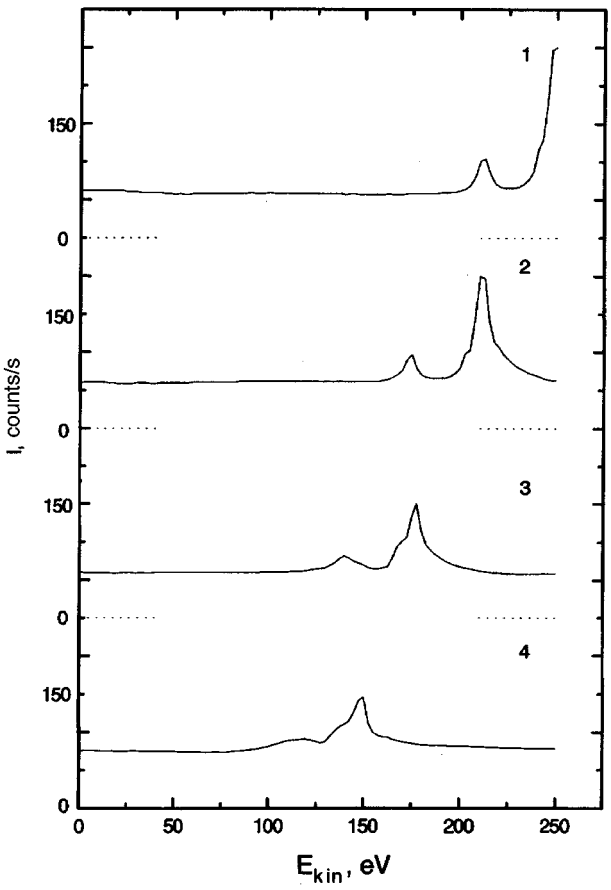

FIG. 1. Change in the spectra of anomalous electron emission from the surface of a polarized $PbTiO_3$ film as a function of irradiation time. Spectra *1–4* were obtained at 30 min intervals.

surface by soft x-rays as in Ref. 6, no anomalous electron emission was observed.

A 100 nm thick SiO_2 film was deposited on cleaved (100) Mg by low-temperature deposition (pyrolysis of tetraethoxysilane in argon vapor). The applied electrodes were used to inject electrons, which were captured by traps. The electret potential difference V_e in the film reached 300 V and remained stable for several hours. Despite the existence of an electret state, no anomalous electron emission was observed from the SiO film.

After a 100 nm thick epitaxial $PbTiO_3$ film having a perovskite structure had been polarized and then exposed to soft x-rays, electron spectra having all the signs of anomalous electron emission were reliably recorded:[6] the beginning of the spectrum coincided with the electret potential difference V_e and the emission was caused by a maximum in the potential distribution at the depth of formation and production of the electron emission spectrum, whose numerical value coincided with the energy position of the high-energy slope of the spectrum. Under prolonged x-ray irradiation, the spectrum was shifted toward lower kinetic energies, its intensity and full width at half-maximum decreased; i.e., the spectrum exhibited relaxation, which is typical of the anomalous electron emission from the surface of $PbMg_{1/3}Nb_{2/3}O_3$ (Ref. 6). However, relaxation of the spectrum accompanied by an increase in the full width at half-maximum was observed for some $PbTiO_3$ films. An example of this relaxation of the spectrum of anomalous electron emission from the surface of $PbTiO_3$ films with a perovskite structure is shown in Fig. 1.

No anomalous electron emission was observed for pyrochlore-structure $Pb(Zr,Ti)O_3$ films after a single polarization, although some was observed after the second and subsequent polarizations (Fig. 2). This effect is interesting because $Pb(Zr,Ti)O_3$ films are linear dielectrics similar to MgO and SiO_2, but no anomalous electron emission has been observed for these, despite repeated polarization. The impression given is that several polarizations of the linear pyrochlore-structure dielectric $Pb(Zr,Ti)O_3$ can result in the formation of a potential relief conducive to anomalous electron emission and which, according to theoretical reasoning,[6] should be formed as a result of the nonlinear response of the ferroelectric to the electret charge injected into the surface. This contradiction may be resolved by assuming that the film

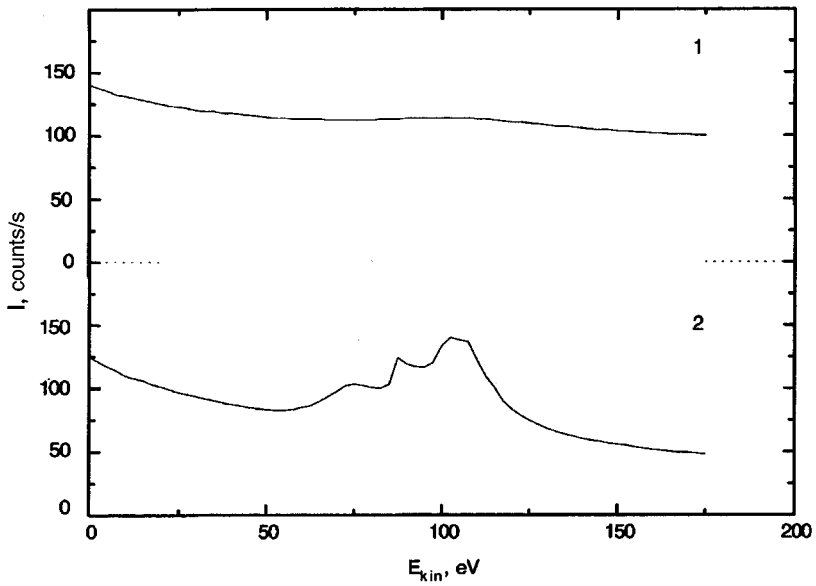

FIG. 2. Change in the spectra of anomalous electron emission from the surface of a singly (*1*) and doubly (*2*) polarized $Pb(Zr,Ti)O_3$ film.

contains a small region with a perovskite structure, which is not observed in the x-ray diffraction data. It may be postulated that the anomalous electron emission is more sensitive to the perovskite structural elements in the thin films than the x-ray diffraction method.

In summary, anomalous electron emission has been observed from films of perovskite-structure $PbTiO_3$ and pyrochlore-structure $Pb(Zr,Ti)O_3$ in x-ray diffraction data but no anomalous electron emission was observed from the surface of a $PbTiO_3$ single crystal. This effect is extremely interesting since in Ref. 4 the theory predicts an abrupt decrease in the electron emission with decreasing thickness of the ferroelectric.

Our experiments using the linear dielectrics MgO and SiO_2 indicate that anomalous electron emission can only occur in nonlinear dielectrics (i.e., those exhibiting ferroelectric instability). Thus the anomalous electron emission observed from the surface of pyrochlore-structure $Pb(Zr,Ti)O_3$ films (according to the x-ray diffraction data) can be attributed to the sensitivity of the anomalous electron emission to a few regions of perovskite structure which are not detected by the x-ray structural analysis.

[1] K. Biedrzychi, Phys. Status. Solidi A **93**, 503 (1986).
[2] L. M. Belyaev and G. Kh. Bendrikova, Fiz. Tverd. Tela (Leningrad) **6**, 645 (1964) [Sov. Phys. Solid State **6**, 506 (1964)].
[3] B. Rosenblum, P. Bräunlich, and J. P. Carrico, Appl. Phys. Lett. **25**, 17 (1974).
[4] G. Rosenman and I. Rez, J. Appl. Phys. **73**, 1904 (1993).
[5] O. Auciello, M. A. Ray, D. Palmer, J. Duarte, G. E. McGuire, and D. Temple, Appl. Phys. Lett. **66**, 2183 (1995).
[6] A. T. Kozakov, V. V. Kolesnikov, V. P. Sakhnenko, A. V. Nikol'skiĭ, I. V. Novikov, E. M. Panchenko, and S. M. Emel'yanov, Fiz. Tverd. Tela. (St. Petersburg) **38**, 2524 (1996) [Phys. Solid State **38**, 1385 (1996)].
[7] V. M. Mukhortov, Yu. I. Golovko, Vl. M. Mukhortov, and V. P. Dudkevich, Izv. Vyssh. Uchebn. Zaved. Fiz. **24**(2), 7 (1981).
[8] A. N. Gubkin, *Electrets* [in Russian] (Mir, Moscow, 1978).
[9] Yu. A. Evdokimov, V. I. Kolesnikov, A. T. Kozakov, V. N. Kravchenko, and A. V. Nikol'skiĭ, Vestn. Mashin. No. 2, 33 (1985).
[10] S. I. Prokopalo, E. M. Panchenko, Yu. I. Trusov, and V. A. Zagoruĭko, Fiz. Tverd. Tela (Leningrad) **32**, 3120 (1990) [Sov. Phys. Solid State **32**, 1810 (1990)].
[11] E. M. Panchenko, Yu. I. Trusov, V. A. Zagoruĭko, S. I. Dudkina, O. N. Razumovskaya, and V. A. Servuli, Izv. Akad. Nauk SSSR Ser. Neorg. Mater. **27**, 1497 (1991).
[12] H. J. Fitting, Exp. Tech. Phys. **24**, 459 (1976).
[13] H. J. Fitting, H. Glaefeke, W. Wild, and M. Franke, Exp. Tech. Phys. **27**(5), 13 (1979).

Translated by R. M. Durham

Undamped self-oscillations in a compensated semiconductor under conditions of impurity breakdown in the presence of a magnetic field

K. M. Jandieri and Z. S. Kachlishvili

Tbilisi State University
(Submitted March 17, 1997)
Pis'ma Zh. Tekh. Fiz. **23**, 62–66 (August 26, 1997)

Conditions for the generation of undamped self-oscillations in a compensated semiconductor in the presence of a magnetic field are studied.
[S1063-7850(97)02908-X]

In Refs. 1 and 2 we derived a criterion for the generation of undamped self-oscillations in a compensated, spatially homogeneous semiconductor undergoing low-temperature electrical breakdown. The dynamics of this physical system were described by a mathematical model whose equations describe generation-recombination processes in shallow impurity levels with the concentration N_d and the degree of compensation C, dielectric relaxation of the electric field **E**, and delay of the electron temperature relative to the change in **E**. This criterion has the form:

$$\tau_d N_d B_T(Z_B) C\left(1-\frac{1}{\gamma}\left(\frac{E}{E_B}-1\right)\right)>\frac{\beta}{2}, \tag{1}$$

where

$$\beta=\left(1+\frac{f'(Z)}{f(Z)}\,\frac{Z}{m}\right)\frac{m}{2}, \quad m=Z\mu'(Z)/\mu(Z),$$

$$\gamma=(A_x(Z_B)+B_T(Z_B))/\beta W\mu(Z_B)C, \quad W=4\pi e/\varepsilon. \tag{2}$$

Here τ_d is the time delay of the electron temperature, Z_B and E_B are the breakdown values of the electron temperature normalized to the lattice temperature ($Z=T_e/T$) and the electric field, respectively; B_T and A_x are the coefficients of thermal recombination and impact ionization, respectively, $f(Z)$ is the total rate of energy loss of the electron gas, μ is the mobility of the free carriers, and ε is the permittivity of the sample. The primes denote derivatives of the corresponding quantities and the value of β is taken at the breakdown point.

Condition (1) is obtained for the case of no additional illumination, where oscillations can only occur in the post-breakdown region of the electric field ($E>E_B$) (Refs. 1–3). The range of variation of E in which undamped oscillations may occur is determined by the inequality $E/E_B-1<\gamma$. The smaller this interval (i.e., the closer the value of E to the breakdown value), the better condition (1) is satisfied, but if the interval is too small, it is difficult to observe the oscillations experimentally. Selecting the optimum value $E/E_B-1=\gamma/2$, condition (1) has the following form:

$$\tau_d B_T(Z_B) N_d C>\beta. \tag{3}$$

From an analysis of this criterion it was established in Refs. 1 and 2 that the occurrence of undamped oscillations is most likely to occur for momentum scattering by phonons in a certain range of N_d, and for fairly high values of C, which is in good agreement with the experiment.[4]

It is known that the magnetic field plays an important role in self-oscillating systems.[5] Here we consider the influence a magnetic field on the behavior of such a system. Conditions without a Hall field ($E_y=0$) are analyzed. A strong, nonquantizing magnetic field H is applied perpendicular to the electric field E_x. Under these conditions, criterion (3) retains its form. The applied field E_x functions as the heating field and the quantity $\mu=e/m^*\langle\tau/(1+\omega_c^2\tau^2)\rangle$ plays the role of the mobility, where ω_c is the cyclotron frequency and τ is the momentum relaxation time. The nature of the dependences $A_I(Z)$ and $B_T(Z)$ obviously does not change in a magnetic field, and thus for a given sample the breakdown value Z_B also remains unchanged. However, the corresponding value of the electric field obviously does vary because of the change in mobility.

When energy is dissipated by acoustic phonons, for $Z\gg1$ we have $f(Z)\propto Z^{3/2}$ (according to the well-known Shockley formula); $Zf'(Z)/f(Z)=3/2$ and if the momentum is also scattered by acoustic phonons, by ionized and neutral impurity atoms, in the absence of a magnetic field we obtain β values of 1/2, 3/2, and 3/4, respectively, according to the notation used in Eq. (2). In a magnetic field the situation changes substantially. For instance, in strong fields ($\omega_c^2\tau^2\gg1$) where the momentum is scattered by acoustic phonons, we have $\mu\propto Z^{1/2}$ and $\beta=1$, i.e., in this case the magnetic field makes it difficult to satisfy condition (3). When the momentum is scattered by impurity ions we have $\mu\propto Z^{-3/2}$ and $\beta=0$, i.e., condition (3) is invariably satisfied (in this case the energy balance equations give $Z\propto E^{2/3}$, i.e., $\mu\propto E^{-1}$ and the drift velocity reaches saturation). When the momentum is scattered by neutral impurity atoms, the magnetic field has no influence on β.

When energy is dissipated in ionizing impurity atoms, $f'(Z)$ can be accurately replaced by $f(Z)/Z$. We then have $\beta=(m/2)(1+1/m)$ and for momentum scattering by impurity ions we obtain $\beta=-1/4$, i.e., β even becomes negative.

We performed computer calculations for arbitrary H. If, in addition to momentum scattering by impurity ions, allowance is also made for scattering by acoustic phonons and neutral impurity atoms, and energy is dissipated by acoustic phonons, in excitation and ionization of impurity atoms (we used expressions from Ref. 6 for the rates of these process), it is impossible to obtain a zero value and particularly a negative value of β (this is partly because when momentum is scattered by impurity ions the theoretical dependence of the momentum relaxation time on the carrier energy $\mathcal{E}$ is

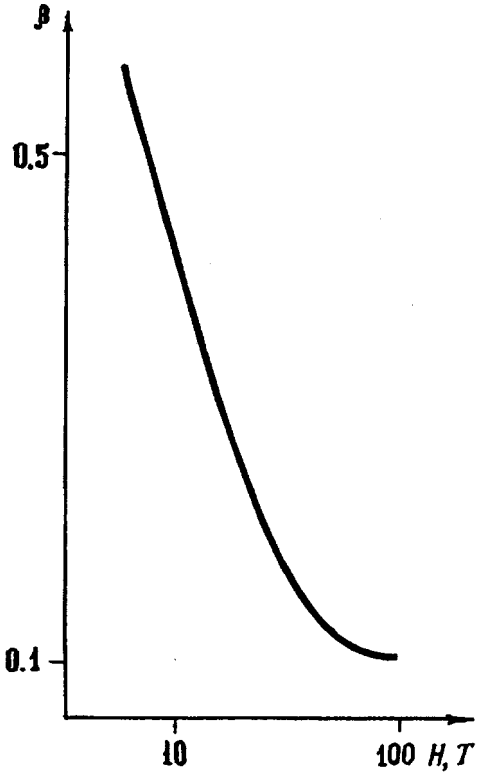

FIG. 1. Dependence of β on H (for explanation see text).

weaker than $\mathcal{E}^{2/3}$ because of the presence of a logarithmic terms). Figure 1 gives β as a function of H for n-Ge under the following conditions: $T=4.2$ K, $C=0.95$, and $N_d=5\times10^{16}$ cm^{-3}.

We now consider the left-hand side of condition (3). At the breakdown point we have $B_T N_d C = A_x N_d (1-C) \sim 1/\tau_x$, where τ_x is the energy relaxation time when this energy is dissipated in ionization of impurity atoms. It was shown in Ref. 1 that $\tau_d \sim \tau_e$, where τ_e is the total energy relaxation time. Under this assumption, the left-hand side of condition (3) is proportional to the ratio τ_e/τ_x and increases with increasing degree of domination of energy dissipation in ionization of impurity atoms over the other dissipation mechanism. As H increases, the left-hand side of condition (3) decreases since the proportionality factor in the dependence of τ_d on τ_2 decreases.

In the presence of a magnetic field, condition (3) is best satisfied when momentum scattering by impurity ions predominates over dissipation of energy in ionization of impurity atoms. As H increases, both the left- and right-hand sides of this inequality decrease. It can therefore be predicted that the condition for the occurrence of undamped oscillations is best satisfied for certain intermediate values of H. This is confirmed by Fig. 2 which gives a bifurcation diagram on the $(E/E_B, H)$ plane for n-Ge under the same conditions as in Fig. 1 for different values of R/r, where R is the resistance of a load connected in series with the sample and r is the resistance of the sample. On this diagram the range of variation of the bifurcation parameters contained within the closed curve corresponds to the saddle-focus equilibrium points, i.e., undamped oscillations in the system.

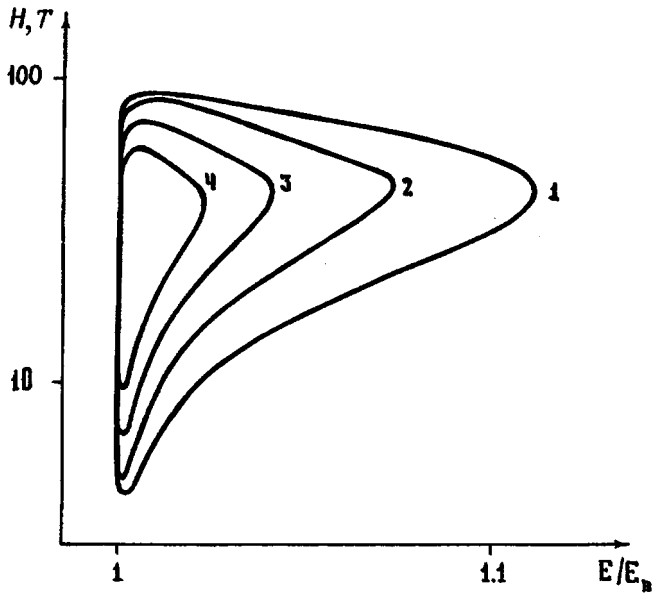

FIG. 2. Bifurcation diagram on the $(E/E_B, H)$ plane for the following values of the ratio R/r: *1* — 0.05, *2* — 0.1, *3* — 0.15, and *4* — 0.2.

[1] Z. S. Kachlishvili and K. M. Jandieri, Bull. Georgian Acad. Sci. **154**, 61 (1996).
[2] Z. S. Kachlishvili and K. M. Jandieri, Bull. Georgian Acad. Sci. **154**, 208 (1996).
[3] Z. S. Kachlishvili and I. D. Kezerashvili, Fiz. Tekh. Poluprovodn. **24**, 1106 (1990) [Sov. Phys. Semicond. **24**, 697 (1990)].
[4] E. I. Zavaritskaya, Tr. Fiz. Inst. Akad. Nauk SSSR **37**, 41 (1966); S. H. Koenig, R. D. Brown, and W. Shillinger, Phys. Rev. **128**, 1668 (1962).
[5] Abe Yutake, Solid State Electron. **31**, 795 (1988); A. Brandle, T. Geisel, and W. Prettl, Europhys. Lett. **3**(4), 410 (1987); M. Weispfenning, I. Hoeser, W. Bohm, W. Prettl, and E. Scholl, Phys. Rev. Lett. **55**, 754 (1985).
[6] Z. S. Kachlishvili, Phys. Status Solidi B **48**, 65 (1971).

Translated by R. M. Durham

Effective rules for combination of interatomic interaction potentials and forces

G. V. Dedkov

Kabardino-Balkarsk State University, Nalchik
(Submitted May 15, 1996; resubmitted March 13, 1997)
Pis'ma Zh. Tekh. Fiz. **23**, 67–75 (August 26, 1997)

New rules are proposed to combine interatomic interaction potentials of neutral atoms by summing (taking into account the sign) geometrically averaged individual contributions of constant sign, calculated using the electron gas model. The formula for the interaction force includes known values of the potentials and forces of homoatomic pairs. The error incurred by using combination relations is compatible with the error of the initial model in the range of internuclear distances $0 \leqslant R \leqslant 8$ a.u. © *1997 American Institute of Physics.* [S1063-7850(97)03008-5]

The search for proven combination rules for interatomic interaction potentials is important for various applications because by successfully solving a problem using 100 potential curves for homoatomic pairs of atoms in the periodic table, it is possible to make elementary calculations of potentials for 4950 possible heteroatomic combinations. This number increases considerably for interaction in ion–atom (ion–ion) systems. This explains why the topic has attracted interest for more than forty years (see Ref. 1 and the references cited therein). The principal disadvantages of all previously proposed combination rules is that they are valid only in restricted ranges of interatomic distances, usually not exceeding a few atomic units, and there are no general formulas for the regions of repulsion and attraction. The aim of the present paper is to provide analytic and numerical justification of a universal method of combining interaction potentials by summing geometrically averaged individual constant-sign contributions to the potential, calculated using the model of an electron gas, which successfully describes the interaction potentials in systems having closed shells for $0 \leqslant R \leqslant 8$ a.u. (Ref. 2). An important factor is that part of the electrostatic interaction is taken into account exactly and gives a Coulomb asymptotic curve for small R. This possibility was first noted in Ref. 1. Although the electron gas model only adequately describes systems with closed shells, calculations of repulsion forces caused by overlap of electron clouds, made using this model, are widely used to determine coupling forces in solids and to model the propagation of accelerated ions in a material.[3,4]

In the standard variant of the model allowing for exchange and correlation,[2] the expression for the interaction potentials of two neutral atoms may be represented as the sum of several terms. Unlike Ref. 2, however, the electrostatic interaction is more conveniently expressed differently[1] (all the formulas are written in atomic units):

$$U(R) = U_e(R) + U_{\rm kin}(R) + U_{\rm ex}(R) + U_{\rm cor}(R), \tag{1}$$

$$\begin{aligned} U_e(R) &= U_e^{(1)}(R) + U_e^{(2)}(R) \\ &= 0.5 Z_1 G_2(R) + 0.5 Z_2 G_1(R) \\ &\quad - 0.5 \int [G_1(r_1) n_2(r_2) + G_2(r_2) n_1(r_1)] d^3\mathbf{r}, \end{aligned} \tag{2}$$

$$G_i(r_i) = \frac{Z_i}{r_i} + V_{ei}(r_i) = \frac{Z_i}{r_i} - \int \frac{n_i(\mathbf{r})}{|\mathbf{r}' - \mathbf{r}_i|} d^3\mathbf{r}', \tag{3}$$

where $n_i(r_i)$, $n_i(\mathbf{r}')$, and $V_{ei}(r_i)$ are the electron density and the potential of the electron cloud of an atom i $(i=1,2)$, Z_i is the corresponding atomic number, and r_i is the distance between a given point and the nucleus of atom i. In the definition of the function $G_i(r_i)$ it is significant that $G_i(r_i) > 0$ for any r_i. The last three terms in Eq. (1) are determined by identical integrals having the form (to simplify the notation the arguments of the functions in the integrand are omitted)

$$U_\alpha(R) = \int [g_\alpha(n_1 + n_2) - g_\alpha(n_1) - g_\alpha(n_2)] d^3\mathbf{r}, \tag{4}$$

where $g_\alpha(n)$ is the corresponding type of energy density (kinetic, exchange, or correlation: α = kin, ex, cor), where $g_{\rm kin}(n) = 2.87 n^{5/3}$ and $g_{\rm ex}(n) = -0.738 n^{4/3}$. The expression for $g_{\rm cor}(n)$ is not given because it is very complicated (see Refs. 1 and 2). For the following analysis it is significant that $U_{\rm cor}(R)$ is negative. Both $U_{\rm ex}(R)$ and $U_e^{(2)}(R)$ are also negative whereas $U_{\rm kin}(R)$ and $U_e^{(1)}(R)$ are positive.

The basic statement made here is that the interaction potentials of a heteroatomic pair of atoms A and B may be expressed in the form

$$\begin{aligned} U^{AB}(R) &= \frac{1}{2}\left[\frac{Z_1}{Z_2} U_e^{AA(1)}(R) + \frac{Z_2}{Z_1} U_e^{BB(1)}(R)\right] \\ &\quad + \sum_\alpha s_\alpha (U_\alpha^{AA}(R) U_\alpha^{BB}(R))^{1/2}, \end{aligned} \tag{5}$$

where $U_\alpha^{AA(BB)}(R)$ are the contributions of the electron gas energy to the interaction potentials of the homoatomic pairs, s_α is their sign, with the sum over α also including a term corresponding to $U_e^{(2)}(R)$, and $U_e^{AA(1)}$ and $U_e^{BB(1)}$ are the homoatomic components of the interaction potential from $U_e^{(1)}(R)$ (see Eq. (2)). The first term in Eq. (5) exactly determines the corresponding part of the interaction potential and is responsible for the Coulomb asymptotic curve $U^{AB} \approx Z_1 Z_2 / R$ for small R.

We obtain an expression for the interaction force $F^{AB}(R)$ by standard differentiation of $U^{AB}(R)$, assuming

that the homoatomic components of the forces $F_\alpha^{AA(BB)}(R)$ are known, as are $F_e^{AA(1)}(R)$ and $F_e^{BB(1)}(R)$, whose notation is explicitly related to that for the potentials:

$$F^{AB}(R) = -\frac{\partial U^{AB}(R)}{\partial R}$$
$$= -\frac{1}{2}\left(\frac{Z_1}{Z_2}F_e^{AA(1)}(R) + \frac{Z_2}{Z_1}F_e^{BB(1)}(R)\right)$$
$$-\frac{1}{2}\sum_\alpha s_\alpha \frac{U_\alpha^{AA}(R)F_\alpha^{BB}(R) + U_\alpha^{BB}(R)F_\alpha^{AA}(R)}{(U_\alpha^{AA}(R)U_\alpha^{BB}(R))^{1/2}}. \quad (6)$$

Let us now justify Eqs. (5) and (6), first considering the term $U_e^{AB(2)}(R)$. We apply the Cauchy–Schwartz inequality (where the subscripts ''1'' and ''2'' indicate the positions of the nuclei, ''A'' and ''B'' indicate the type of atoms, and the arguments of the functions in the integrand are omitted for conciseness)

$$\int (n_{1A}G_{1A}n_{1B}G_{2B})^{1/2}d^3\mathbf{r}$$
$$\leqslant \left\{\left(\int n_{1A}G_{2A}d^3\mathbf{r}\right)^{1/2}\left(\int n_{1B}G_{2B}d^3\mathbf{r}\right)^{1/2}\right\}. \quad (7)$$

However, direct numerical calculations indicate that the following relation holds

$$0.5\int (n_{1A}G_{2B} + n_{2B}G_{1A})d^3\mathbf{r}$$
$$\geqslant \int (n_{1A}G_{2A}n_{1B}G_{2B})^{1/2}d^3\mathbf{r}. \quad (8)$$

The function in the integrand on the right-hand side of inequality (8) is not the geometric average of the functions in the integral on the left-hand side (otherwise it would be trivially satisfied). Taking into account inequalities (7) and (8), we replace the left-hand side of inequality (8) with the product of the integrals on the right-hand side of inequality (7), which is equivalent to evaluating $U_e^{AB(2)}$ using the geometric average rule. In this case, there is clearly some compensation for the incurred error. The result is of course accurate for a homoatomic pair. For the other contributions to the potential, the numerical calculations indicate that the following inequalities are satisfied

$$\int [g_\alpha(n_{1A}+n_{2B}) - g_\alpha(n_{1A}) - g_\alpha(n_{2B})]d^3\mathbf{r}$$
$$\geqslant \int \{[g_\alpha(n_{1A}+n_{2A}) - g_\alpha(n_{1A}) - g_\alpha(n_{2A})]^{1/2}$$
$$\times [g_\alpha(n_{1B}+n_{2B}) - g_\alpha(n_{1B}) - g_\alpha(n_{2B})]^{1/2}\}d^3\mathbf{r}. \quad (9)$$

Again applying the Cauchy–Schwartz inequality (to the right-hand side of expression (9)), the integral on the left-hand side can again be estimated by the geometric average of the homoatomic potentials (with partial compensation for the error).

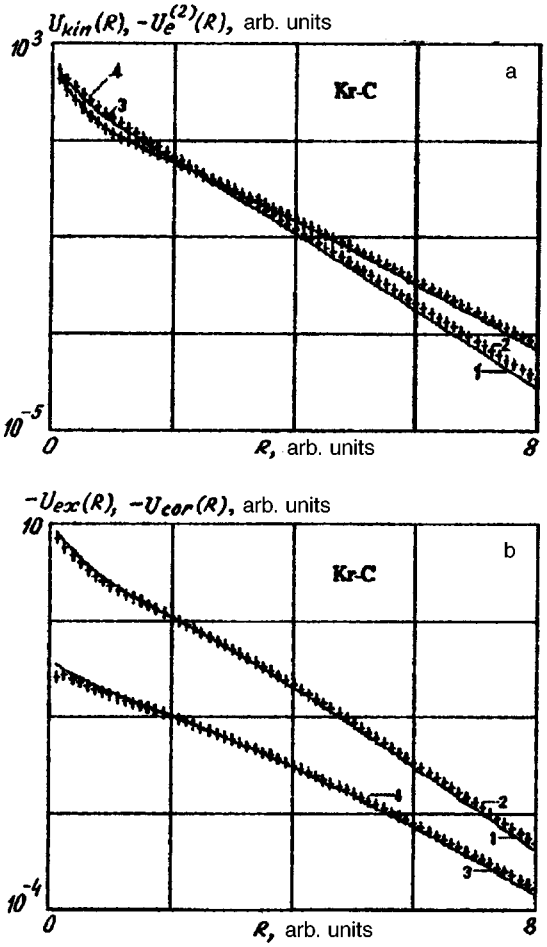

FIG. 1. Separate contributions to the interaction potential of Kr–C as functions of the internuclear distance R. Curves *1* and *3* were obtained using the combining formulas and correspond to $-U_e^{(2)}(R)$, $U_{\text{kin}}(R)$ for case *a* and $-U_{\text{ex}}(R)$, $-U_{\text{cor}}(R)$ for case *b*. Curves *2* and *4*, in the same order, give the exact calculations using formulas (1)–(4). All the values are given in atomic units.

This argumentation clearly does not guarantee final success in applying Eqs. (5) and (6) but provides the stimulus for a numerical analysis.

Numerical calculations of homoatomic and heteroatomic interaction potentials were made using an analytic approximation of the Hartree–Fock electron distributions for neutral atoms taken from Ref. 5, which gives a compact computer program. The criterion used to assess the accuracy of the combination formulas (5) and (6) was to compare the results of calculations using these and those of direct calculations of heteroatomic interaction potentials using formulas (1)–(4).

The most critical case for such a comparison is that where there is a large difference between the atomic numbers of the interacting particles, therefore a Kr–C pair was considered as the first representative example. Figures 1a and 1b show results of calculations of the various contributions to the interaction potential (without the term $U_e^{(1)}(R)$ taken into account exactly). The solid curves give the combination rules and the crosses give the accurate calculations. For convenience, all the terms of the interaction potentials are taken in terms of the modulus. Figures 2a, 2b, and 2c give the result-

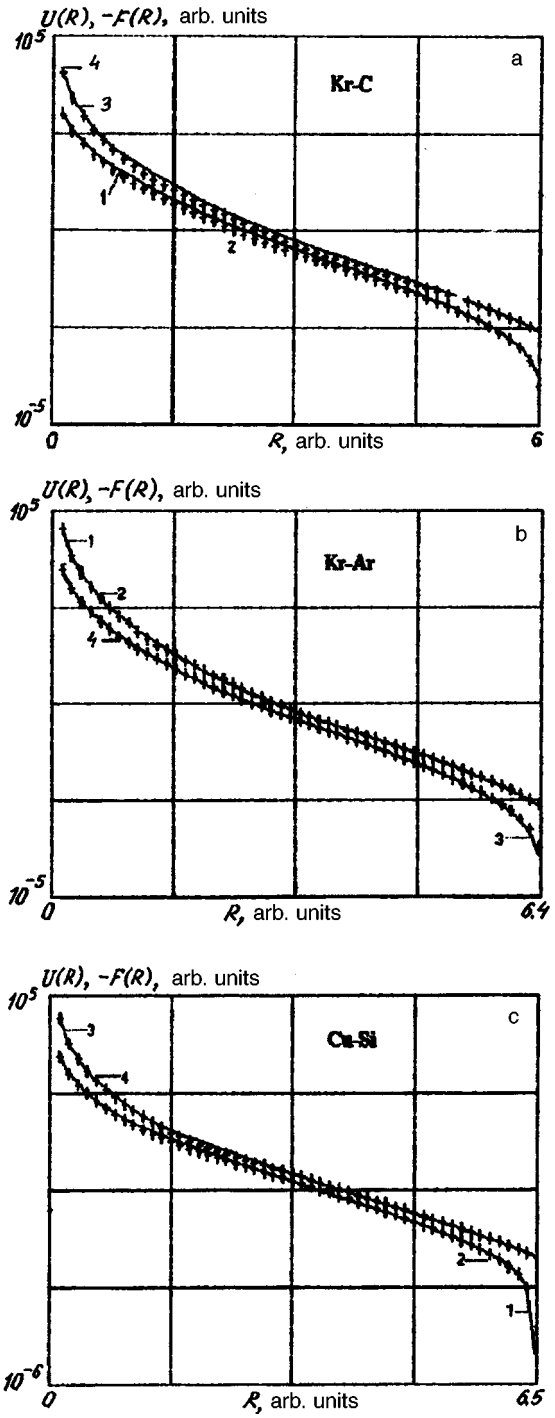

FIG. 2. Resultant potential, curves (*1*, *2*) and force (*3*, *4*) curves for Kr–C (*a*), Kr–Ar (*b*), and Cu–Si (*c*) for repulsion: *1*, *3* — combining rules, *2*, *4* — exact calculations. For convenience all the forces have their signs changed.

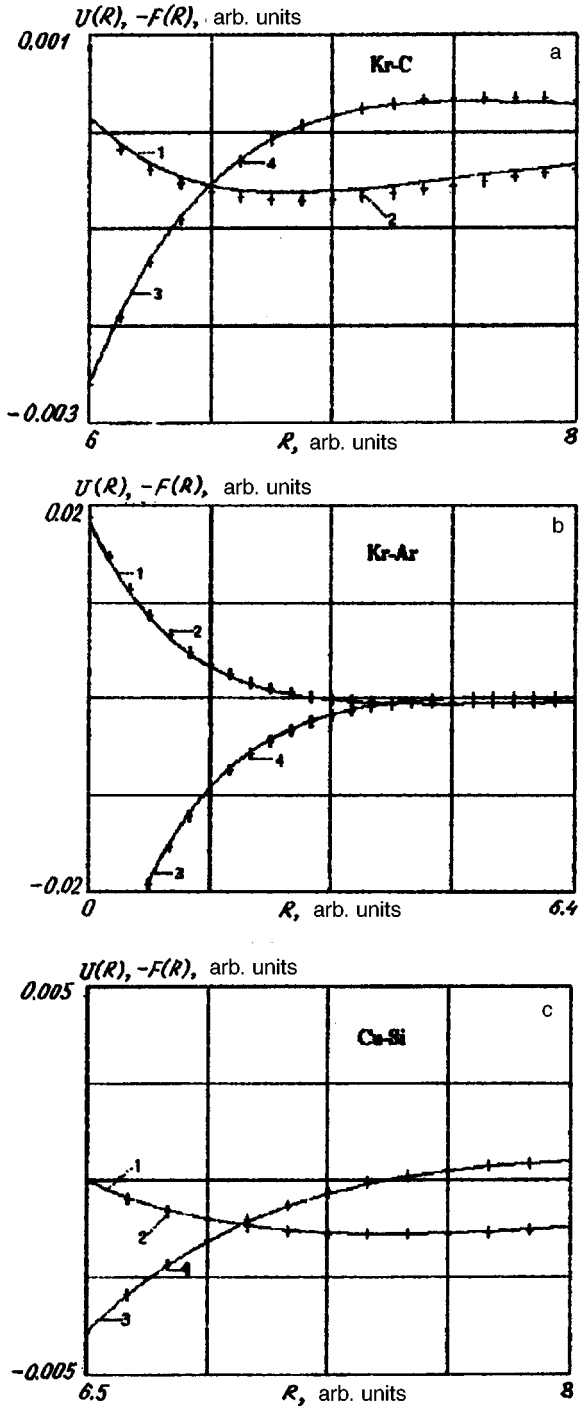

FIG. 3. As Fig. 2 for regions of attraction. All the forces also have their signs changed.

ant dependences of the interaction potentials and the interaction forces for the combinations Kr–C, Kr–Ar, and Cu–Si. The regions of repulsive interaction are shown. The regions of attraction are given separately in Figs. 3a, 3b, and 3c. The figures show extremely good agreement between the potential curves and the force curves obtained using formulas (5) and (6), and by direct integration using formulas (1)–(4) over the entire range of R values, even giving the correct position and depth of the minimum. The difference compared with the accurately calculated potentials does not generally exceed 10%, i.e., is comparable with the initial accuracy of the electron gas model. Although the approximation used for the electron densities is not the most accurate nowadays, the results suggest that the combination formulas (5) and (6) should still hold when other atomic approximations are used. A more detailed comparison between the curves in Fig. 1 and Figs. 2 and 3a for Kr–C also indicates additional compensation for the errors from summation of the contributions of different sign to the interaction potentials (compare

the behavior of the individual components and the resultant potentials for $R>5$ a.u.).

These results are also typical of all the other calculated heteroatomic combinations with atomic numbers $Z_{1,2}\leqslant 36$. It can therefore be concluded that it is promising to use the proposed combination formulas to calculate interatomic interaction potentials and forces.

[1] G. V. Dedkov, Usp. Fiz. Nauk **165**, 919 (1995).
[2] R. G. Gordon and Y. S. Kim, J. Chem. Phys. **56**, 322 (1972).
[3] W. A. Harrison, *Electronic Structure and the Properties of Solids* (Freeman, San Francisco, 1980) [Russ. transl., Mir, Moscow, 1983].
[4] J. P. Biersack, Nucl. Instrum. Meth. Phys. Res. B **27**, 21 (1987).
[5] G. Strand and R. A. Bonham, J. Chem. Phys. **40**, 1686 (1964).

Translated by R. M. Durham

Vortex optical Magnus effect in multimode fibers

V. V. Butkovskaya, A. V. Volyar, and T. A. Fadeeva

Simferopol State University
(Submitted December 16, 1996)
Pis'ma Zh. Tekh. Fiz. **23**, 76–81 (August 26, 1997)

A theoretical and experimental analysis is made of the optical Magnus effect in multimode optical fibers excited by a laser beam whose wavefront has a pure screw dislocation and carries the topological charge $\pm l$, where l is the azimuthal quantum number. It is found that the angular rotation of the plane of propagation of a local wave depends on the magnitude and sign of the topological charge and changes qualitatively when the circulation of the polarization is reversed. The phase mechanism is attributed to spin-orbit interaction in the photon ensemble. It is demonstrated experimentally that the optical Magnus effect in a few-mode fiber for the CP_{11} mode at the beat length is observed as a rotation of the axis of the pure edge dislocation field through an angle proportional to the beat length.
[S1063-7850(97)03108-X]

The propagation of a polarized meridional local plane wave through a multimode fiber is associated with rotation of the plane of propagation of the wave about the axis of symmetry of the fiber. In optical fibers with a parabolic refractive index profile, which conserve the polarization state of the wave, the plane of propagation of the wave undergoes a circular rotation, which has been described as the optical Magnus effect.[1] Optical fibers with a stepped refractive index profile do not conserve the polarization state of the wave and thus the plane of propagation of a local wave oscillates about some arbitrary equilibrium state.[2,3]

It is known that the optical vortices of an electromagnetic wave carry an angular momentum additional to the wave spin.[4] It is expected that the specific rotation of the plane of polarization of the wave carrying the topological charge will respond to the magnitude and sign of the topological charge l of the vortex of the exciting beam. Here we report an experimental investigation of the rotation of the wave caustic in a multimode optical fiber as a function of the magnitude and sign of the topological charge l and we also study the characteristic features of the optical Magnus effect in few-mode graded-index fibers.

1. An experimental investigation was made of the specific rotation $\varkappa$ of the wave caustic formed at the exit end of a multimode fiber as a function of the magnitude and sign of the topological charge l of a pure screw dislocation of the exciting-beam wavefront. The experimental apparatus used in Ref. 2 was used as the basis for this study. Linearly polarized laser radiation was passed through a optical polarization modulator, after which the polarization state varied from linearly polarized to right circularly polarized at frequencies between 0.1 and 10 Hz. The modulated laser beam was incident on a phase transparency with a computer-generated hologram of a screw wavefront dislocation, having the topological charge l. The computer-generated holograms were created by the technique described in Ref. 5. After the hologram, the light was focused onto the entry end of the fiber by a $20\times$ microscope objective such that predominantly meridional rays propagated in the fiber. The sample used was a straight multimode fiber with a stepped refractive index profile, having diameter $D=0.5$ mm, length $l=7$ cm, and numerical aperture $A=0.65$. The near-field pattern of the exit end of the fiber was projected into the plane of the screen by an $f=3$ cm short-focus lens. The meridional excitation of the fiber was tuned using the pattern of the wave caustics. The angular displacement $\varkappa$ of an arbitrary wave caustic was measured for two successive polarization states of the light after the modulator. For given l the angular displacement $\varkappa$ was then averaged for different meridional caustics.

The results of the measurements are plotted in Fig. 1 as a family of curves giving the specific angular displacement $\varkappa$ as a function of the magnitude and sign of the topological charge l of an optical vortex of the exciting laser beam.

For the same directions of σ and l, the angular displacement $\varkappa$ increases with increasing modulus $|l|$ of the topological charge, whereas for opposite directions of σ and l, the angular displacement $\varkappa$ decreases monotonically with increasing $|l|$.

A simultaneous reversal of the signs of σ and l does not alter the nature of the curve $\varkappa(l)$ and merely corresponds to an angular rotation of $\varkappa(l)$ about the origin. The angular displacement $\varkappa$ for a Gaussian beam carrying no optical vortex ($l=0$) is typically less than that for the topological charge $|l|=1$.

The behavior of the angular displacement $\varkappa$ of the caustics in a multimode fiber as a function of the topological charge of the exciting optical field is treated physically in terms of the vector nature of the spin σ and orbital angular momentum l of the optical vortex. The field propagating in the fiber carries the z component of the total angular momentum, which is defined[4] per photon as $L_z=(l_\sigma)/\omega$ (here $\sigma=\pm 1$ is the spin number). As the topological charge increases, the intrinsic angular momentum of the photon obviously increases. This angular momentum is added to the spin angular momentum with allowance for the sign of the circulation of the electric vector and causes additional twisting of the caustics. This explains the different branches of the curves in Fig. 1 for the different signs of l and σ. We did not obtain a linear relation between the angular rotations $\varkappa$ and the azimuthal number l. This is evidently because of the

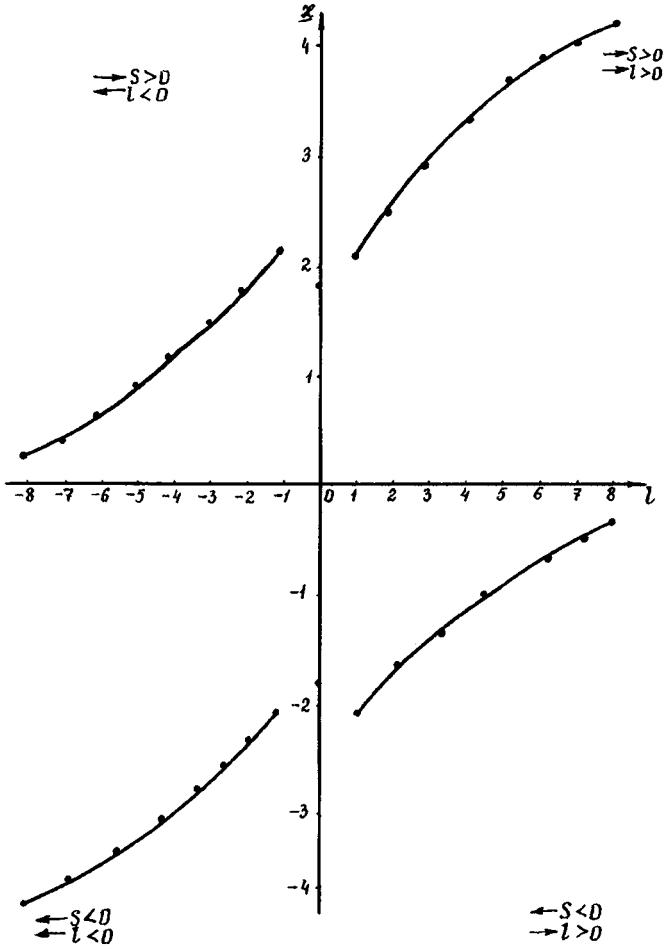

FIG. 1. Angular displacement $\varkappa$ versus topological charge l of vortex (σ is the spin number and l is the azimuthal quantum number of the vortex).

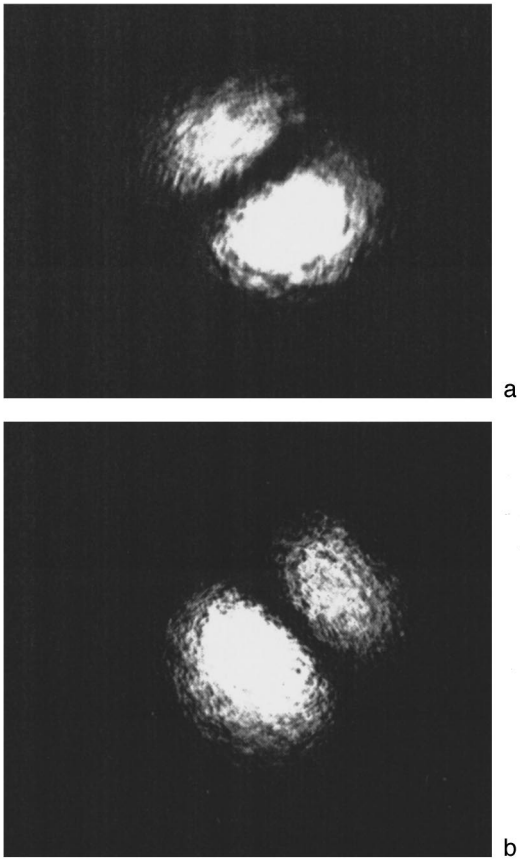

FIG. 2. Photographs of the radiation field of the circularly polarized CP_{11} mode at half the beat length: a — excited by right circularly polarized light, b — excited by left circularly polarized light.

nonuniform distribution of the angular momentum over the fiber cross section,[4] since the field in the fiber cannot be represented as a paraxial beam and a cross term appears in the description of the angular momentum of the field.

2. An experimental investigation was made of the optical Magnus effect in a few-mode fiber excited by a smooth Gaussian beam. We selected a stepped-index fiber having a core diameter $D=3.5\ \mu$m, which supported the HE_{11}, HE_{21}, TE_{01} and TM_{01} modes. The maximum measured beat length was 3.8 m. The fiber was excited by radiation which had been passed through a phase mask with the profile of the LP_{11} mode to suppress the excitation of the HE_{11} mode as far as possible. The fiber was broken off 2 cm at a time until the pattern of the radiation field reproduced the field of the LP_{11} mode turned through an angle of 38° (Fig. 2a). Then the polarization state was changed to left circularly polarized by means of an electrooptic modulator. As a result, the radiation field pattern of the mode was rotated through $-42°$ (Fig. 2b). In a few-mode fiber excited by a smooth wave, pure edge and pure screw disclinations of the vector field are superposed to form optical vortices. It can be shown that the field of a pure edge dislocation of the circularly polarized CP_{11} mode at the beat length $\Delta\beta z_0=m\pi$ (where $\Delta\beta=-\delta\beta_1/2$, $\delta\beta_1$ is the polarization correction to the HE_{11} mode) has the form:

$$E\Rightarrow\cos(\phi-\sigma_z\delta\beta_{21}z_0)\begin{pmatrix}1\\ \sigma_z i\end{pmatrix}.$$

Here the ''+'' and ''-'' signs correspond to excitation of the fiber by right and left circularly polarized light, respectively. Reversal of the direction of circulation of the circular polarization rotates the axis of the pure edge dislocation through the angle $\Delta\phi=2\,\delta\beta z_0$. These results show that the optical Magnus effect in a fiber is determined by the polarization correction to the HE_{21} mode.

This work was partially supported by the International Soros Program for the Support of Education in the Exact Sciences (ISSEP), Grant N PSU062108.

[1] A. V. Dugin, B. Ya. Zel'dovich, N. D. Kundikova, and V. S. Liberman, Zh. Éksp. Teor. Fiz. **100**, 1474 (1991) [Sov. Phys. JETP **73**, 816 (1991)].
[2] A. V. Volyar and S. N. Lapaeva, Pis'ma Zh. Tekh. Fiz. **18**(8), 53 (1992) [Sov. Tech. Phys. Lett. **18**, 261 (1992)].
[3] A. V. Volyar, S. N. Lapaeva, and Yu. N. Mitsaĭ, Pis'ma Zh. Tekh. Fiz. **20**(5), 32 (1994) [Tech. Phys. Lett. **20**, 190 (1994)].
[4] B. Zeldovich, Phys. Rev. A **5**, 7980 (1991) [*sic*].
[5] V. Yu. Bazhenov, M. S. Soskin, and M. V. Vasnetsov, J. Mod. Opt. **39**, 985 (1992).

Translated by R. M. Durham

Parametric regeneration of spin oscillations of a thin-film ferromagnetic cavity by microwave pumping

B. A. Kalinikos, N. G. Kovshikov, and E. A. Ospanov

St. Petersburg State Electrical Engineering University
(Submitted May 15, 1997)
Pis'ma Zh. Tekh. Fiz. **23**, 82–87 (August 26, 1997)

An experimental investigation is made of the regeneration of spin oscillation losses in a thin-film ferromagnetic cavity by parametric pumping. It is observed that effective regeneration only takes place in narrow frequency intervals in zones of strong dispersion near dipole gaps in the spin wave spectrum of thin films with bounded mobility of the surface spins. It is shown that microwave parametric pumping can substantially improve the Q factor of dipole-exchange spin oscillations of the thin-film cavity. © *1997 American Institute of Physics.*
[S1063-7850(97)03208-4]

The use of a four-wave process to amplify traveling spin waves in yttrium iron garnet thin films was recently reported for the first time.[1] The authors observed the amplification of a weak (signal) spin wave by a traveling pump spin wave of finite amplitude. The signal and pump waves had similar frequencies and propagated in the same direction. The carrier frequencies of the waves were selected to be in the strong dispersion region near one of the dipole ''gaps'' in the spin wave spectrum. The theoretical model proposed in Ref. 1 shows that the four-wave parametric process leading to the amplification of traveling spin waves can also be used to regenerate standing spin waves. In other words, four-wave parametric mixing can be used to regenerate the natural oscillation losses of thin-film ferromagnetic cavities.

The aim of the present study was to make an experimental investigation of the regeneration of the natural oscillation losses of a thin-film ferromagnetic cavity by microwave parametric pumping. As in Ref. 1, the signal and pump had similar frequencies, situated in zones of strong spin-wave dispersion.

The cavity was fabricated of high-Q single-crystal yttrium iron garnet film (half-width of ferromagnetic resonance curve $\Delta H=0.6$ Oe) of thickness $L=9$ μm, grown on a [111]-oriented gadolinium gallium garnet substrate. The film used for the experiments had pinned surface spins. It was previously shown theoretically and experimentally[2,3] that the spin wave spectrum of these films has zones of strong dispersion. These zones showed up experimentally as ''dips'' on the amplitude-frequency transmission characteristic of the microwave signal.

The planar dimensions of the thin-film cavity were selected as 4×12 mm to obtain a multiresonance spectrum of spin oscillations. The smaller dimension ensured that standing spin waves — spin oscillations — were formed with closely spaced resonant frequencies. Some of the resonant frequencies of these oscillations fell within the zones of strong dispersion. The larger dimension of the thin-film cavity had almost no influence on the formation of the spectrum of natural oscillation frequencies since its value was greater than the mean free path of the spin wave.

The prototype used for the investigations consisted of a Polikor plate on which a microstrip spin-wave antenna 50 μm wide and 4 mm long, and a strip supply line were formed by photolithography. The thin-film sample was placed on top of the antenna, with the longitudinal axes of the sample and the antenna coinciding. The sample was uniformly magnetized perpendicular to its surface.

Spin-wave oscillations were excited by a microwave signal supplied to the prototype antenna from an oscillator via a directional coupler. The pump signal was supplied to the same antenna from a similar oscillator via a microwave amplifier. The measurements were made using a reflection system, recording the reflected signal with a spectrum analyzer.

The experiment consisted of two stages. At the first stage, the spectrum of natural oscillations of the cavity was studied. The results of measurements of the spectra are shown in Fig. 1b. For clarity the experimental data are shown against the theoretically calculated spectrum of dipole-exchange spin waves A (Fig. 1a). The calculations were made using the following parameters of the experimental sample: thickness $L=9$ μm, saturation magnetization $M_0=1750$ Oe, inhomogeneous exchange interaction constant $\alpha=3.1\times10^{-12}$ cm^2, and pinned surface spin state. The calculated spectrum typically exhibits zones of ''repulsion'' of the dispersion curves. These repulsion zones — dipole gaps — are formed near points of degeneracy of the fundamental mode with higher-order modes having odd indices n. This aspect has already been discussed in some detail in Refs. 2–4.

The experimental curve in Fig. 1b gives the relative amplitude of the resonant oscillations as a function of frequency. It can be seen from a comparison of Figs. 1a and 1b that the resonances corresponding to the weak-dispersion parts of the spectrum have a higher intensity than those corresponding to the strong-dispersion parts.

The aim of the second stage of the experiment was to study the regeneration of the resonant oscillation losses in the cavity, and was carried out as follows. The behavior of the spin system of the sample was first studied under the application of only one harmonic signal — the pump signal — while the power and tuning of the carrier signal were varied. In the course of these measurements we recorded modulation instability of various natural cavity oscillations situated in zones of strong dispersion.[1)] In particular, a

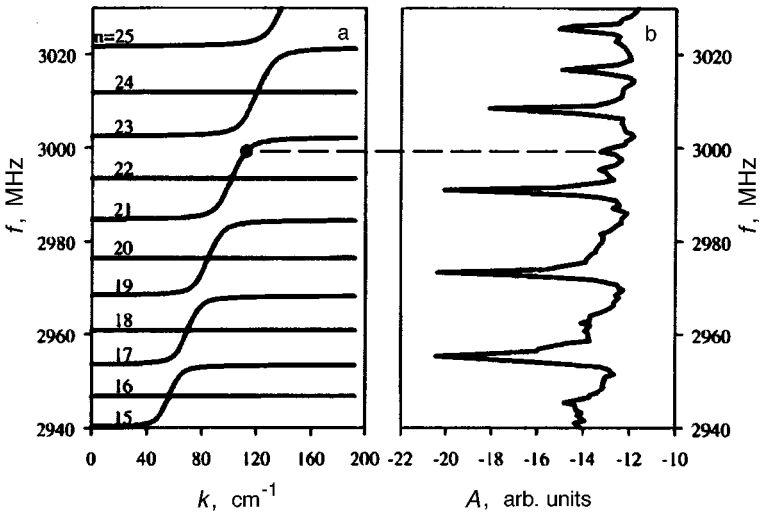

FIG. 1. Theoretical spectrum of spin waves (a) and experimental frequency dependence of the reflection coefficient (b) for the yttrium iron garnet film under study. The dashed line gives the resonant frequency of the dipole-exchange spin oscillation used for parametric regeneration.

modulation instability threshold $P_{\text{th}}=7.71$ mW was obtained for the resonant oscillation at $f_s=2999$ MHz, which was subsequently selected as the working oscillation. Then by applying two frequencies simultaneously — the signal and the pump — we studied the change in the Q factor of the natural oscillation mode when the pump power was lowered below the modulation instability threshold. The selected signal frequency f_s was kept constant (resonant for one of the oscillation modes) and the pump frequency f_p was tuned over a wide range. We stress that all the resonances were pumped parametrically during the experiment, but effective regeneration of the losses was only observed at the peaks of the low-intensity oscillations whose frequencies were located near the dipole gaps in the spin wave spectrum. In other words, it was observed that only those oscillation modes formed by strong-dispersion spin waves were effectively regenerated.

Measurements of the profile of the resonant peak with the initial frequency f_s = 2999 MHz on application of a pump wave at the frequency $f_p=3005$ MHz are plotted in Fig. 2. When the signal level was maintained at $P_s=2.1$ μW and the pump level was varied between low-power and the threshold, compensation of the losses was observed in the form of a decrease in the width of the peak. A nonlinear shift of the frequency f_s was also observed. The maximum regeneration effect was observed when the spacing between the pump and signal frequencies was $f_p-f_s=3.5$ MHz.

Figure 3 gives the loaded Q factor as a function of the pump wave power P_p. The Q factor was determined by the usual expression $Q=f_s/\Delta f$, where f_s is the resonant frequency and Δf is the width of the resonant peak at half power. It can be seen that doubling the pump power increases the Q factor approximately seven times. The maximum Q factor was $Q_{\max}=15\,000$. As the pump power increased, no transition from regeneration to lasing was observed. The absence of lasing can be ascribed first to the fairly strong coupling between the cavity and the external circuit and second to the instability established above the threshold P_{th}.

To conclude, a thin-film cavity of dipole-exchange spin waves has been investigated experimentally under conditions of parametric pumping at a frequency very close to the signal

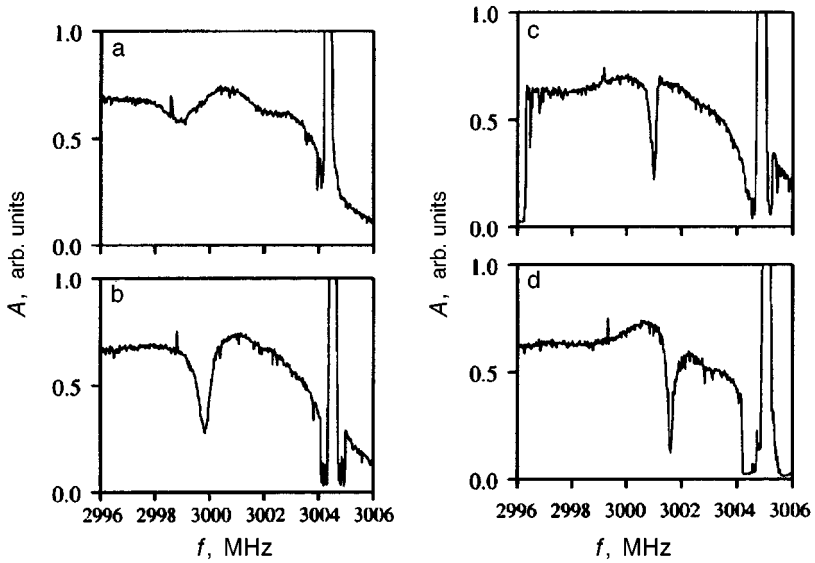

FIG. 2. Change in the profile of the resonant peak corresponding to the parametrically regenerated spin oscillation with increasing pump power P_p: a — 3.7 mW, b — 5.05 mW, c — 7.56 mW, and d — 7.66 mW.

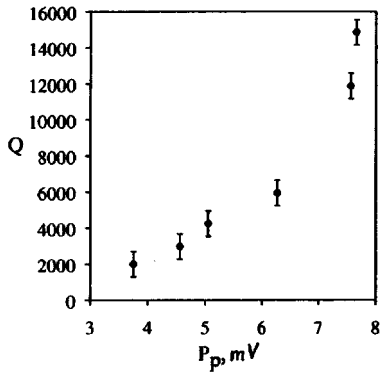

FIG. 3. Q factor of dipole-exchange spin oscillation as a function of pump power.

frequency. It has been shown that the losses can be regenerated and the Q factor of the spin oscillations improved substantially by means of the pump signal.

This work was partially supported by the Russian Fund for Fundamental Research, Grant No. 96-02-19515, and also by the German Ministry of Education, Science, Research and Technology, Grant No. 50TT9606.

[1)]A detailed discussion of the pattern of this modulation instability is outside the scope of the present study.

[1] B. A. Kalinikos, N. G. Kovshikov, M. P. Kostylev, and H. Benner, JETP Lett. **64**, 171 (1996).
[2] B. A. Kalinikos and A. N. Slavin, J. Phys. C **19**, 7013 (1986).
[3] B. A. Kalinikos, N. G. Kovshikov, and A. N. Slavin, Zh. Éksp. Teor. Fiz. **94**(2), 159 (1988) [Sov. Phys. JETP **67**, 303 (1988)].
[4] A. V. Lugovskiĭ and P. E. Zil'berman, Fiz. Tverd. Tela (Leningrad) **24**, 458 (1982) [Sov. Phys. Solid State **24**, 259 (1982)].

Translated by R. M. Durham

Characteristic features of low-temperature gas-discharge plasma flows

A. P. Bedin

A. F. Ioffe Physicotechnical Institute, Russian Academy of Sciences, St. Petersburg
(Submitted April 25, 1997)
Pis'ma Zh. Tekh. Fiz. **23**, 88–93 (August 26, 1997)

An investigation is made of the nature of gasdynamic anomalies accompanying the motion of shock waves and objects in a low-temperature nonequilibrium plasma. It is shown that these anomalies are caused by characteristic features of sound propagation in the plasma. © *1997 American Institute of Physics.* [S1063-7850(97)03308-9]

Recent investigations have revealed various characteristic features in the flows of a low-temperature plasma compared with flows of heated and cold air. These features include an extension of the velocity range where subsonic flow takes place around objects in the plasma,[1] increased separation of the shock wave head from objects travelling in the plasma,[1] reduced intensity, increased propagation velocity, and changes in the structure of shock waves,[2–8] changes in the resistance of objects,[9,10] and so forth.

In our opinion, most of these characteristics are attributable to changes in the velocity of sound and its dispersion, caused by relaxation processes which take place when a sound wave propagates in the plasma.

In order to determine the velocity of sound in a plasma, we analyze dependences of the drag coefficient C_x as a function of its velocity V in cold air ($T_c=290$ K) and heated air ($T_h=1200$ K), and also in a plasma ($T_p=1200$ K, $T_e=4$–6 eV) plotted in Fig. 1a. Here and subsequently, the subscripts c, h, and p refer to cold and hot air, and to the plasma, respectively. All the curves are plotted at pressure $P=15$ Torr and sphere diameter $d=15$ mm. Curves *1* and *2* were plotted using our results and data from Ref. 11 and curve *3* was plotted using our data.[10] The adiabatic exponent was taken as $\gamma_h=\gamma_c=1.4$.

On comparing the V shift of the curves $C_x=C_x(V)$ and knowing that the shift in cold and hot air is caused by a difference between the velocities of sound, it is easy to conclude that the velocity of sound, a_p, in a plasma differs from that in cold and heated air (a_c and a_h), where $a_c<a_h<a_p$. Then, assuming that $M_c=M_h=M_p$: $C_{xc}\approx C_{xh}\approx C_{xp}$, the velocity of sound in the plasma can be estimated. According to the estimates $a_p\approx 1.45a_h$ ($T_p=T_h=1200$ K, $T_e=4$–6 eV). Similar estimates made in Ref. 1 using the separation of the shock wave head from a sphere yielded $a_p\approx 1.5a_h$ ($T_p=T_h=1400$ K, $T_e=1$–2 eV). From this it can be seen that in the range $T_e=1$–6 eV the velocity of sound in an air plasma is almost independent of T_e and may be taken as $a_p=1.48a_h=29.7\sqrt{T}$. This means that the results of measurements of the coefficient C_x of a sphere in a plasma can be plotted as a function of the M number (see Fig. 1b, which gives the curves $C_x=C_x(M)$ in cold and hot air for $\mathrm{Re}_h=\mathrm{Re}_c=1.2\times 10^3 M$ and $\gamma_h=\gamma_c=1.4$). It can be seen from an analysis of the figure that for numbers $M>0.8$ the coefficient C_x in the plasma is several times greater than in air. This may be caused by a decrease in the adiabatic exponent, a slight increase in the plasma viscosity, and also by splitting of the shock wave into two (a precursor and a residual shock wave). Assuming that heated air in equilibrium at $T=1200$ K, $\gamma_h\approx 1.3$, it can be taken that $\gamma_p=1.25$. Together with the previously determined velocity of sound in a plasma, this exponent can be used to calculate the ratio $\overline{C_x}=C_x/\overline{P_0'}$ in a plasma ($\overline{P_0'}=2P_0'/\rho V^2$ is the relative stagnation pressure behind the shock wave) and in air. The results are plotted in Fig. 2b, which also gives the values of $\overline{C_x}=C_x/\overline{P_0'}$ for a sphere in different gases for $\mathrm{Re}\sim 10^6$ plotted using data from Ref. 12. It can be seen that the adiabatic exponent negligibly influences $C_x/\overline{P_0'}$ (in a plasma this is observed for $M>0.8$). According to Ref. 12, $C_x/\overline{P_0'}$ is self-similar in terms of γ for any objects and any numbers M. Assuming that this property is also conserved for a plasma, and not only in the range $M=0.8$–1.2 but also for $M>1.2$, the coefficient C_{xp} and the drag force X_p of the objects can be estimated from their well-known drag coefficient C_{xc} in air, using the conversion:

$$C_{xp}=C_{xc}P_{0p}'/\overline{P_{0c}'},$$

$$X_p=C_{xc}\rho_p V^2\overline{P_{0p}'}/2\overline{P_{0c}'}.$$

For a sphere with $V>a_p$ we have $X_p\approx X_c T_c/T_p$. In our case $X_p\approx 0.25X_c$ is obtained.

For numbers $M<0.7$ the drag coefficient of a sphere in a plasma, judging by the data plotted in Fig. 1b, is reduced ~ 2.5 times compared with that in air. This reduction is possibly caused by a transition through the thermal velocity of sound a_t. A similar decrease in the coefficient C_x for a sphere in an argon plasma (approximately half that for argon) was identified for M numbers close to 0 in Ref. 9. Thus, for $M<0.7$ the drag force of a sphere in an air plasma is $X_p\approx 0.1X_c$.

The similarity between the curves $C_{xp}/P_{0p}'=f(M_p)$ and $\overline{C_{xc}}/P_{0p}'=f(\overline{M_c})$ for $M>0.8$ and also between $\Delta_p=\Delta_p(M_p)$ and $\overline{\Delta}=\overline{\Delta_c}(M_c)$, where $\overline{\Delta}$ is the relative separation of the shock wave head from the sphere, indicates that the stagnation pressure beyond the shock waves and the pressure distribution over an object in a plasma and in air are similar for $M_p=M_c>1$. This means that the aerodynamic characteristics and loads on objects passing through a plasma can be estimated for given M_p and γ_p using the usual methods.

A characteristic feature of the propagation of shock waves in a discharge plasma is that they are accelerated on

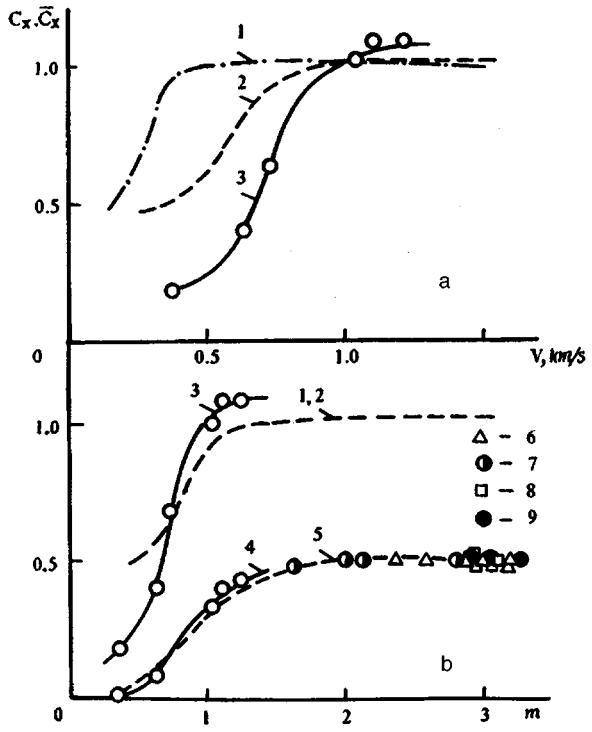

FIG. 1. Drag coefficient of a sphere as a function of velocity (a) and M number (b). C_x: *1* — cold air, *2* — heated air, *3* — plasma; $\overline{C_x}$: *4* — plasma, *5* — air, Re $=1.2\times10^3 M$, *6* — air, *7* — CO_2, *8* — Ar, and *9* — Freon-12 for Re $\sim10^6$ (Ref. 12).

entering the discharge zone. It was shown in Ref. 4 by means of calculations that the acceleration of shock waves in a plasma is only caused by thermal effects. This conclusion is supported by experimental data,[2,4–6,8,13,14] as is readily established by using the quantities measured in these studies to construct the ratio $\overline{V_p}/\sqrt{\overline{T_p}}$, where $\overline{V_p}=V_p/V_c$ and $\overline{T_p}=T_p/T_c$. In air and argon plasmas and in heated air this ratio is close to 1, which can only occur if the shock wave propagation velocities in the plasma and in heated air are the same and obey the same law:[15]

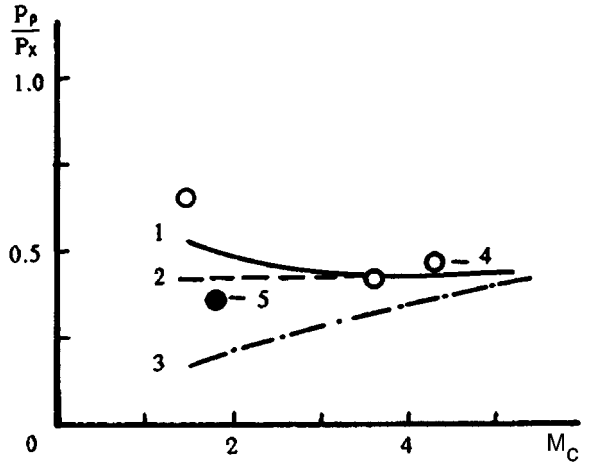

FIG. 2. Relative pressure behind shock wave as a function of M_c number. Calculations: *1* — P_0'/P_1, *2* — P_2/P_1, *3* — P_3/P_1; Experiment: *4* — Refs. 5 and 6, *5* — Ref. 6.

$$V=\frac{b}{r^n}\sqrt{\frac{E}{\rho_1}},$$

where E is the shock wave energy, ρ_1 is the density of the unperturbed medium, r is the coordinate, $n=1.5$, 1, and 0.5, and b = 0.4, 0.5, and 2/3, respectively, for spherical, cylindrical, and plane waves. Thus, in a plasma having the same composition as cold air we have:

$$V_p=V_h=V_c\sqrt{T_p/T_c};\quad M_p=0.675M_c=0.675M_h.$$

This means that formulas for a normal shock can be used to calculate the ratios of the pressures behind the shock wave P_{2p}/P_{2c}, the initial pressures P_{0p}'/P_{0c}', and the pressures behind the reflected wave P_{3p}/P_{3c} in a plasma (precursor) and in cold air. For the calculations the parameters of the incident shock wave were assumed to be the same and were taken as $\gamma_p=1.25$, $\gamma=1.4$. The results are plotted in Fig. 2, which shows that the pressure behind the shock wave (static and initial) in a plasma is 40–50% of that in cold air. This result is supported by the experimental data[5,6,8] (see Fig. 2).

In relaxing media the velocity of sound depends on the frequency ω, varying gradually as $\omega=1/\tau$, where τ is the relaxation time.[16] At low frequencies this velocity is the same as the usual adiabatic velocity of sound a_h, whereas at high frequencies, it is the same as the frozen or plasma velocity a_p. Since the shock wave propagation velocity in a medium is proportional to the velocity of sound, the shock wave on entering the discharge zone should split into two waves — a high-frequency or plasma wave with the propagation velocity $V_p\sim a_p$, and a low-frequency or residual wave with $V_0\sim a_0$, giving $V_p/V_0=a_p/a_0=1.48$. According to experimental data[5,6] $V_p/V_0=1.39$ for an incident wave velocity $V=500$ m/s and V_p/V_0 =1.43–1.6 for $V=1500$ m/s. These results for an incident shock wave ($V=1500$ m/s) entering a cold plasma ($T_p=350$ K) were used to calculate the ratios of the static and stagnation pressure behind the residual wave and the precursor, which were 1.5 and 2, respectively. However, the ratio of the pressures behind the residual wave and the precursor measured with an end piezoelectric transducer[6] was 2.5.

[1] G. I. Mishin, Yu. L. Serov, and I. P. Yavor, Pis'ma Zh. Tekh. Fiz. **17**(11), 65 (1991) [Sov. Tech. Phys. Lett. **17**, 413 (1991)].
[2] I. V. Basargin and G. I. Mishin, Pis'ma Zh. Tekh. Fiz. **15**(8), 55 (1989) [Sov. Tech. Phys. Lett. **15**, 311 (1989)].
[3] A. I. Klimov, G. I. Mishin, A. B. Fedotov *et al.*, Pis'ma Zh. Tekh. Fiz. **15**(20), 31 (1989) [Sov. Tech. Phys. Lett. **15**, 800 (1989)].
[4] P. A. Voĭnovich A. P. Ershov, S. E. Ponomareva *et al.*, Teplofiz. Vys. Temp. **29**, 582 (1991).
[5] A. Yu. Gridin and A. I. Klimov, Khim. Fiz. **12**, 363 (1993).
[6] A. Yu. Gridin, A. I. Klimov, and K. V. Khodataev, Teplofiz. Vys. Temp. **32**, 486 (1994).
[7] A. Yu. Gridin, A. I. Klimov, K. V. Khodataev *et al.*, Teplofiz. Vys. Temp. **32**, 809 (1994).
[8] I. V. Basargin and G. I. Mishin, in *Principal Results of Scientific Research 1989/1990* [in Russian], Physicotechnical Institute Press, Leningrad (1991), pp. 100–103.
[9] M. K. Asanaliev, V. S. Éngel'sht, E. P. Pakhomov *et al.*, in *Proceedings of the Fifteenth International Conference on Phenomena in Ionized Gases* [in Russian], Minsk (1981), pp. 959–960.
[10] A. P. Bedin and G. I. Mishin, Pis'ma Zh. Tekh. Fiz. **21**(1), 14 (1995) [Tech. Phys. Lett. **21**, 5 (1995)].
[11] A. B. Bailey and J. Hiatt, AIAA J. **10**, 1436 (1972).

[12] A. P. Bedin, V. P. Meleshko, G. I. Mishin *et al.*, in *Physicogasdynamic Ballistic Research* [in Russian], Nauka, Leningrad (1980), pp. 25–33.
[13] I. V. Basargin and G. I. Mishin, Preprint No. 880 [in Russian], Physicotechnical Institute, Academy of Sciences of the USSR, Leningrad (1984).
[14] I. V. Basargin and G. I. Mishin, Pis'ma Zh. Tekh. Fiz. **11**, 209 (1985) [Sov. Tech. Phys. Lett. **11**, 85 (1985)].
[15] L. I. Sedov, *Methods of Similarity and Dimensionality in Mechanics* [in Russian], Nauka, Moscow (1981).
[16] I. G. Mikhaĭlov, V. A. Solov'ev, and Yu. P. Syrnikov, *Principles of Molecular Acoustics* [in Russian], Nauka, Moscow (1964).

Translated by R. M. Durham